NANOWIRES FABRICATED BY FOCUSED ION BEAM

by

JAY PRAKASH NAIK

A thesis submitted to

The University of Birmingham

for the degree of

DOCTOR OF PHILOSOPHY

School of Mechanical Engineering

The University of Birmingham

August 2013

UNIVERSITY OF
BIRMINGHAM

University of Birmingham Research Archive

e-theses repository

This unpublished thesis/dissertation is copyright of the author and/or third parties. The intellectual property rights of the author or third parties in respect of this work are as defined by The Copyright Designs and Patents Act 1988 or as modified by any successor legislation.

Any use made of information contained in this thesis/dissertation must be in accordance with that legislation and must be properly acknowledged. Further distribution or reproduction in any format is prohibited without the permission of the copyright holder.

ABSTRACT

This thesis reports research on nanowires fabricated by FIB lithography with experiments to understand their mechanical, electrical and hydrodynamic properties.

Au nanowires fabricated on Si_3N_4 membranes with width below 50nm exhibit liquid like instabilities and below ~20nm the instabilities grow destroying the nanowires due to the Rayleigh–Plateau instability. Stability is better in the case for Si substrates than for the insulators SiO_2 and Si_3N_4.

A series of 4-terminal resistance measurements were carried out on a "platinum" nanowire grown by FIB-induced decomposition of an organometallic precursor. Such nanowires are found to be a two phase percolating system, containing up to 70% by volume carbon. They have unexpected temperature behaviour which is explained using a percolation model with Kirkpatrick conduction in the presence of temperature induced strain.

Au nanowire bridges of very small diameter were probed using AFM to investigate their deformation and fracture strength. Below a diameter ~50nm, the mechanical properties are consistent with liquid-like behaviour. After reaching the fracture, the gold molecules from the bridge retract towards the fixed ends; rebinding of the gold causing reforming of the nanowire bridge can occur.

FIB fabrication was also used to form a thermal bimorph MEMS cantilever which was investigated by AFM during actuation.

Dedicated to my parents and my sister............

ACKNOWLEDGEMENTS

My special gratitude goes to my incredible primary supervisor Prof. Philip D. Prewett, who has provided his inspirational guidance every step of the way throughout my PhD research project. This unconditional support has resulted in two good international journal publications and an international collaboration.

I would also like to thank Dr Mike C. Ward, as my second supervisor, for his advice during my PhD. The following people have generously given their time to provide me with training and guidance; Dr Carl Anthony and Dr Xueyong Wei for training on the Focused Ion Beam system and other cleanroom processes, Dr James Bowen for training on Atomic Force Microscope system, and Dr David Cheneler for training on the STS system.

My sincere thanks goes to Prof Arup K Raychaudhuri, Dr Kaustuv Das and Mr Manotosh Chakravorty from the Centre for Nanotechnology, S N Bose National Centre for Basic Sciences, Salt Lake (Sector-III), Kolkata 700098, India, for their contribution to our international collaboration under UKIERI and for personal guidance on my PhD. I would also like to thank the Department of Science and Technology, Government of India and the British Council of the UK Foreign Office for their financial support.

I would like to thank Prof Ejaz Huq and Dr Yifang Chen from STFC-Rutherford Appleton Laboratory, Chilton, Didcot OX11 0QX, United Kingdom, for training, guidance and support on the Plasma Etching process and Electron Beam Lithography.

Last but certainly not least I would like to thank my family and Miss Naomi Green, for their support not just during my PhD but all aspects of my life.

Table of Contents

Chapter 1: Introduction **1**

1.1 Introduction to the Research Project 1

1.2 Research Aims and Objectives 3

1.3 Outline of the Thesis 4

1.4 References 7

Chapter 2: Literature Review **8**

2.1 Introduction 8

2.2 Relevant Research on Nanowires 8

2.3 Structural and Electrical Properties 11

2.4 Mechanical Properties 12

2.5 Hydrodynamic Instability in Nanowires 13

2.5.1 Rayleigh Instability 14

2.5.2 Instability in Solid Materials 15

2.6 Focused Ion Beam System (FIB) 16

2.6.1 Background 16

2.6.2 System Parameters and Functions 17

2.6.3 Capability and Applications 18

2.6.3.1 FIB Imaging 18

2.6.3.2 FIB Milling 19

2.6.3.2.1 Without Enhanced Etching 20

2.6.3.2.2 With Enhanced Etching (EE) 21

2.6.3.3 FIB Metal Deposition (Ion Beam Induced Deposition) 22

2.7 Atomic Force Microscope System (AFM) 24

2.7.1 Principle of Operation and Hooke's Law 25

2.7.2 Imaging by AFM 27

2.7.3 Force Calibration and Deflection Measurement 29

2.8 References 31

Chapter 3: Fabrication and Characterisation Techniques 37

3.1 Introduction 37

3.2 Photoresist Spin Coating for FIB Fabrication 37

3.3 Design and Fabrication of Si Stencil Mask 39

3.3.1 Photolithography 41

3.3.2 Silicon Etching 41

3.3.2.1 Reactive Ion Etching (RIE) 42

3.3.2.2 Deep Reactive Ion Etching (DRIE) 43

3.4 Focused Ion Beam Lithography (FIB) 44

3.4.1 FIB on Photo Resist 45

3.4.2 FIB on Metallic Thin Film (Au) 47

3.5 Scanning Electron Microscopy (SEM) 49

3.6 Electron Beam Lithography (EBL) 51

3.7 Energy Dispersive X-Ray Spectroscopy (EDX) 54

3.8 References 56

Chapter 4: Study of Instability in Nanowires Fabricated by Focused Ion Beam Lithography 58

4.1 Introduction 58

4.2 Rayleigh – Plateau Instability, Surface Energy and Critical Radius (R_c) 59

4.3 Fabrication of Nanowires on Si_3N_4 Substrate 60

4.4 Hydrodynamic Instabilities 62

4.5 Analysis and characterisation of the Instabilities 64

4.6 Conclusion 67

4.7 References 69

Chapter 5: Effects of Substrate on the Instabilities in Nanowires Fabricated by Focused Ion Beam 69

5.1 Introduction 69

5.2 Liquid-like Instabilities 71

5.3 Fabrication Process of Nanowires on Different Substrates 74

5.4 Critical Radius and Hydrodynamic Instabilities on Different Substrates 76

5.5 Conclusion 82

5.6 References 83

Chapter 6: Study of Electrical Properties of Nanowires Fabricated by Focused Ion Beam Metal Deposition 86

6.1 Introduction 86

6.2 *Section* ***A*** 89

6.2.1 Percolating System 89

6.2.2 Sample Preparation for 4 – Probe Electrical Measurements 90

6.2.3 Microscopic Analysis of the 4 – Probe Nanowire Sample 92

6.2.4 Temperature Sensitive Resistivity Measurements of the 4 – Probe Nanowire 93

6.2.5 Analysis of the Results in 4 – Probe Electrical Measurements 94

6.3 *Section* ***B*** 99

6.3.1 Sample Preparation for Bimorph Cantilever 99

6.3.2 Force and Deflection Measurements on Bimorph Cantilever 102

6.3.3 Analysis of the Results from Measurements on Bimorph Cantilever by AFM 103
6.4 Conclusion 105
6.5 References 107

Chapter 7: Atomic Force Microscope Study of Mechanical Properties of Nanowire Fabricated by Focused Ion Beam Lithography 109

7.1 Introduction 109
7.2 Fabrication of the Nanowire Bridges 113
7.3 Atomic Force Microscopy on the Nanowire Bridges 114
7.4 Microscopic Analysis of the Nanowire Bridges 115
7.5 Conclusion 123
7.6 References 125

Chapter 8: Summary and Conclusion 127

8.1 Summary of the Thesis 127
8.2 Detailed Conclusion 128
8.3 Future Work 131
8.4 References 133

List of Figures

Figure 2.1	Image of helical strand of nanowire	10
Figure 2.2	Image of helical structure of nanowire strands	10
Figure 2.3	An example of liquid jet turning into droplets	14
Figure 2.4	Schematic diagram of the dual beam FIB/SEM system	16
Figure 2.5	Schematic diagram of the Ion Milling without Enhanced Etching	20
Figure 2.6	Schematic diagram of the Ion Milling with Enhanced Etching	21
Figure 2.7	Current density vs. Etch rate, variable dependency of gas to ion ratio	22
Figure 2.8	Current density vs. deposition rate in the FIB system	23
Figure 2.9	Schematic of modern system developed by Gerhard Meyer and Nabil M. Amer	25
Figure 2.10	SEM image of the AFM cantilever tip with a tip radius of 10 nm	26
Figure 2.11	Example of force vs z position of the AFM tip. This shows the typical manipulation path of the AFM probe	27
Figure 3.1	Schematic diagram of the spin coating process during the photolithography	38
Figure 3.2	Spin Speed Curves (Microposit S1800 Photo Resist Undyed Series)	39
Figure 3.3	Designs used for the emulsion film mask to fabricate contact pads as well as the Si stencil mask for the direct deposition of the contact pad on the chip	40
Figure 3.4	SEM image of the nano channels without Enhanced Etch	46
Figure 3.5	SEM image of the nano channels with Enhanced Etch	47
Figure 3.6	SEM image of gold nanowires with different sizes formed between nano channels	48
Figure 3.7	SEM image of the different sizes of free nanowires suspended in the Si_3N_4 substrate	49
Figure 3.8	An example of SEM image of an AFM cantilever tip used for the mechanical measurement	50
Figure 3.9	An example of incident beam interaction with a sample and several signals generated by the incident electrons in the Scanning Electron Microscope (SEM) and the regions from which the signals can be detected	51

Figure 3.10	Schematic of the Electron Beam Writer	52
Figure 3.11	SEM image of the gold (Au) nanowire fabricated by Electron Beam Lithography	53
Figure 3.12	Energy Dispersive X-Ray Spectroscopy (EDX) carried out on the gold (Au) nanowire on Si_3N_4 substrate	55
Figure 4.1	Cross-section of the Si_3N_4 membrane with FIB etched nanowire	60
Figure 4.2	SEM image of the 200 nm gold wire without size dependent variations in width	61
Figure 4.3	SEM image showing 60 nm wire with the appearance of the diameter variation	62
Figure 4.4	SEM image of a nanowire below 50 nm in diameter with periodic variation of the width	63
Figure 4.5	SEM image of the beginning of the formation of the droplet in the instable nanowire	64
Figure 4.6	SEM image showing a discontinuous nanowire.	65
Figure 5.1	Schematic showing the radial perturbation of a nanowire due to Rayleigh instability	72
Figure 5.2	EDX analysis results showing atom concentrations across the nanowire	76
Figure 5.3	SEM image of instability in thin gold nanowire (Sample A) on (a) nearly perfect nanowire with thickness of 100 nm (b) lightly doped Si with native oxide (c) instability seen on unpassivated lightly doped Si	77
Figure 5.4	(Sample B) (a) Au nanowire ~ 40 nm wide fabricated on unpassivated highly doped Si (b) thin straight nanowire with limited instability fabricated on passivated highly doped Si	78
Figure 5.5	SEM image of Au nanowires fabricated on SiO_2 (300 nm) /Si (sample C) showing more pronounced liquid-like instability (inset showing evidence of Taylor Cone formation with apex jetting).	79
Figure 5.6	(a) Nanowire on Si_3N_4 (200 nm)/Si (sample D) at the onset of fragmentation. (b) Nanowire fragmented into spheres	80
Figure 6.1	(a) Ion beam image of 4 – probe connection on nanowire of length 5 μm and width and thickness of 130 nm deposited by FIB at 29 pA on Si_3N_4 substrate. (b) SEM image of nanowire of length 5 μm and width and thickness of 50 nm deposited at 29 pA on SiO_2 substrate	90

Figure 6.2	(a) 4 – probe connection on FIB deposited nanowire of length 20μm (b) Demagnified view showing FIB deposited electrical connections to Au/Cr contact pads	91
Figure 6.3	Cross-section of FIB deposited C-Pt on SiO_2/Si wafer substrate. Pt islands are distributed in a high resistivity carbon matrix	92
Figure 6.4	Resistivity vs Temperature of four nanowires (S1 - S4)	94
Figure 6.5	Resistivity (ρ) vs Metallic Concentration (C) for different temperatures	95
Figure 6.6	Deflection of the bi-layer substrate of Si and SiO_2	97
Figure 6.7	Surface strain (ε_s) due to bending of the substrate. Inset shows the thermal expansion coefficient (α) of Si and SiO_2	98
Figure 6.8	a) SEM image of cantilever (6 μm x 1.5 μm); b) single Pt heating meander of width of approximately 100 nm	100
Figure 6.9	SEM image triple meander Pt-C heater	100
Figure 6.10	Schematic of the AFM Probe used to measure the force generated by the MEMS bimorph cantilever when a current is supplied through the Pt heater fabricated by FIB metal deposition on the surface of the Si_3N_4 membrane	101
Figure 6.11	Consolidated approach signal from AFM tip (used to measure Force/Deflection signal).	103
Figure 6.12	(a) Current ($\boldsymbol{I}$) vs Deflection ($\boldsymbol{\delta}$), (b) Force ($\boldsymbol{F_{eff}}$) vs Current ($\boldsymbol{I}$)	104
Figure 7.1	FIB fabricated gold nanowires on silicon bridges before the silicon removal by RIE	113
Figure 7.2	a) FIB fabricated nanowires after removing the silicon material under the gold nanowires to form a nanobridge by RIE process in STS plasma etcher (before the AFM loading). b) Nanobridge reaching its fracture point after AFM loading.	114
Figure 7.3	3D images of, a) Nanowire bridge just before axial loading showing the elevated position in the midpoint and b) Two halves of the "nanowire bridge" just after reaching the fracture point.	115
Figure 7.4	AFM tip manipulation path during the loading and unloading, a) A nanowire with diameter of 60 nm reaching fracture point at 508 nN (no rearrangement or retraction observed), b) A nanowire with diameter < 20	116

nm shows the constant rearrangement of gold molecules resulting in multiple fracture points (represented by 1, 2, 3)

Figure 7.5 SEM image of "*nanowire bridge*", after reaching the fracture point, a) in nanowire bridge with 60 nm diameter (no retraction observed), b) in nanowire bridge with 40 nm diameter elongated to 20 nm (a small amount of retraction is observed), c) in nanowire bridge with 16 nm diameter and close to the critical diameter of the material (retraction of the gold molecules towards the surface of the substrate is observed), d) in nanowire bridge with 16 nm diameter (it is observed that the gold molecules rebind the two newly formed beams as result of *van der Waals* forces and liquid behaviour) 117

Figure 7.6 SEM image of nanowires of 40 nm (top), 30 nm (middle) and 16 nm (bottom) reaching their fracture points and achieving increasing amounts of retraction depending on their decreasing diameter 119

Figure 7.7 Schematic diagram of scenario one, where the bridge retracts, showing the AFM tip movement and the step-by-step behaviour of the nanowire bridge under tension; a) the AFM tip approaches the midpoint of the nanowire bridge, b) just before the tip touches the nanowire bridge the gold atoms pull the cantilever downwards due to *van der Waals* force, c) the AFM tip dislocates the gold molecules in the nanowire bridge due to forced elongation, d) just before the fracture point the nanowire bridge thins down to a single atom Au-Au bond under loading tension, e) just after reaching the fracture point the Au-Au bond breaks and because of the spring effect the gold atoms retract until the structure achieves the minimum energy configuration 121

Figure 7.8 Schematic diagram of scenario two, where the bridge heals, showing the AFM tip movement and the step-by-step behaviour of the nanowire bridge under tension however the loading was retracted immediately after fracture point; a), b), c) and d) are repeated steps from scenario one, e) just after reaching the fracture point the Au-Au bond breaks, however, unlike scenario one the ends of the two newly formed beams have created 122

a bond with the AFM cantilever tip surface under the influence of *van der Waals* force. f) the AFM tip was retracted after the fracture point and the ends of the newly formed beam re-establish the Au-Au bond which can be described as a self healing process

List of Tables

Table 2.1	Sputter yield and milling rate of different materials	19
Table 3.1	The parameters of RIE for 100 nm undercut of nanowires (Etch rate ~ 750 Å/min)	43
Table 3.2(a)	The parameters for the standard DRIE etch using the STS Multiplex ICP DRIE etcher (STS Plc., UK). DRIE of masks with Etch rate ~ 2.5 μm/min – estimated)	44
Table 3.2(b)	The parameters for the standard oxygen plasma clean using the STS Multiplex ICP DRIE etcher (STS Plc., UK).	44
Table 5.1	Properties of the nanowire instability for different substrates	81
Table 6.1	Volume concentration of conducting and non conducting elements with FIB energy at 28 pA beam current (+/- 0.1%)	93

List of Publications

J P Naik, K Das, P D Prewett, A K Raychaudhuri, and Yifang Chen, *Liquid-like instabilities in gold nanowires fabricated by focused ion beam lithography*, Appl. Phys. Lett., 2012, **101**: p 163108.

J P Naik, P D Prewett, K Das, and A K Raychaudhuri, *Instabilities in Focused Ion Beam-patterned Au nanowires*, Microelectronics Engineering, 2011, **88**: p 2840.

Manotosh Chakravorty, Kaustuv Das, A K Raychaudhuri, J P Naik, P D Prewett, *Temperature dependent resistivity of platinum-carbon composite nanowires grown by focused ion beam on SiO2/Si substrate*, Microelectronic Engineering, 2011, **88**: p 3360–3364.

J P Naik, P D Prewett, K Das, and A K Raychaudhuri, *Investigation of the force generated in a thermally activated bimorph cantilever heater using an Atomic Force Microscope* (In preparation)

J P Naik, J Bowen, D Chaneler, P D Prewett, A K Raychaudhuri, *Atomic Force Microscopic study of atomic rearrangement in the nanowire bridge fabricated by Focused Ion Beam lithography* (In preparation)

Chapter 1

Introduction

1.1 Introduction to the Research Project

Research into the fabrication and application of nanowires is rapidly increasing due to their potential in many fields, such as electronics, optics, sensors, and medicine. Nanowires can be defined as a structure of less than 100 nm in diameter. However their length can be few hundred times longer, resulting in an extreme aspect ratio (length to width ratio) of more than 100. For this reason nanowires are often referred to as quasi-one-dimensional structures. This one-dimensionality makes the properties and behaviour of these nanowires interestingly distinct from the bulk material. The exploration of these differences is still in the experimental phase. Understanding the electrical, mechanical & hydrodynamic properties of nanowires better through experimental measurements will enable the expansion of their use.

These properties will vary between different materials, for example metals behave differently from their semiconductors counterparts. The experiments conducted in this thesis focus on the use of gold (Au), platinum (Pt), nickel (Ni), chromium (Cr), silicon (Si) and silicon nitride (Si_3N_4), due to their distinct properties at the nano scale, e.g. conductivity, elasticity, hydrodynamic stability.

The method of fabrication also has particular importance as this can affect the properties and behaviour of the nanowire. Nanowires can be fabricated by using various techniques such as photolithography, bombardment of ions (Focused Ion Beam or FIB), electron beam lithography (EBL), chemical etching, electrodeposition and Vapour-Liquid-Solid (VLS) synthesis method. The use of Focused Ion Beam (FIB) is one of the simplest and most

efficient ways of fabricating nanowires. The technique allows nanowires to be fabricated from almost any material which can be deposited on the substrate, using one of the deposition techniques (sputtering, evaporation or electrochemical deposition).

Due to the high aspect ratio in a nanowire the surface to volume ratio is very large and surface tension effects dominate. In metallic nanowires this causes them to behave more like liquids than solids. Below ~ 50 nm and above a critical diameter, hydrodynamic instabilities occur in the nanowire and ultimately become unstable below the critical diameter [1]. Understanding these instabilities is crucial for the fabrication of Nano Electro Mechanical Systems (NEMS) devices and their applications, such as interconnects, because of the absolute requirement that they have a stable and controlled geometry. The substrate on which the nanowires are fabricated has a significant effect on the stability of the nanowire.

For Micro Electro Mechanical Systems (MEMS) to function effectively it is important to have a precise knowledge of the piezoresistive effects in nanowires. It has been reported that FIB deposited platinum nanowires are carbon-metal composites [2], which can be described as a two phase 3D percolating system. If this is the case then the nanowires will have a negative temperature coefficient of resistivity [3]. A study of the temperature dependent resistivity was carried out to understand the transportation of electrons within the Pt nanowire. A series of 4-terminal resistance measurements were made at a range of different temperatures and volumes concentrations of platinum [3].

A significant number of MEMS are dependent on the use of thermally actuated bimorph cantilevers to generate deflection and force, such as micromechanical switches and chemical sensors. Bimorph cantilevers are of significant interest in the application of nanoscale strain gauges. An Atomic Force Microscope (AFM) was used to accurately measure the deflection and the effective force generation as a function of drive current in a thermally actuated

bimorph cantilever system, on silicon nitride (Si_3N_4) membrane, fabricated by a combination of FIB milling and metal deposition system.

1.2 Research Aims and Objectives

The aims of the research are to study the mechanical, electrical and hydrodynamic behaviour of nanowires fabricated by FIB. Understanding these properties is significantly important for the development and application of NEMS and MEMS devices.

To achieve these aims, the following objectives are highlighted below,

- Conduct a literature review of the current research and development on nanowires fabrication, characterisation, and hydrodynamic, mechanical and electrical behaviour.
- Use a range of fabrication and characterisation techniques to fabricate nanowires with a diameter of a few nanometres.
- Study the hydrodynamic instability of gold nanowires fabricated by Focused Ion Beam Lithography.
- Investigate the effect of substrates on the hydrodynamic instability on gold nanowires fabricated by FIB.
- Conduct a four probe electrical measurement to analyse percolation theory in FIB deposited platinum nanowires.
- Fabricate a thermally actuated bimorph cantilever and define the relationship between force and current, to understand its potential application as a strain gauge.

- Determine the fracture point of FIB fabricated gold nanowire bridges, using AFM, in order to understand the atomic mobility in free standing nanowires below the critical radius of instability.

- Perform an AFM loading to achieve the fracture point of FIB fabricated nanowire bridge.

1.3 Outline of the Thesis

The research undertaken to meet the aims and objectives above is presented in this thesis. It contains eight chapters, which are described below.

Chapter 1 is an introduction to nanowires fabricated by Focused Ion Beam lithography and the understanding of their hydrodynamic, electrical and mechanical behaviour. The project aims and objectives are outlined in this chapter as well as the structure of the thesis.

Chapter 2 is a literature review of current research allied to this thesis, which outlines the work already carried out by different researchers around the world. This chapter also describes in detail the theoretical background to the research. The capability and application of the primary fabrication system, Focused Ion Beam, and characterisation techniques, such as Atomic Force Microscopy are described in detail. It also reviews the different types of nanowires fabricated from different materials used for the various applications in NEMS devices.

Chapter 3 describes the various fabrication techniques used to fabricate nanowires i.e. Nano Electrodeposition, Electron Beam Lithography, Photolithography and Focused Ion Beam Lithography. Also described are various characterisation techniques i.e. Scanning Electron Microscopy, Energy Dispersive X-Ray Spectroscopy. All the fabrication methods mentioned in this chapter have the ability to fabricate nanowires in the range of 10 – 500 nm. However

the different fabrication methods result in nanowires with different electrical, mechanical and hydrodynamic properties.

Chapter 4 investigates experimentally the fact that FIB fabricated Au nanowires have a structural instability below a certain diameter. The observed behaviour has been explained as a manifestation of the Rayleigh – Plateau instability [4, 5], which occurs below a critical diameter, where the surface energy becomes the dominating feature. It is vital that these instabilities are understood for the fabrication of NEMS devices, such as strain gauges, due to the need for them to have a stable and well defined geometry.

Chapter 5 investigates experimentally the instability of different types of Au nanowire, at different widths on different substrates. The results demonstrate the clear tendency for liquid-like behaviour, associated with electrohydrodynamic instabilities for narrower nanowires, on all substrates. However, the stability of the wires is noticeably better in the case of conducting silicon (Si) substrates than for silicon coated with the insulators SiO2 or Si3N4, due to the minimisation of space charge effects during FIB fabrication. This instability could severely limit the use of FIB patterned gold nanowires in nanosensors and other nanoscale devices.

Chapter 6 describes the fabrication process of platinum (Pt) nanowires fabricated by FIB metal deposition. It investigates the electrical properties of the nanowire and experimentally and theoretically explains the composite percolation system using 4-probe connections on FIB deposited nanowire of length 20 μm. This chapter also describes the use of AFM to measure deflection and effective force generation as a function of drive current in a thermally actuated bimorph cantilever system, on silicon nitride (Si_3N_4) membrane, fabricated by a combination of FIB milling and metal deposition system.

Chapter 7 describes the use of AFM to measure the mechanical properties of nanowire bridges, fabricated by the combined process of FIB lithography and Reactive Ion Etching (RIE). We have experimentally shown that, after reaching the fracture point under loading tension, the gold molecules in the nanowire bridge retract towards the fixed ends due to liquid-like behaviour and continuous rearrangement of gold atoms. The observations recorded also confirm that this phenomenon occurs only below the critical diameter of the nanowire bridge.

Chapter 8 consolidates the main findings of this research into the mechanical, electrical and hydrodynamic behaviour of nanowires fabricated by FIB. It also suggests possible future research areas to expand on this work.

1.4 References

[1] Naik J. P., Prewett P. D., Das K., Raychaudhuri A. K., *Instabilities in Focused Ion Beam-Patterned Au Nanowires*. Microelectronics Engineering. 2011, **88**: p 2840-2843.

[2] Scott Kirkpatrick, *Percolation and Conduction.* Rev. Modern Phys. 1973, **45**: p 574.

[3] Manotosh Chakravorty, Kaustuv Das, A. K. Raychaudhuri, J P Naik and P D Prewett, *Temperature dependent resistivity of platinum–carbon composite nanowiresgrown by focused ion beam on SiO_2/Si substrate*. Microelectronic Engineering. 2011, **88:** p 3360–3364.

[4] Lord Rayleigh, Proc. London Math. Soc. 1878, **10**: p 4.

[5] J Plateau Transl. *Annual Reports of the Smithsonian Institution*. 1873, p 1863.

Chapter 2

Literature Review

2.1 Introduction

Nanowires seize the attention of researchers around the globe because they have different properties from the bulk material. Nanowires are usually defined as a structure with width in the range of 10 – 100 nm. Miniaturisation of such a small structure with high aspect ratio makes scientists try to explore various new methods of fabrication and investigation, which are economical, efficient and good quality. Applications including high density magnetic storage in memory devices, fuel efficiency in automobiles, hydrogen sensors, thermal devices and high performance electrical storage facilities etc., make this research extremely significant. This chapter outlines a review of the body of knowledge carried out by researchers around the world to date. The primary system, Focused Ion Beam, (FIB) used for this work is described in detail including its background, applications and functions. Atomic Force Microscope (AFM) is described in detail in the second half of the chapter, ahead of its use to carry out mechanical measurements in Chapter 7.

2.2 Relevant Research on Nanowires

Various techniques to fabricate desired reduced dimensionality and good quality nanowires are well documented. Yeh and Yang [1] have developed a method of fabricating two dimensional (2D) uniform arrays of Nickel nanowires with large aspect ratio using the simple electrodeposition method. Nano Channel Glass (NCG) was used as a template to grow nanowires inside the channel using both electrodeposition and supercritical fluid processes.

The fabrication method of NCG template is similar to that for optical fibres [1, 2]. Shi, Wu and Szpunar [3] have developed palladium nanowires using the simple and very economical electroless deposition process. They use the phenomena of palladium nanoparticles linking together in one direction bead by bead on the stainless steel substrate. The dimensions of the nanowires can be controlled by the $PdCl_2$ in the plating bath. Kamalakar and Raychaudhuri [4] have also developed a technique to fabricate tubular nanostructures (nanowires) using three electrode rotating field electrodeposition. To fabricate metal nanotubes (MNT), Kamalakar used an anodic alumina template and managed to achieve 20 nm internal diameter and 160 nm outer diameter nanotubes. Dimitri *et al* [5] developed a method of fabricating nanowires using Nanolithography for use in a Single Electron Tunnelling system. They used a porous anodic aluminium oxide template to fabricate semiconductor nanowires. Dimitri achieved a range of nanowires with diameters from 5 nm to few hundred nanometres. High demand for nanostructures, considering their potential applications, leads researchers to carry out experiments to explore their electrical and mechanical behaviour. Some of the experiments carried out by various scientists to fabricate nanowires are reviewed and described in this chapter.

During the fabrication of the nanowires using the FIB, an unusual shape of nanowire was observed. The nanowire edges, which were bombarded with the ions, were not sharp but a smooth round shape often with a wavy nature. This unusual observation has been explained by the theory of Y. Kondo and K. Takayanagi [6], and E. Tosatti and S. Prestipino [7]. According to their theory, gold nanowires at a few nanometre scale experience rearrangement of the atoms at their edge. These atoms create triangular bonds with their nearest neighbouring atom and form into complete strands of gold atoms. Figure 2.1 explains the shape of these nanowires. From the figure the colour red describes the central strand and the colour pink and white are subsequent strands around the central strand, respectively. The

conductivity of each strand is $2e^2 / h$ (Where e is the electron charge and h is the Planck's constant) [6, 8]. The conductivity of the nanowire depends on the number of strands carried by the nanowire. So the generalised formula of conductivity of each nanowire can be given by n*($2e^2 / h$) (where n is the number of strands in each nanowire). Similarly, if the

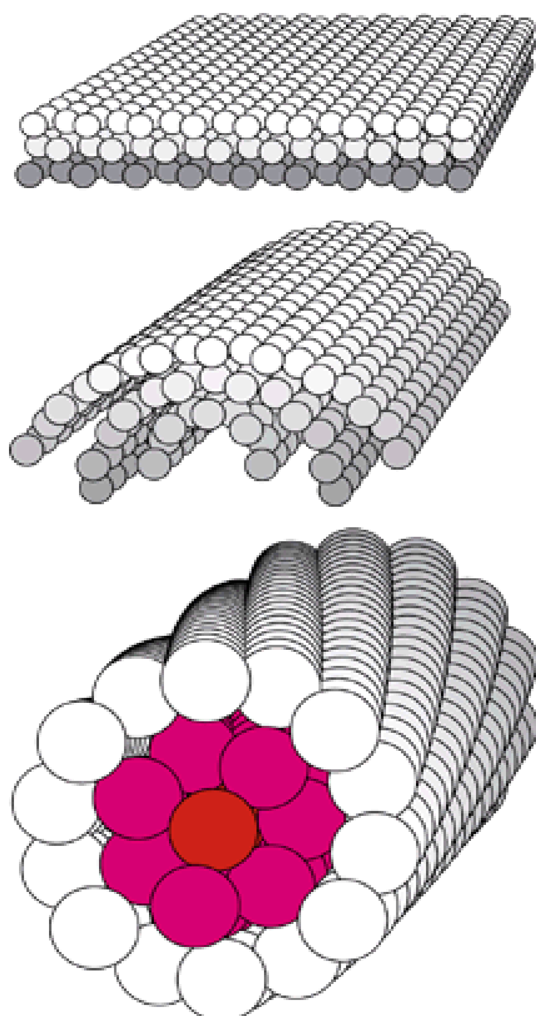

Figure 2.1: Image of helical strand of nanowire [6,7]

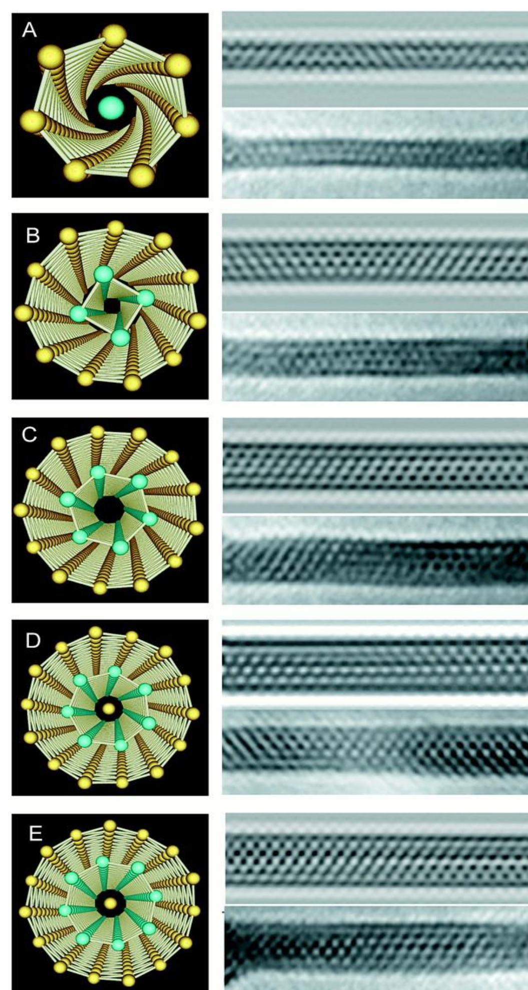

Figure 2.2: Image of helical structure of nanowire strands [6]

conductivity of the nanowire is known, the number of strands in each nanowire can be calculated and therefore its electrical properties can be described. Figure 2.2 explains the structure of the nanowires and explains the helicity of the strands.

2.3 Structural and Electrical Properties

Kondo *et al* [8] observed gold nanowires in the Transmission Electron Microscope (TEM) and measured their conductance, eventually reaching the conclusion that a gold nanowire contains a series of strands of gold atoms. He measured the electron transport within the nanowires and determined that the transport of electrons is ballistic rather than diffusive as in the bulk material. Kondo described that the strands of gold atoms inside the nanowires have the unconventional property of self rearrangement and except for the middle strand; all the other strands of atoms are surrounded in a helical shape [6, 8]. It contains a multi-shell structure composed of coaxial tubes. The helical strand around the axis of the central strand makes a structure similar to carbon nanotubes. They also concluded that the structures of strands are described by L-M-N (L is the central strand, M, N is the subsequent outer strands) [2]. Each subsequent strand of atoms from the central strand has an additional 7 strands (i.e. 1-7-14) [6]. Each atom forms triangular bonds with its neighbouring atoms to build tubular structures [6, 8]. Yi Cui *et al* [9] at Stanford University made an extraordinary discovery of *"High-performance lithium battery anodes using silicon nanowires,"* This battery can hold 10 times more charge than the conventional lithium-ion battery. They concluded that by using the silicon nanowires instead of conventional carbon electrodes increases the discharge time of the battery. They describe how silicon nanowires have different characteristics to those of the bulk material. Bulk silicon can expand after absorbing the positively charged lithium during the process of charging and contract during the discharging process making the silicon break in to pieces. Yi Cui used silicon nanowires, which have unique properties and do not break during the charging process [9].

2.4 Mechanical Properties

Professor John Sader *et al* [10] at University of Melbourne developed germanium nanowires, which have a size range of 20 – 80 nm. The fracture strength of these nanowires was observed to be 15 GPa, which is close to the theoretical value of ~ 17 GPa [10]. They developed a generalised model for nanowire strength and by using AFM lateral manipulation they concluded that nanowires grown by the super critical fluid process have close to the theoretical ultimate strength. This mechanical property of the nanowire is the highest ever reported for any semiconductor material. Emra Celik [11] from University of Arizona measured the mechanical properties of nickel nanowires with a diameter range of 250 nm. A template synthesis technique, which requires electroplating of the nickel into nanopores was used. Measurements of the properties were carried out with an in-situ AFM & Scanning Electron Microscope (SEM) combination. It was discovered that the elastic strength of the nanowires is significantly higher than the bulk material. However the nanowire diameter in this particular case is significantly higher when compared to our work [11, 12]. Their work also contains some theoretical explanation of higher strength in nanowire compared to its bulk material. Another AFM experiment carried out by Bin Wu *et al* [12] at Trinity College Dublin is one of the most significant and highly contributing works so far in mechanical property measurement of nanowires. Wu used an alumina template and electrodeposition method to fabricate nanowires with diameter range of 40 – 200 nm. The nanowires were placed on a silicon substrate with trenches underneath and AFM lateral loading was used in order to obtain the Young's modulus, yield strength and behaviour during plastic deformation and failure. Wu compared the material behaviour of the nanowires to a bulk nanocrystalline material (BNM) with a similar grain size. The results are in line with Celik's work [11], although the materials used are different. (Wu used Au nanowires but Celik used Ni, which is a ferromagnetic material). Neither considered the fact that nanowires with a diameter range

from 20 – 80 nm contain hydrodynamic instabilities [13]. The results show that the Young's modulus is independent from the nanowire's diameter and similar to the bulk material. However the yield strength was observed to be 100 times that of the bulk material, and is dependent on the diameter, with the largest yield strength being reported in the smallest wire of 40 nm. The ultimate strength of the Au nanowire is reported to approach the theoretical value of the order of one tenth the value of Young's modulus for the bulk material [12]. Au nanowires have a clear yield point and exhibit strain hardening, unlike BNM's with a similar grain size which display near perfect elasto-plasticity. Wu and Celik [11-12] both hypothesise that this is due to the reduction in the number of defects in the material and also the limited number of grains across the diameter of the nanowire.

2.5 Hydrodynamic Instabilities in Nanowires

In order to use the metallic nanowires in nano-device applications such as interconnects and nano-sensors, they have to demonstrate long term mechanical and electrical stability. However instabilities of metallic nanowires have been observed at higher temperatures for post growth annealing [14] and even at room temperature for thinner wires [15]. Such morphological instabilities can be attributed to the so-called Rayleigh instability and are of concern to researchers wishing to fabricate such nanowires and apply them as interconnects, for example. Some theoretical work has been done on cylindrical systems considering the effect of surface tension leading to a perturbation in diameter. An extensive theoretical study has been done by Lord Rayleigh on the stability of a nonviscous liquid [16] and an extension to this approach to solids by Nichols and Mullins [17]. Karim *et al* [18] have investigated the thermal instability of gold nanowires produced by electrochemical deposition in polymer membranes. It has even been recently suggested that sub 10 nm structures suffer serious line

roughness problems which render devices with these dimensions "intrinsically unmanufacturable" [19].

2.5.1 Rayleigh Instability

The instability which takes place in a thin jet of liquid is called Rayleigh Instability. Lord Rayleigh in 1878 [16] studied the scaled down jet of fluid to understand the instability within

Figure 2.3: An example of liquid jet turning into droplets (Ref: Prof Arup K Raychaudhuri private communication)

a range of diameters. Figure 2.3 is a typical example of Rayleigh Instability which takes place in a liquid column. The phenomenon also exists in the solid material, which was later proved experimentally by Rodel and Glaeser in 1990 [20].

2.5.2 Instability in Solid Materials

The main theoretical concept of this work is that at high temperature and in vacuum the metal atoms would be expected to adopt a new minimum energy configuration when gravity is negligible and surface tension forces are greater than the combined effect of gravitational force and yield force. Below a critical radius the surface forces, F_s, become greater than the yield force, F_y, and the metal will deform to a new surface shape. Equation 2.1 explains the condition for a material to maintain stability [16],

$$F_s = -\pi R \sigma_s \, , F_y = -\pi R^2 \sigma_y \, , F_y \geq F_s => R \geq \frac{\sigma_s}{\sigma_y} \qquad (2.1)$$

where R is the critical radius of the structure, σ_y is the yield stress and σ_s is the surface stress. For metals like Au, the critical radius ranges between 4 nm and 10 nm (determined in Chapter 5) and the free energy may be calculated using the theory of Plateau (1873) [21]. The so-called Rayleigh-Plateau instability sets in when the force due to surface tension exceeds the limit that can lead to plastic flow. This occurs at a diameter $< d_m = 2\sigma_s / \sigma_y$, where σ_s is the surface stress and σ_y is the yield stress [22, 23]. When fluctuations in the radius (r) of the wire have a wavelength (λ) less than the circumference (i.e. $\lambda < 2\pi r$) then perturbation increases the free energy [25]. It can then be shown that, when fluctuations in the radius (r) of the wire have a wavelength (λ) greater than its circumference (i.e. $\lambda > 2\pi r$), the perturbation decreases the free energy and perturbation amplifies with time [13, 23]. Thus the wire becomes unstable and tends to breakup into smaller segments and ultimately into small droplets to minimise the

free energy. The nanowires in this case get deformed from the pure cylindrical shape to a wire with width varying in an approximately periodic manner along its axis.

2.6 Focused Ion Beam System (FIB)

Focused Ion Beam is a fabrication tool used for industrial and research applications for decades. However, in recent years the use of FIB in nanofabrication processes has dramatically increased due to technology developed by manufacturers like FEI with ion beam spot diameter down to a few nanometres. The precision and sensitivity required in devices like sensors, actuators and interconnects inspires researchers to push their limits on systems like FIB for fabrication. FIB is the primary tool for the present work on metallic nanowires.

2.6.1 Background

FIB uses Liquid Metal Ion Source (LMIS) as a primary component of the system. A typical FIB system contains an ion column, a sample stage, multiple detectors, two electrostatic lenses, multiple apertures, gas delivery system, computer feedback system and a vacuum chamber. There are two different types of source needle used in the LMIS system: directly heated and indirectly heated (separately heated by filament heater) [24]. A schematic of the FIB system is shown in the Figure 2.4 [25]. LMIS science and technology has links back to

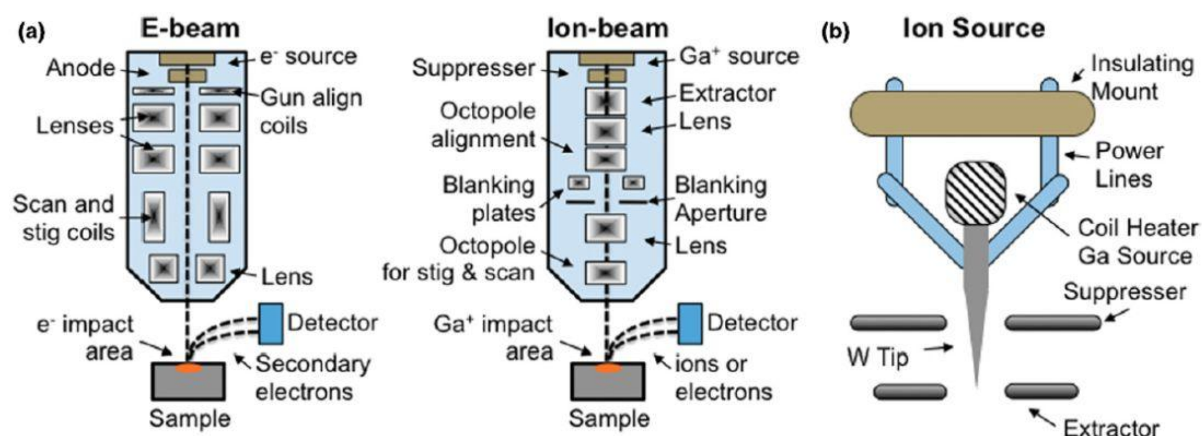

Figure 2.4: Schematic diagram of the dual beam FIB/SEM system [25]

the 18th century when Bose first reported to have observed the formation of water threads at the nozzle of an electrified capillary [24]. However, the fully functional LMIS used in FIB was developed in the 1970's. The most commonly used LMIS is the Ga^+ blunt needle source due to its advantages over its alternatives like Au, In, Bi, Sn etc. Gallium (Ga) has low melting temperature, low volatility and low vapour pressure [26], which provides a clear advantage. Gallium based LMIS are more stable than their rivals due to their nonreactive properties with source needle materials like tungsten (W) [24-26].

2.6.2 System Parameters and Functions

In the FIB system the Ga^+ blunt needle source generates an ion beam in two focusing steps using a condenser-objective lens combination [27]. The emitted beam from the source typically uses two lenses in order to focus the ions from the LMIS. Unlike electron beam systems, FIB tools use electrostatic lenses instead of electromagnetic lenses [24]. The location of these two lenses and the different stages where the beam passes through are shown in Figure 2.4. The top octopole aligns and directs the beam to pass through the blanking aperture via beam blanker plates to avoid constant milling. The beam then reaches a second octopole via a second lens, which provides the function of astigmatism correction, scan and shift [24-28]. Sputter yield is typically defined as the number of atoms removed by the incident Ga^+ ions, which is dependent on the material properties of emitted ions and the sputtered material, i.e. beam energy, atomic mass, angle of incidence, crystal orientation and surface energy of the target material [28-30]. The minimum spot size in the current system (FEI Strata™ Dual Beam 235 FIB-SEM) at the University of Birmingham is below 10 nm. Secondary electrons generated during the milling process are used to identify the point where one material ends and the layer of another material starts. The process is called End Point Detection (EPD). EPD is very useful in order to determine the milling rate and sputter yield

of different materials. Fabrication of gold nanowires on a silicon (Si) or silicon nitride (Si_3N_4) membrane is the perfect example of the application of EPD due to their sharp contrast in conductivity compared to gold.

2.6.3 Capability and Applications

An FIB system can be used for removing material from the substrate (Ion Milling), imaging and metal deposition (Ion Beam Induced Deposition) on the substrate. FIB can be used for repairing defective photolithography or X-Ray lithography masks. FIB metal deposition is most commonly used in interconnects and redesigning the circuit parameters in NEMS devices to modify their functions [31-33].

2.6.3.1 FIB Imaging

A Focused Ion Beam system can also be used as an imaging tool. FIB imaging is very similar to Scanning Electron Microscope imaging; however, positively charged ions are used instead of negatively charged electrons. The secondary electrons generated by the interaction between positively charged (Ga^+) ions and the targeted material contains the information to generate an image, a process which is called Scanning Ion Microscopy, SIM. SIM images are typically used for the positioning of processing points, monitoring of processing conditions, and observing cross sections [27]. SIM imaging is different to SEM imaging due to an absence of backscattering, enhanced surface resolution, greater sample damage (i.e. sputtering due to high energy ions) and Ga^+ ions implantation [26, 30]. Insulating samples can be imaged significantly better in SIM mode compared to SEM due to lower charging effects. In the current research, both the FIB systems used (FEI Strata^{TM} Dual Beam 235 FIB/SEM and FEI Dual Beam Helios 600 FIB-SEM) are dual beam systems with a separation angle of 52° between ion beam and electron beam.

2.6.3.2 FIB Milling

FIB milling is a process to remove (sputter) the target material using a beam of positively charged (Ga^+) ions emitted from LMIS. This process is also known as Maskless Etching. Ion milling can be typically classified into two categories: without Enhanced Etching (simple milling) and with Enhanced Etching (chemically assisted). The milling rate ($\mu m^3/s$) is linearly proportional to the beam current [30]. The efficiency of sputter yield, *Y*, is a significant factor to consider while milling nanoscale two dimensional (2D) or three dimensional (3D) structures (i.e. nanowires), which can be expressed by Equation 2.2 [29, 34]:

$$Y_{\mu m^3/nC} = \frac{Y_{atoms/ion} \times M}{96\rho} \quad (2.2)$$

where *M* is molecular weight and ρ is the density of the target material in g/cm^3. The applied dose (nC) can be obtained from the ion beam current and the milling time [29]. Sputter yield of different materials (Atoms/ion) at 0° angle is listed in Table 2.1 [29-37].

Table 2.1: Sputter yield and milling rate of different materials [29-37].

Material	**Sputter Yield (Atoms/Ion)**	**Milling Rate ($\mu m^3/nC$)**
Gold (Au)	18	2.55
Chromium (Cr)	3.5	0.28
Silicon (Si)/SiO_2	2.1 (Si)	0.25 (Si)/0.297 (SiO_2)
Silicon Nitride (Si_3N_4)	0.5	0.21

2.6.3.2.1 Without Enhanced Etching

Simple Ion Milling is an etching process without any type of physical or chemical assistance which also occurs in an unwanted manner during FIB imaging. The milling rate is dependent on the angle of the incident beam and the mass of the targeted material atoms as well as the ion energy. This dependency can be explained by $Y_{(\varphi)}/Y_{(0)}=1/\cos^{\beta}(\varphi)$, where φ is measured from the surface normal. Figure 2.5 [30] explains the removal of the targeted material atoms by the high energy ions. Table 2.1 shows the milling rates of different materials [37]. A significant disadvantage of using this method is the redeposition of the sputtered material on to the trench sidewalls. This problem can be overcome with the use of Enhanced Etching (EE) and controlling the milling strategy, including pixel dwell time [38-39].

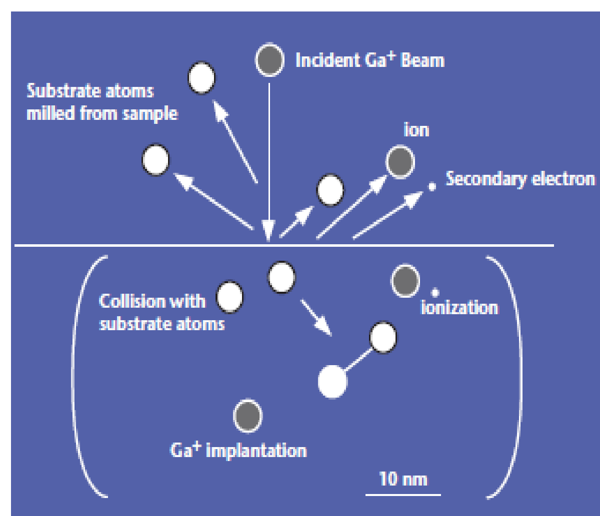

Figure 2.5: Schematic diagram of the Ion Milling without Enhanced Etching [30]

2.6.3.2.2 With Enhanced Etching (EE)

Focused Ion milling with Enhanced Etching (EE) uses chemical assistance to the incident beam of positively charged (Ga^+) ions. This process eliminates many of the disadvantages of simple ion milling and significantly reduces the process of unwanted redeposition of the sputtered sample material while increasing the milling rate [24, 27-30]. Enhanced Etching uses controlled gas delivery combined with the ion beam [28], as shown in Figure 2.6. The FIB system used in the present work at the University of Birmingham (FEI Strata^{TM} Dual Beam 235 FIB/SEM) uses iodine (I_2) as the EE gas. The simple ion milling rate is directly proportional to the ratio of current density to the number of ions bombarded on the surface [27-28], while the milling rate with EE is dependent on the targeted material, current density and the type of etch enhancing gas used. Typical etch gases include iodine (I_2) or water vapour (H_2O). Care must be taken when using any etch gas to avoid the formation of unwanted chemical compounds. The selection process requires consideration of the etch gas and surface properties like sticking coefficient, and the gases should preferably only react with the target material at the time of bombardment [27].

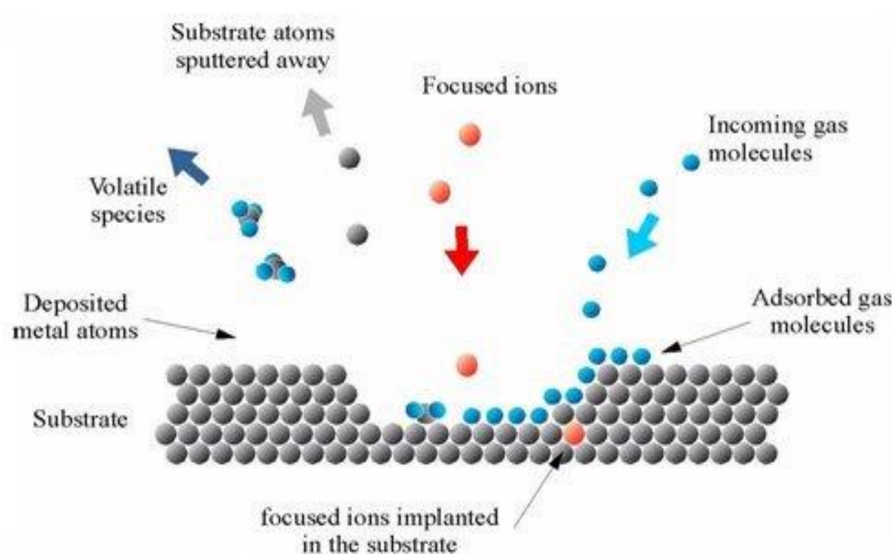

Figure 2.6: Schematic diagram of the Ion Milling with Enhanced Etching [36]

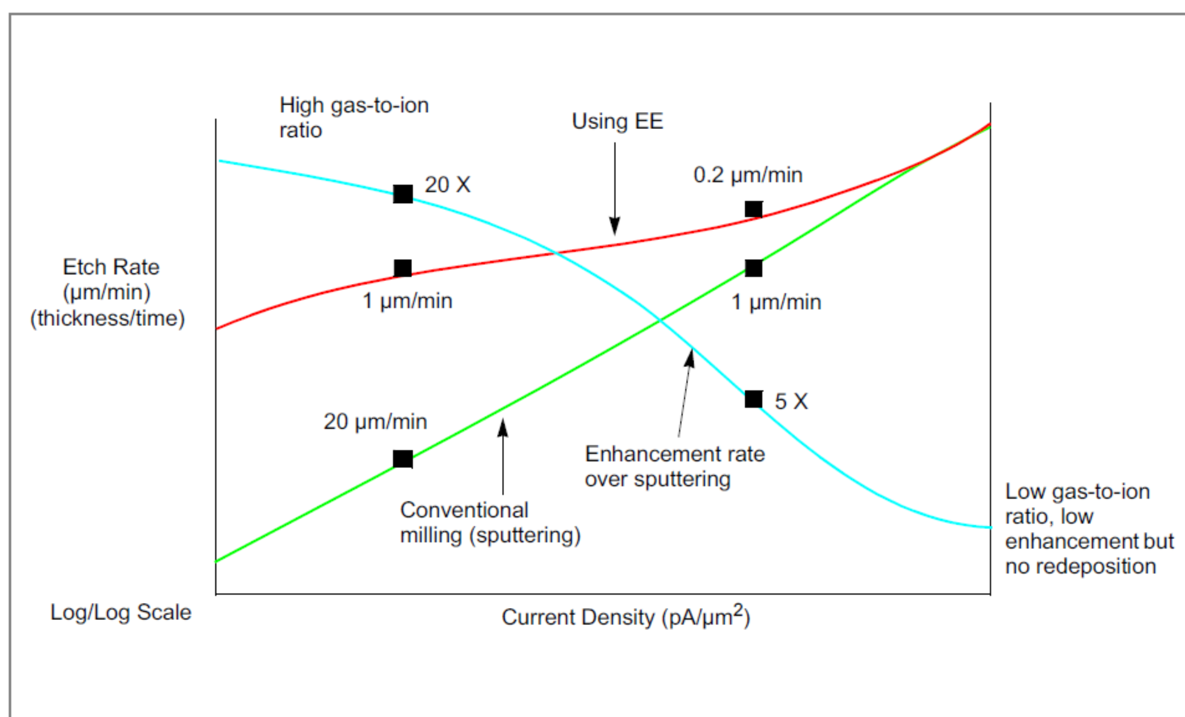

Figure 2.7: Current density vs. Etch rate, variable dependency of gas to ion ratio, [40]

Figure 2.7 explains the relationship between the supplied current density (pA/µm^2) and etch rate (µm/min) due to Enhanced Etching and its dependency of gas flux to ion flux ratio. The etch gas molecules at low current density (pA/µm^2) dominate the etch process. As the beam current density increases the ion beam begins to dominate over etch gas flux [40]. At this point the EE gas supply flow rate can affect the increase in the milling rate (e.g. by using a coaxial needle with XeF_2 when milling SiO_2 or Si) [27, 28, 30, 40].

2.6.3.3 FIB Metal Deposition (Ion Beam Induced Deposition)

A metallic conductive layer or non conducting isolating material can be deposited with the assistance of a precursor gas. For example, metals like platinum (Pt) or insulators like silicon dioxide (SiO_2) can be deposited with either an ion or electron beam. It has been known for some time that metal deposits produced in this way contain carbon from the decomposed precursor as the majority phase and that gallium (Ga) from the incident beam can also be incorporated [41, 42]. The deposition of metallic thin films (Pt or W) using FIB is usually

achieved by the ion beam decomposition of carbon rich precursors (i.e. methylcyclopentadienyl platinum trimethyl (CH3)3(CH3C5H4)Pt for platinum deposition and tungsten hexacarbonyl ($W(CO)_6$) for tungsten). Such precursors lead to films with high resistivity (ρ) with a negative temperature coefficient of resistivity $\beta = \frac{1}{\rho}\frac{d\rho}{dT}$. This is typical of carbon and can vary by a large amount depending on the carbon content in the film [43]. FIB deposition can be classified into two major categories: chemical assisted deposition (FIB-Chemical Vapour Deposition technique), and direct deposition. In chemical assisted deposition, the ion beam decomposes a source gas that reacts into the sample surface resulting in film deposition, a process which is also known as "beam excitation surface reaction technology" [28]. As in the case of etch enhancement the outcome – milling or deposition – depends on the balance of fluxes between ions and precursor molecules. This is not simply a matter of current density compared with precursor molecular flux but is also determined by scan strategy, in particular by the so-called loop time [24]. Ion beam deposition has significantly higher deposition rate than the electron beam equivalent due to its ability to produce greater secondary electron yield [45]. FIB systems can be used to fabricate patterns by using pattern generators such as the Raith Elphy (from Raith GmbH**).** Figure 2.8 explains the dependence of the deposition rate of the FIB system on the current density [40]. Region A shows the effect of a lower current density resulting in a slower deposition rate. This type of deposition is used for larger patterns. In region B with the higher current density, the most efficient deposition takes place due to maximum utilisation of the precursor gas molecules. This region is used for medium sized patterns. In region C, the deposition rate efficiency reduces with an increase in the current density and eventually milling starts instead of deposition due to an increase in the relative number of ions.

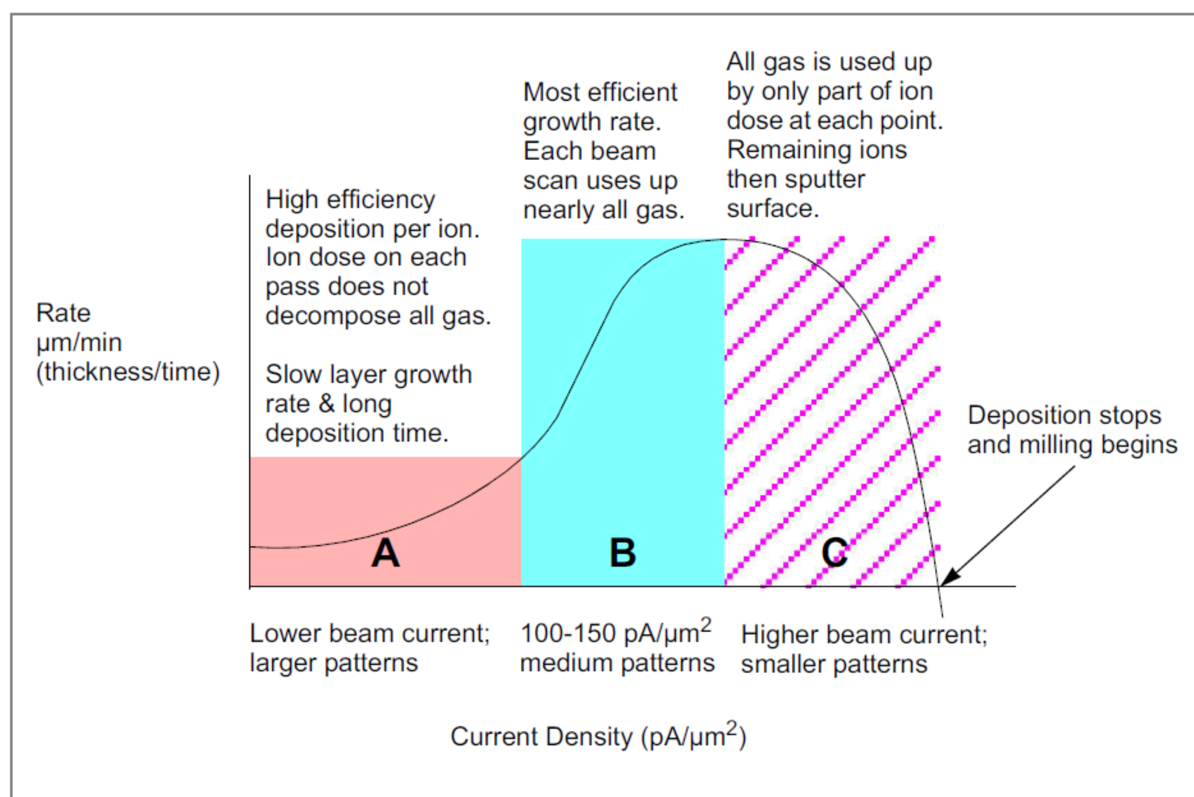

Figure 2.8: Current density vs. deposition rate in the FIB system. [40]

2.7 Atomic Force Microscope System (AFM)

Atomic Force Microscopy (AFM) is a significant tool for the analysis and characterisation of the physical properties of the surfaces of MEMS and NEMS devices. AFM also has important applications in bioscience and biomedical engineering. AFM, also known as Scanning Force Microscopy (SFM), is characterised by high lateral (6Å) and vertical (1Å) resolutions and a high signal-to-noise ratio [46-49]. The associated system of Scanning Tunnelling Microscope (STM) uses tunnelling electrons instead of force signals. STM was invented by Gerd Binnig and Heinrich Rohrer in the early 1980s at IBM Research, Zurich (Nobel Prize. 1986). Eventually Binnig, Calvin Quate and Christoph Gerber developed the STM further and gave birth to the modern and more sophisticated Atomic Force Microscope (AFM) [49]. STM has a very significant disadvantage over AFM which is that it only has the ability to image conducting or semi conducting surfaces [50]. AFM applications include

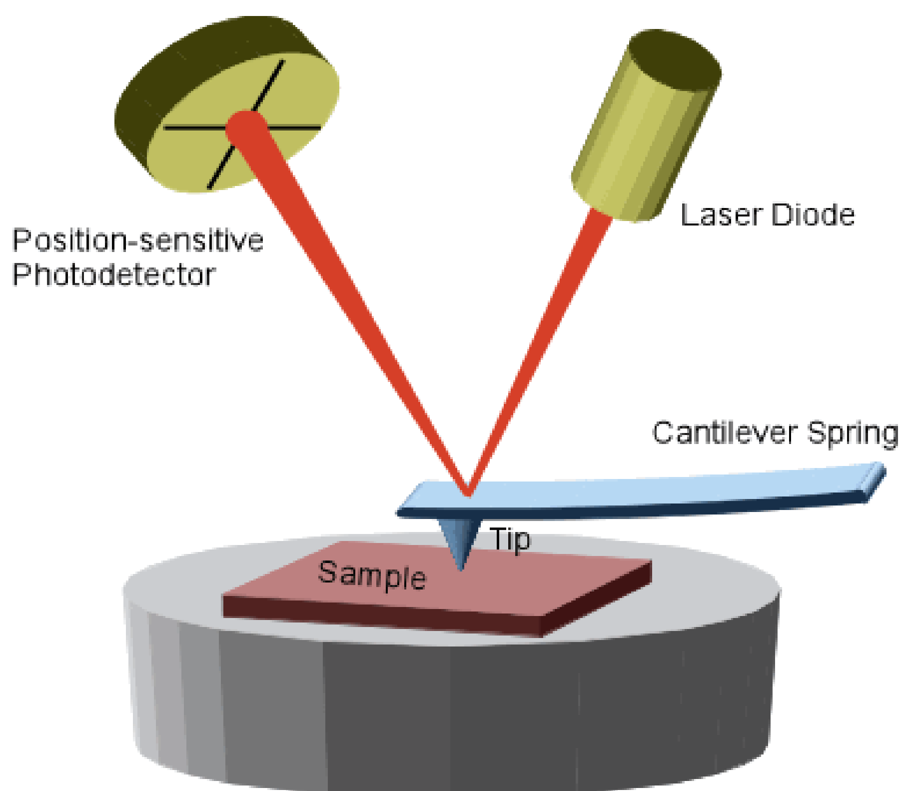

Figure 2.9: Schematic of modern system developed by Gerhard Meyer and Nabil M. Amer [53].

imaging, characterisation and analysis (i.e. Young's modulus, fracture strength etc.), measurement (i.e. force, deflection etc, described in Chapter 7). AFM is one of the preferred characterisation methods for the study of biological molecules.

2.7.1 Principle of Operation and Hooke's Law

Gerhard Meyer and Nabil M. Amer [51] introduced the modern AFM system in 1990, in which an optical laser beam is reflected by the AFM cantilever to the position photosensitive detector. Figure 2.9 [53] is a schematic of a typical AFM system. The AFM cantilever tip is attached to a cantilever spring. The typical tip radius is ~10 – 50 nm. AFM tips and cantilevers are almost always fabricated from silicon (Si) or silicon nitride (Si_3N_4). Figure 2.10 shows the SEM image of the AFM cantilever tip with tip radius of ~ 10 nm, used in the experiments described in Chapter 6 and Chapter 7. When the AFM tip comes into contact with the sample surface, initially the tip is pulled towards the surface atoms. The

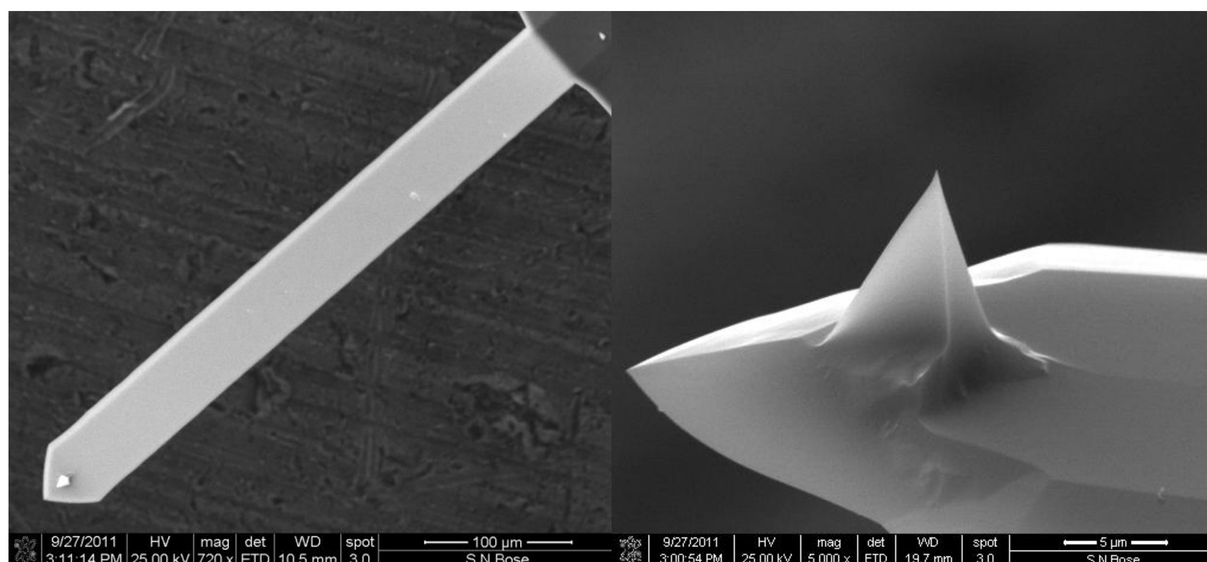

Figure 2.10: SEM image of the AFM cantilever tip with a tip radius of 10 nm.

phenomenon of attractive and repulsive forces between molecules was first observed by the Dutch scientist Johannes Diderik van der Waals and this force generated in the process is called the *van der Waals* force. Further loading of the AFM tip increases its deflection and generates a bending moment in the cantilever. In contact mode, the magnitude of the force generated is in the range of 0.1 - 1 nN. The position photosensitive detector is connected with the computer interface device which converts the deflection signal into a digital signal for computer processing and analysis.

The generated force can be calculated using Hooke's Law, $F = -k\delta$. Where F is the force generated by tip deflection, δ is the magnitude of the deflection in the vertical direction and k is the spring constant of the AFM cantilever. Figure 2.11 demonstrates a typical example of the manipulation path of the AFM tip showing the force generated due to the AFM tip movement (z position) on a solid surface sample. The blue region represents the *van der Waals* force generated between the sample atoms and the AFM cantilever tip. The red region shows the generation of force during the approach of the AFM tip in the contact mode. Almost all major applications of AFM such as imaging, force and deflection measurement are

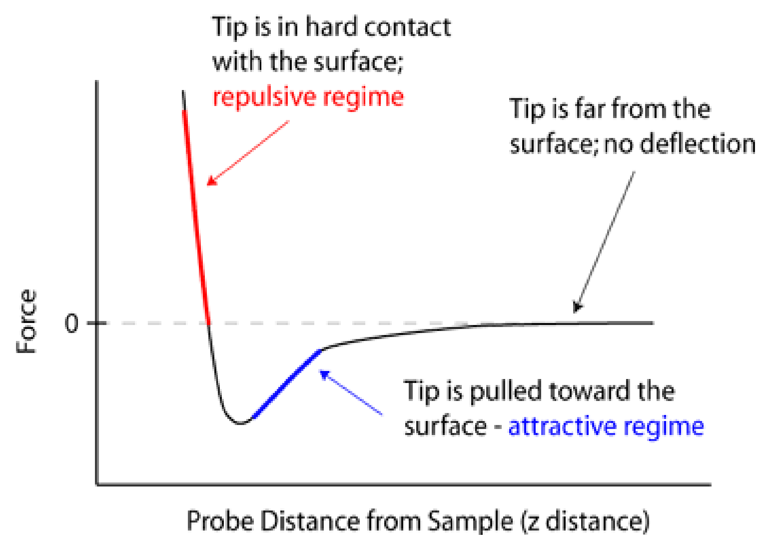

Figure 2.11: Example of force vs z position of the AFM tip. This shows the typical manipulation path of the AFM probe [54].

dependent on the cantilever properties of spring constant and resonant frequency. The spring constant, k_c, can be given by the Equation 2.3 [50, 55]

$$k_C = \frac{3EI}{L^3} \tag{2.3}$$

where E is the Young's modulus of the cantilever, I is the moment of inertia and L is the length of the cantilever. The moment of inertia I of a cantilever with thickness t and width w is $I = wt^3/12$.

2.7.2 Imaging by AFM

The imaging process can be done with three different modes: Contact mode, Non-contact mode and Tapping mode. The most commonly used imaging mode is contact mode, where a position photosensitive detector (PDS) measures the deflection in the cantilever beam caused by horizontal scanning (raster scanning) of the AFM tip on the surface of the substrate. The PDS transfers these signals to the computer interface in order to generate the topographical image of the substrate surface. The resolution of the image produced by this method is

equivalent to the diameter of the tip [50] and is increased by selecting a cantilever tip of lower diameter. Contact mode generates *van der Waals* force between the cantilever tip and the sample molecules while imaging. However, the contact mode of imaging can be achieved in two different ways: by keeping the deflection level of the cantilever tip at constant point and moving the sample height during the imaging or by keeping the sample height constant and recording the deflection signal by position photosensitive detector (PDS).

The second type of imaging mode is non-contact mode. In this case the tip of the cantilever is not in direct contact with the sample molecules but instead it oscillates above the zone of *van der Waals* forces. When the AFM tip enters the zone of *van der Waals* forces, it determines the concentration of the forces and evaluates them as a function of the tip height from the substrate [50]. *Van der Waals* forces reduce the resonant frequency of the oscillating tip and this force concentration as a function of height is used (by adjusting height) to maintain constant amplitude of oscillation. Computer interface feedback uses this height adjustment data to construct the image of the substrate. The biggest advantage of this method is that it does not cause wearing of the cantilever tip. This type of imaging is ideal in the case of organic material or biomedical samples such as DNA.

The third type of imaging is the Tapping mode, which may be thought of as the intermediate mode between contact mode and non-contact mode. The cantilever tip in this mode oscillates vertically at a given frequency, unlike the other two modes. Amplitude in this mode is set 50 - 60 % lower than the non-contact mode, and is maintained at a constant level using the piezoelectric actuator by controlling the height between the cantilever tip and sample surface. Tapping mode does not create friction between the tip and the sample surface thereby minimising damage to the sample with the advantage of very high resolution [50, 56]. The amplitude of the oscillation is 10 fold higher than the *van der Waals* forces zone to avoid the

adhesive meniscus forces and to avoid generation of shear force between the tip and the sample. This imaging mode is often used in non solid or biological samples.

2.7.3 Force Calibration and Deflection Measurement

A significant feature of the Atomic Force Microscopy is the ability to directly measure the force generated in NEMS or MEMS devices, where the force is an operative function (for example the bimorph cantilever in Chapter 6 or a strain gauge device). Figure 2.11 explains the force as a function of z displacement of the AFM cantilever tip. If an AFM cantilever is in contact with the sample surface and if the sample surface generates a vertical displacement, the AFM cantilever will acquire a bending moment as a direct result of the displacement and the reaction force (repulsive contact force) generated by the sample. AFM has the ability to measure this force directly from the system using Hooke's Law. This function of AFM is called Force Mode and Figure 2.11 can be described as force vs displacement curve. The force vs displacement curve and the Force Mode function of the AFM are important for the evaluation of material properties. For example, the Young's modulus and the fracture strength of a material were calculated by Wu *et al* [12] and they highlighted the fact that nanowires have different properties than their bulk material. Chapter 7 describes the use of AFM to highlight the phenomenon of instability generated in gold nanowires and atomic mobility below the critical diameter. Commercially available AFMs can measure forces as low as 0.1 nN with a very sensitive cantilever tip and controlled working environment. As already discussed, displacement in the cantilever beam is measured by position photosensitive detector (PDS) and converted to force by Hooke's Law knowing the spring constant of the cantilever, which is provided by the manufacturer. However the actual value of the spring constant should be calibrated before an experiment is started. This can be achieved by any of these three methods [58]: from the cantilever geometry, using the

reference cantilever or using the thermal noise method. The material of the cantilever is indeed vulnerable to thermal fluctuations. For example, Chapter 7 describes how every 0.83° (K or C) fluctuation in temperature can cause a cantilever made from Si_3N_4 to deflect 1 nm. (The thermal energy generated at a certain temperature can be evaluated by Boltzmann constant [58]).

2.8 References

[1] Yeh W. J., Yang K., *Fabrication of Uniform Magnetic Nanowire Array*, Journal of Physics, 2007, Conference Series **61**: p 1299–1302.

[2] Tonucci R. J., Justus B. L., Campillo A. J., Ford C. E., *Nanochannel Array Glass*. Science. 1992 **258**: p 783.

[3] Shi Z. Wu S. Fairbridge C. Szpunar J. A., *Controlling palladium nanowire size through electroless deposition process*, Micro & Nano Letters, 2008, **3**(2) p 50-56.

[4] Kamalakar M. V., Raychaudhuri A. K., *A Novel Method of Synthesis of Dense Arrays of Aligned Single Crystalline Copper Nanotubes Using Electrodeposition in the Presence of a Rotating Electric Field.* Adv. Mater. 2008, **20**: p 149–154.

[5] Routkevitch, D. Tager, A. A., Haruyama, Junji, Almawlawi, D., *Nonlithographic nano-wire arrays, fabrication, physics, and device applications,* IEEE Transaction on Electron Devices, 1996 **43** (10): p 1646 - 1658.

[6] Kondo Y., Takayanagi K., *Synthesis and Characterization of Helical Multi-Shell Gold Nanowires,* Science, 2000, **289**(5479), p 606-608.

[7] Tosatti E., Prestipino S., *Weird Gold Nanowires*, Science, 2000: **289**(5479): p 561 – 563.

[8] Kondo Y., Takayanagi K., Hideaki Ohnishi, *Suspended Gold Nanowires - Ballistic transport of Electrons*, JSAP International, **3**, 2001.

[9] Candace K. Chan, Hailin Peng, Gao Liu, Kevin McIlwrath, Xiao Feng Zhang, Robert A. Huggins, Yi Cui, *High-performance lithium battery anodes using silicon nanowires,* Nature Nanotechnology, 2008, **3**: p 31 - 35.

[10] Lien T. Ngo, Dorothe Almcija, John E. Sader, Brian Daly, Nikolay, Petkov, Justin D. Holmes, Donats Erts, John J. Boland, *Ultimate-Strength Germanium Nanowires,* Nano Letters, 2006, **6**(12): p 2964-2968.

[11] Celik E., Guven I., Madenci E., *Mechanical characterization of nickel nanowires by using a customized atomic microscope in scanning electron microscope*, Electronic Components and Technology Conference (ECTC), 2011 IEEE 61st, 2011, p 1999–2006

[12] Wu B, Heidelberg A., Boland J. J., *Mechanical properties of ultrahigh-strength gold nanowires*, Nature Materials, 2005, **4**: p 525–529.

[13] Naik J. P., Prewett P. D., Das K., Raychaudhuri A. K., *Instabilities in Focused Ion Beam-Patterned Au Nanowires*, Microelectronics Engineering, 2011, **88:** p 2840-2843.

[14] Toimil-Molares M. E., Balogh A. G., Cornelius T. W., Neumann R., Trautmann C., *Fragmentation of nanowires driven by Rayleigh instability*, Appl. Phys. Lett., 2004, **85:** p 5337

[15] Sun Y., Mayers B., Xia Y., *Transformation of silver nanospheres into nanobelts and triangular nanoplates through a thermal process.* Nano Letters, 2003, **3**(5): p 675–679.

[16] Lord Rayleigh, Proc. Longon Math. Soc, 1878, **10**: p 4.

[17] Nichols F. A., Mullins W. W., *Surface (Interface) and Volume Diffusion Contributions to Morphological Changes Driven by Capillarity.* Trans. Metal. Soc. AIME, 1965**, 233**: p 1840.

[18] Karim S., Toimil-Molares M. E., Balogh A. G., Ensinger W., Cornelius T. W., Khan E. U., Neumann R., *Morphological evolution of Au nanowires controlled by Rayleigh instability*, Nanotechnology, 2006, **17**: p 5954-5959.

[19] Kelly M. J., *Intrinsic top-down unmanufacturability*. Nanotechnology, 2011, **22**: p 245303.

[20] Rodel, J., Glaeser, M., *High-temperature healing of lithographically introduced cracks in sapphire*. J. Am. Ceram. Soc., 1990, **73**: p 592-601.

[21] J Plateau, *Transl. Annual Reports of the Smithsonian Institution*, 1873, p 1863.

[22] Bid A., Bora A., Raychaudhuri A. K., *Low frequency conductance fluctuations (1/f_ noise) in 15nm Ag nanowires-Implication on its stability*, Phys. Rev B, 2005, **72**: p 113415.

[23] Yu H. H., Suo Z., *An axisymmetric model of pore-grain boundary separation*. J. Mech. Phys. Solid., 1999, **47**: p 1131-1155.

[24] Prewett P. D., Mair G. L. R., *Focused ion beams from Liquid metal ion source,* John Wiley & Sons, 1991.

[25] Rivera V. A. G., Ferri F. A., Silva O. B., Sobreira F. W. A., Marega E. Jr., *Light Transmission via Sub wavelength Apertures in Metallic Thin Films*, (edited by Ki Young Kim), October 24, 2012.

[26] Volkert C. A., Minor A. M., *Focused Ion Beam Microscopy and Micromachining*. MRS Bulletin, 2007, **32**: p 389-399.

[27] Lucille A. Giannuzzi (FEI Company), Fred A. Stevie (North Carolina State University) *Introduction to Focused Ion Beams*: *Instrumentation, Theory, Techniques and Practice*, (2005) Springer Science + Business Media, Inc., Boston.

[28] Adnan Latif, *Nanofabrication Using Focused Ion Beam*, PhD Thesis, 2000, Darwin College, Cambridge.

[29] Hossein Ostadi Valiabad, *Micro and Nano Scale Three-Dimensional reconstruction of Polymer Electrolyte Fuel Cell Porous Layer,* PhD Thesis, 2011, University of Birmingham.

[30] FEI Company Manual, Focused ion beam technology, *Capabilities and Applications*.

[31] Nikawa K., *Applications of focused ion beam technique to failure analysis of very large scale integrations: A review*, J. Vac. Sci. Technol. B, 1991, **9**: p 2566.

[32] Prewett P. D., *Focused ion beams-microfabrication methods and applications*, Vacuum, 1993, **44**: p 345-351.

[33] Abramo M. T., Hahn L. L., *The application of advanced techniques for complex focused-ion-beam device modification*, Microelectron. Reliab., 1996, **36**: p 1775-1778.

[34] Mulders J. J. L., De Winter D. A. M, Duinkerken W. J. H. C. P., *Measurement and calculations of FIB milling yield of bulk metals,* Microelectronic Engineering, 2007, **84**: p 1540-1543.

[35] Gérard Barbottin, André Vapaille, *New Insulators Devices and Radiation Effects*, Elsavier Science B., 1999, **3**: p 2-938.

[36] Focused Ion Beam, Wikipedia, (http://en.wikipedia.org/wiki/Focused_ion_beam).

[37] Bruce Geol, Army Research Laboratory data, ARL-MR-1, 1993, p 14.

[38] Vasile M. J., Niu Z., Nassar R., Zhang W., Liu S., *Focused ion beam milling: Depth control for three-dimensional microfabrication*, J. Vac. Sci. Technol. B, 1997, **15**: p 2350-2354.

[39] Ishitani T., Ohnishi T., Madokoro Y., Kawanami Y., *Focused ion beam ‘‘cutter’’ and ‘‘attacher’’ for micromachining and device transplantation*, J. Vac. Sci. Technol. B, 1991, **9**: p 2633.

[40] FEI™ Application note, *Using beam chemistries with SEM*, FIB and Dual Beam™ for surface modification.

[41] Lin J. F., Bird J. P., Rotkina L., Bennett P. A., *Classical and quantum transport in focused-ion-beam-deposited Pt nanointerconnects*, Appl. Phys Lett., 2003, **82**: p 802.

[42] Fernández-Pacheco A., De Teresa J. M., Córdoba R., Ibarra M. R., *Metal-insulator transition in Pt-C nanowires grown by focused-ion-beam-induced deposition*, Phs. Rev. B., 2009, **79**: p 174204.

[43] Pe˜nate-Quesada L., Mitra J., Dawson P., *Non-linear electronic transport in Pt nanowires deposited by focused ion beam*, Nanotechnology, 2007, **18**: p 215203.

[44] Manotosh Chakravorty, Kaustuv Das, A. K. Raychaudhuri, J P Naik and P D Prewett, *Temperature dependent resistivity of platinum–carbon composite nanowires grown by focused ion beam on SiO_2/Si substrate*. Microelectronic Engineering. 2011, **88:** p 3360–3364.

[45] FEI™ Application note, Beam Induced Deposition of Gold.

[46] Abu-Lail N., Camesano T. A., *Dekker Encyclopedia of Nanoscience and Nanotechnology*, Worcester Polytechnic Institute, Worcester, Massachusetts, USA, p 109.

[47] Scheuring S., Fotiadis D., Moller C., Muller S. A., Engel A., Muller D. J., *Single proteins observed by AFM*, Single Mol., 2001, **2**: p 59–67.

[48] Binning G., Quate C.F., Gerber C.H., *Atomic Force Microscope*. Phys. Rev. Lett., 1986, **56** (9): p 930–933.

[49] Muller D.J., Anderson K., *Biomacromolecular imaging using atomic force microscopy*. Trends Biotechnol., 2002, **20** (8), S45–S49.

[50] Bharat Bhushan, *Springer Handbook of Nanotechnology*, © Springer-Verlag Berlin Heidelberg,2004, p 599.

[51] Meyer G., Amer N. M., *Optical beam deflection atomic force microscopy: The NaCl (001) surface*, Appl. Phys. Lett., 1990, **56**: p 2100.

[52] Meyer G., Amer N. M.*, Simultaneous measurement of lateral and normal forces with an optical beam deflection atomic force microscope* , Appl. Phys. Lett., 1990, **57**: p 2089.

[53] AFM (Atomic Force Microscope), (http://www3.physik.uni-greifswald.de/method/afm/eafm.htm).

[54] Atomic Force Microscopy, http://www.nanoscience.com/products/afm/technology-overview/.

[55] Gere J. M., Timoshenko S. P., *Mechanics of Materials*, 1990, Boston, Massachusetts, **Chapter 5**, p 868-882.

[56] Dekker M., *Dekker Encyclopedia of Nanoscience and Nanotechnology*, 2004, p 133-143.

[57] Technical Note, © JPK Instruments AG, (www.jpk.com), p 1 – 8.

[58] Cappella B., Dietler G., *Force-distance curves by atomic force microscopy*, Surface Science reports, 1999, **34**: p 1–104.

Chapter 3

Fabrication and Characterisation Techniques

3.1 Introduction

In this chapter, various types of methods used to fabricate and characterise nanowires are discussed. Some methods are significantly important to carry out the present work. For a detailed understanding of fabricated nanowire properties, especially in the region below 50 nm, Focused Ion Beam (FIB) lithography is used as a primary method for fabrication. However, having an understanding of other fabrication methods is also significantly important in the fabrication of nanowires with the desired dimensions. Fabrication techniques like Photolithography, Electrodeposition, Electron Beam Lithography and Plasma Etching are also used for the fabrication of contact pads for electrical and mechanical measurements. Atomic Force Microscopy (AFM) is used to carry out studies of the mechanical properties of the fabricated nanowires. Scanning Electron Microscopy (SEM) is used for characterisation of the results. Deep Reactive Ion Etching (DRIE) is used to fabricate the silicon stencil masks for the contact pads for the electrical measurements as well as to fabricate free standing nanowire bridges for the mechanical measurements.

3.2 Photoresist Spin Coating Process for FIB Fabrication

Photolithography, also known as Ultra-Violet (UV) lithography, is a technique to fabricate a particular pattern using photo masks and positive or negative photo sensitive resist on a substrate. Ultimately this process can be used in addition to electrodeposition to fabricate three dimensional (3D) structures. Photoresist is an organic compound sensitive to UV light

exposure. The way the photoresist reacts to the UV light depends on the type. In the positive type, exposure decomposes a development inhibitor and developer solution only dissolves photoresist in the exposed areas. However, the negative type photoresist photo-polymerises the exposed area and renders it insoluble to the developer solution. The combined process is widely used in fabrication of MEMS (Micro Electro Mechanical System) and NEMS (Micro Electro Mechanical System) devices. Photolithography incorporates the following step by step process; Sample Preparation, Photo Resist Coating, Pre-Baking (Soft Baking), Mask Alignment, Ultra Violet Exposure, Development and Post-Baking (Hard Baking). The use of this process in our particular case was to try and fabricate nanowires with a width of a few nanometres, as well as contact pads for the nanowire electrical measurements.

Figure 3.1 shows the schematic of the spin coating process for the photo resist during the photolithography process. Silicon (Si) wafer of 10 cm (4 in) in diameter and 0.5 mm in thickness was used as a substrate. Si wafer was sputter coated with a gold layer of ~ 10 nm in thickness for the electrical conductivity for the electrodeposition. Photo resist S1805 was spin

• **Spin on**

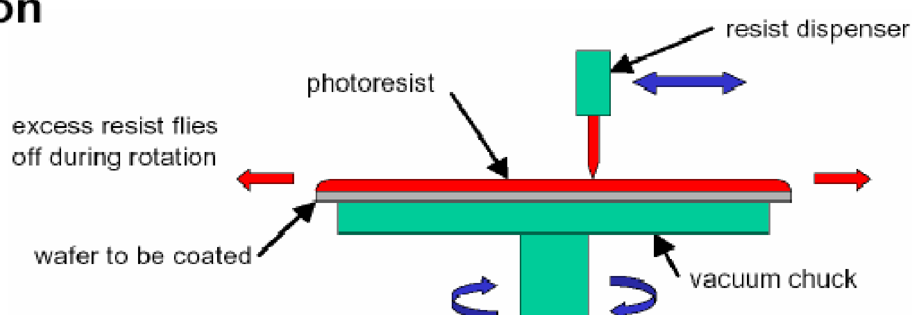

Thickness of PR $t := K \cdot S \cdot \left(\frac{\nu}{\omega^2 \cdot R^2}\right)^{\frac{1}{3}}$

t = thickness
K = constant
S= fraction of solids
υ= viscosity
ω= angular velocity

Figure 3.1: Schematic diagram of the spin coating process during photolithography (Ref: University of Birmingham cleanroom laboratory instruction booklet)

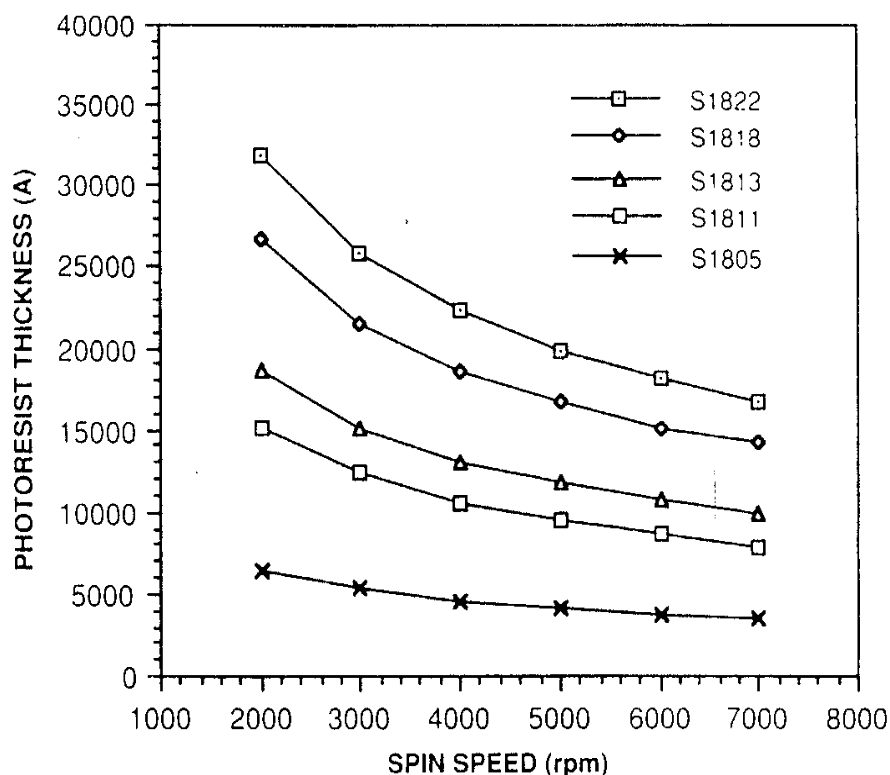

Figure 3.2: Spin Speed Curves [1]
Microposit S1800 Photo Resist Undyed Series

coated with a uniform thickness of 300 nm using the spin speed of 6000 rpm based on the datasheet provided by the manufacturer of S1805 [1], as shown in Figure 3.2. This figure shows that the thickness of the photo resist coating can be controlled by the speed of the spinner. Theoretical curve between thickness vs. spin speed is shown in Figure 3.2 [1]. The coated photo resist was soft baked at 115 °C for 60 seconds. After cooling down to room temperature the coated substrate was cut to the sample size of 1 cm x 1 cm using a diamond cutter for further experiments, such as FIB milling or electrodeposition.

3.3 Design and Fabrication of Si Stencil Mask

Electrical measurements carried out on the fabricated nanowires (described in Chapter 6) used contact pads in order to connect the nanowires to the outside electrical source. Photolithography was used in order to fabricate the contact pads, where the process uses SPR220-7.0 photoresist and photo masks. SPR220-7.0 is a positive tone photo resist and the

photo mask was designed and outsourced to *J D Photos Tools, UK,* who use Pulse Xenon Flash technology for developing emulsion film masks. Figure 3.3 shows the design for the emulsion film mask used to fabricate the contact pads as well as the Si stencil mask for the direct deposition of the contact pad on the chip. The typical substrate used in our experiments is a 7.5 x 7.5 mm^2 silicon chip with an etched square window of 200 µm x 200 µm. There is a silicon nitride (Si_3N_4) membrane, of a thickness of 200 nm, covering the entire chip. If the contact terminals are fabricated directly onto the silicon nitride (Si_3N_4) membrane using the photolithography process, it may cause damage to the membrane. This type of photolithography process directly onto the chip involves hard baking. The change of temperature makes the membrane go through an expansion and contraction process after which the membrane does not remain flat but sags below the surface plane of the chip. Gold deposition (for the contact pads) after photolithography and the lift off process may also cause damage to the membrane. Therefore photolithography directly on the silicon nitride

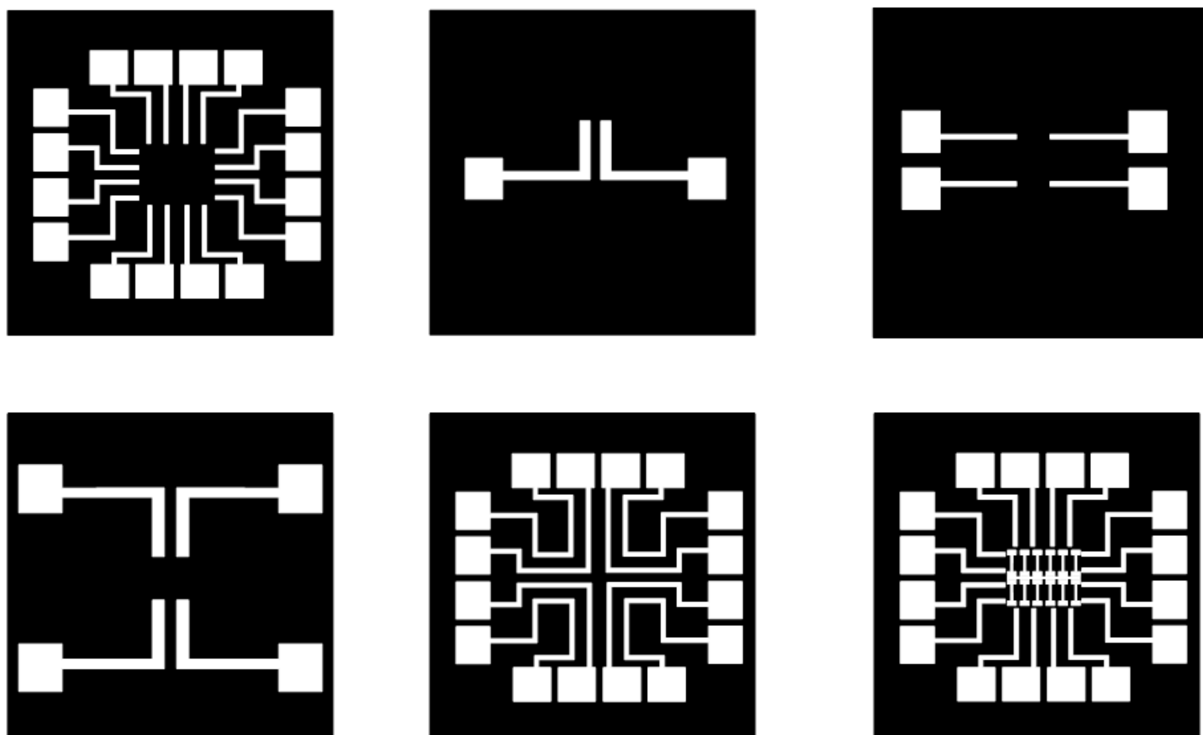

Figure 3.3: Designs used for the emulsion film mask to fabricate contact pads as well as the Si stencil mask for the direct deposition of the contact pad on the chip

(Si_3N_4) membrane chip is not recommended in this particular case. A far superior method is to fabricate the contact terminals on the silicon nitride (Si_3N_4) chip using silicon etched stencil masks.

3.3.1 Photolithography

A silicon wafer of 100 mm diameter and 0.5 mm thickness was used as a substrate for stencil mask fabrication. At least one side of the wafer must be mirror polished to avoid damage of the silicon nitride membrane in the evaporation process. The polished side of the wafer was spin coated at the speed of 500 rpm for 5 seconds followed by 2000 rpm for 30 seconds with the positive tone photo resist SPR220-7.0. The thickness of the photo resist at 2000 rpm is approximately 9 μm. The wafer was baked for 120 seconds at 115 $^{\circ}$C on the hot plate and eventually cooled down to room temperature. The photoresist coated silicon wafer was then exposed to UV light using a Canon PLA-501FA mask aligner with the exposure dose of Hg-lamp (12.6 mW/cm^2) for 45 seconds. The pattern was developed using the MF26A developer after the UV exposure. The developed pattern was etched using Deep Reactive Ion Etching in the STS Plasma Etcher. Such type of photoresist can survive up to 1 mm etch in a standard DRIE process [2-3].

3.3.2 Silicon Etching

Silicon etching is a fabrication process to (chemically or using plasma) remove the silicon atoms from the surface of the substrate. The etching process can be classified into two major categories: Wet etching and Dry etching. In Wet etching the etch reactant is extracted from a liquid source and eventually converted into a soluble compound or gas [2]. Dry etching contains Plasma Etching, Sputtering/Ion Beam Etching, Reactive Ion Etching and Deep Reactive Ion Etching. The Dry etching process has significant advantages over the Wet etching process in nanofabrication due to good process control, low particle contamination,

less selective, low chemical consumption and anisotropic/isotropic in nature [2-3]. In the present work, the Deep Reactive Ion Etching process was used to fabricate the silicon stencil mask for the contact pads and the Reactive Ion Etching process was used in the removal of the silicon under the nanowires in order to fabricate a free standing nanowire bridge (use of the nanowire bridge is explained in Chapter 7).

3.3.2.1 Reactive Ion Etching (RIE)

Reactive Ion Etching (RIE) is a fabrication technique to remove the surface material using chemically reactive plasma [4-5]. RIE was used in Chapter 7 to fabricate nanowire bridges which were used to perform mechanical measurements with an Atomic Force Microscope (AFM). In order to fabricate free standing nanowire bridges, gold nanowires were fabricated using the Focused Ion Beam (FIB) milling process on a silicon (Si) substrate and then the silicon material under the gold (Au) nanowire was removed using RIE. The RIE type of Dry etching method can fabricate a highly isotropic profile, have reasonably good selectivity, higher etch rate, etches in all directions with equal speed and moderate bombardment-induced damage to the sample (in this case the gold nanowires). This is achieved by using SF_6/silicon chemistry. This reaction causes the silicon bonds to break and is generally independent of crystallographic orientation. This is what causes the undercut of the gold nanowires as all exposed silicon will get etched as there is no sidewalk passivation [3]. However, this method reduces the prospect of producing high aspect ratio structures and leaves metallic impurities from the chamber walls [2-5]. This is a primary difference between RIE and DRIE process. However in our case it is a little more complicated. That is because we have an inductively coupled plasma etcher which accelerates the ions giving them momentum normal to the original substrate surface. This causes a sort of mechanical abrasion to occur as well as the chemical action and causes a preferential etch at the bottom

of the trenches so that the etch profile is elongated vertically. This means the depth of the etch is greater than the undercut in our case. This effect can be reduced by reducing the DC bias at the substrate. Table 3.1 explains the parameters used for the fabrication of nanowire bridges i.e. RIE process for 100 nm undercut of nanowires with etch rate ~ 750 Å/min (estimated).

Table 3.1: The parameters of RIE for 100 nm undercut of nanowires (Etch rate ~ 750 Å/min)

Parameters	**Etch Cycle**
SF_6 Flow Rate	20 sccm
O_2 Flow Rate	8 sccm
Ar Flow Rate	8 sccm
Pressure	5 mTorr
Duration	80 s
13.56 MHz Platen Power	100 W
RF Coil Power	600 W

3.3.2.2 Deep Reactive Ion Etching (DRIE)

Deep Reactive Ion Etching (DRIE) also known as the Bosch™ Process (because it was patented and named after the company Robert Bosch GmbH) [4] is a modified RIE fabrication technique to achieve very high aspect ratio anisotropic structures, which uses high density induction coupled plasma (ICP). A thin layer (teflon) is deposited on the surface using decomposition of Octafluorocyclobutane (C4F8) gas inside the plasma. The passivation layer is removed by the bombardment of ions carried by ICP in horizontal surfaces. The passivation layer protects the vertical surfaces and Si is only etched from the horizontal surfaces. DRIE was used to fabricate silicon stencil masks to deposit the contact pad material onto the silicon nitride (Si_3N_4) membrane chip (detailed in Chapter 6), which alleviates the

photolithography process on the membrane and ultimately prevents the possible damage of the membrane window. Table 3.2(a) lists the DRIE process parameters used for the fabrication of high aspect ratio stencil masks with an etch rate of ~ 2.5 μm/min (estimated).

Table 3.2(a): The parameters for the standard DRIE etch using the STS Multiplex ICP DRIE etcher (STS Plc., UK). DRIE of masks with Etch rate ~ 2.5 μm/min – estimated)

Parameters	**Etch Cycle**	**Passivation Cycle**
SF_6 Flow Rate	100 sccm	0 sccm
C_4F_8 Flow Rate	0 sccm	85 sccm
Duration	8 s	5 s
13.56 MHz Platen Power	800 W	600 W
RF Coil Power	600 W	600 W

Table 3.2(b): The parameters for the standard oxygen plasma clean using the STS Multiplex ICP DRIE etcher (STS Plc., UK).

Parameters	**Etch Cycle**
O_2 Flow Rate	100 sccm
Duration	10 min
13.56 MHz Platen Power	800 W
RF Coil Power	600 W

3.4 Focused Ion Beam Lithography (FIB)

Focused Ion Beam lithography is a fabrication technique which typically uses Liquid Metal Ion Source (LMIS) [6] of gallium (Ga+) ions. The gallium (Ga+) ions are accelerated towards the substrate at the bottom of the vacuum chamber passing through two electrostatic lenses. The ions bombard the substrate generating positively charged secondary ions and negatively charged secondary electrons; the surface of the substrate is milled microscopically. A precursor gas of methylcyclopentadienyl platinum trimethyl $(CH_3)_3(CH_3C_5H_4)Pt$ is used in an ion induced metal deposition process. In the present work two very similar types of FIB were used: FEI Strata^{TM} Dual Beam 235 FIB/SEM and FEI Dual Beam Helios 600 FIB-SEM. The most widely used metals are platinum (Pt) or tungsten (W), but in the present experiments only platinum (Pt) was used.

3.4.1 FIB on Photo Resist

The samples prepared (Chapter 3.2) by photoresist spin coating process were loaded in to the vacuum chamber of the Focused Ion Beam. Nano channels were developed using bombardment of the liquid metal ion source on the coated sample in the FIB vacuum chamber. The dimensions of the channels were controlled by the computer feedback control panel attached to the FIB instrument. The width of the channel was kept limited to ~ 80 – 100 nm and the depth was controlled until the beam hit the surface of gold layer. Figure 3.4 and Figure 3.5 are the Scanning Electron Microscopy (SEM) images of the nano channel developed using FIB etch. Figure 3.4 shows the nano channel developed without using Enhanced Etching (EE). Without EE the sputtered material removed by the ion beam, damages the side wall of the channels. The narrowing of the trench in the Figure 3.4 demonstrates the redeposition of the sputtered material on to the side walls. Figure 3.5 exhibits the fine shape nano channels developed by the ion beam with EE. This sample could

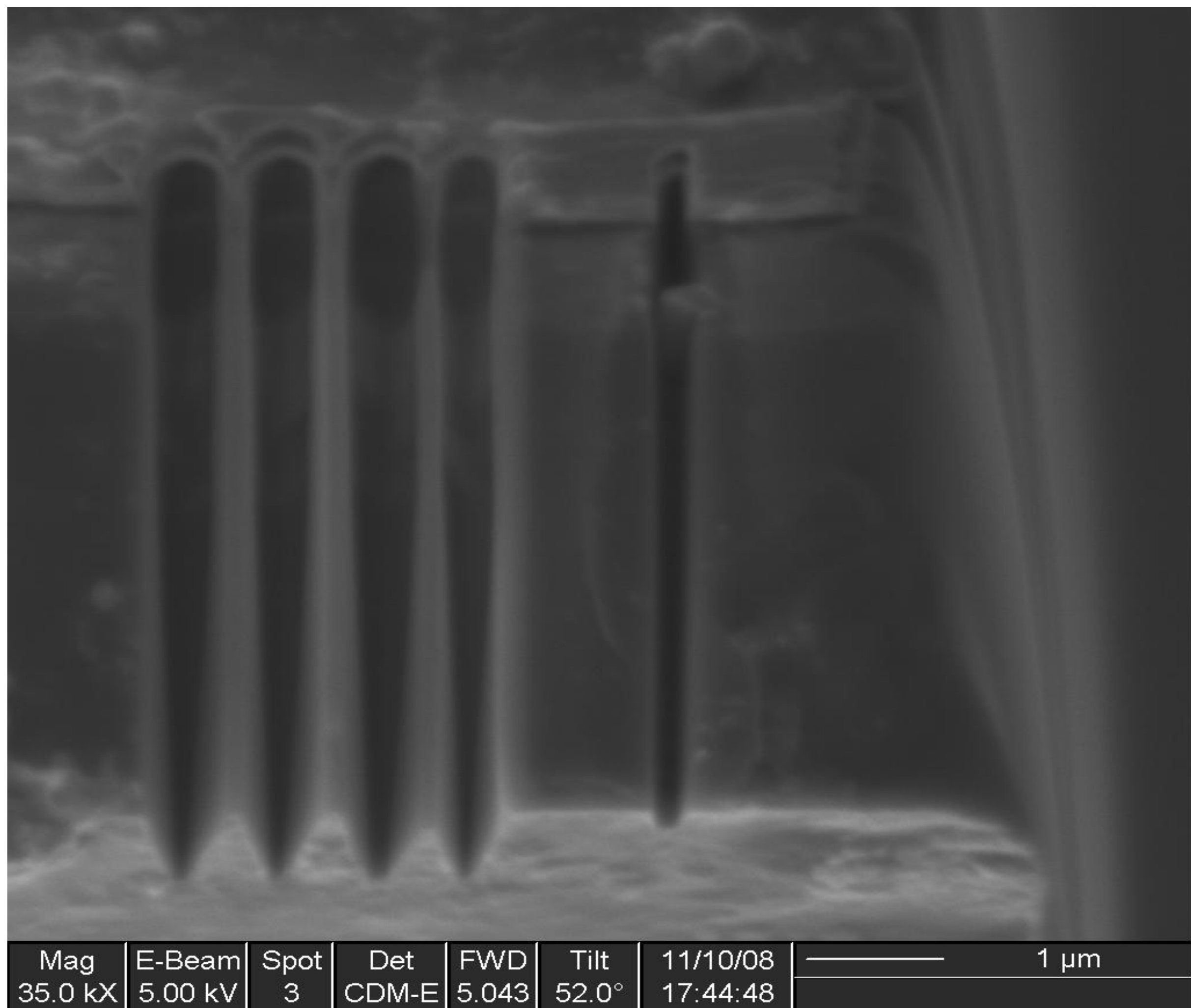

Figure 3.4: SEM image of the nano channels without Enhanced Etch

possibly be used as a template to electrodeposit the material (Ni, Au, Cu etc) into these nano channels for the fabrication of the nanowires. Electron bombardment while taking the SEM images may damage the surface and the edge of the resist S1805. The experiment leads to a simple way of fabricating good quality gold nanowires. Instead of spin coating the photo resist, and depositing the gold, the substrate was sputter coated with gold with a thickness of ~ 50 – 80 nm and milled by FIB system.

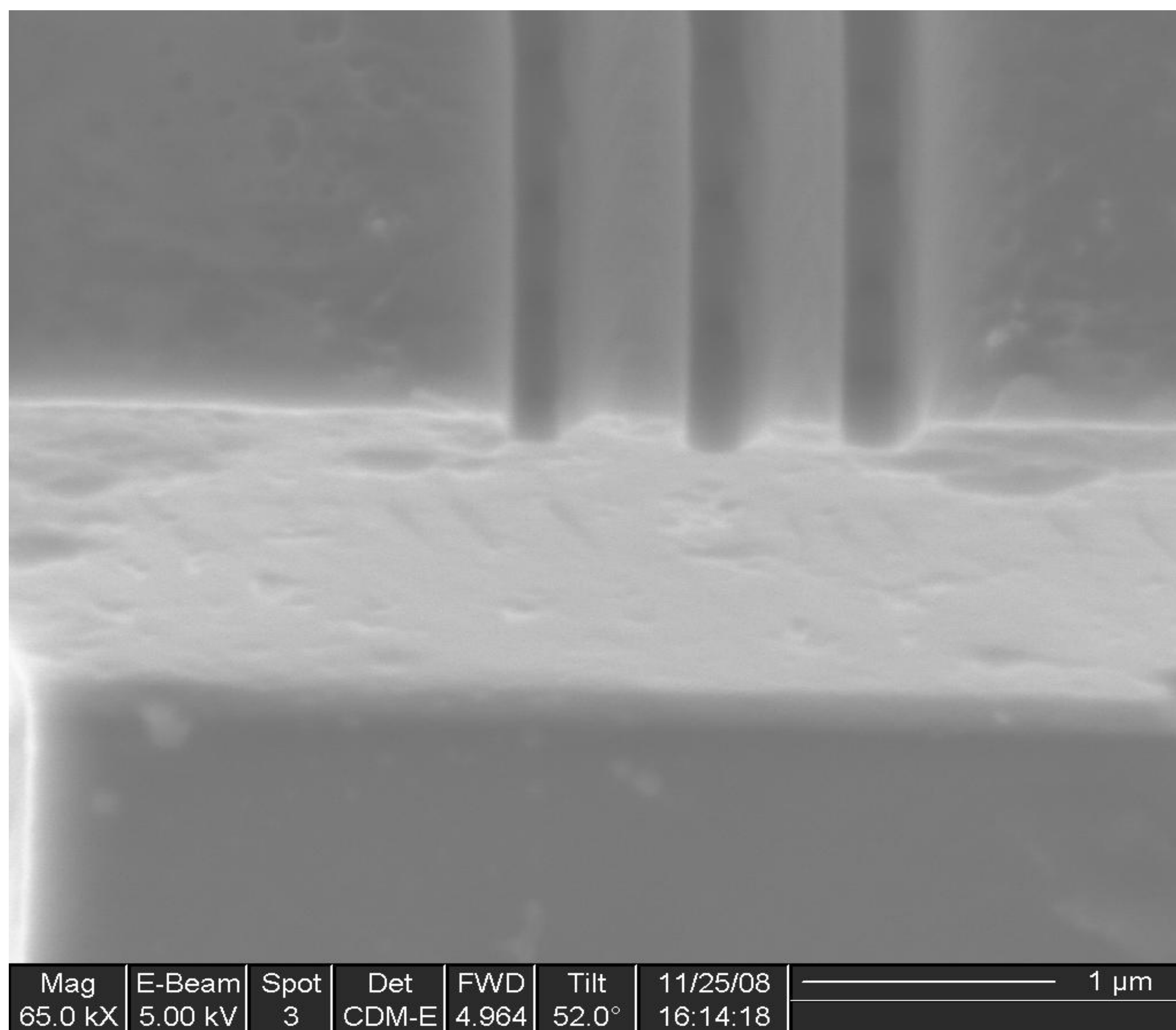

Figure 3.5: SEM image of the nano channels with Enhanced Etch

3.4.2 FIB on Sputter Coated Metallic Thin Film (Au)

The sample of 1 cm x 1 cm with the sputter coated gold surface using Agar automatic sputter coater B7341 before loaded in to the FIB vacuum chamber. B7341 is an advance fully automatic sputter coater. The sputtering current and coating time can be set by digital input. The desired thickness is achieved using thickness monitor, which allows the sputter coated to automatically terminate the task after reaching the target. A similar process of developing the nano channels as in the resist coated substrate was used. However, in this case the area which

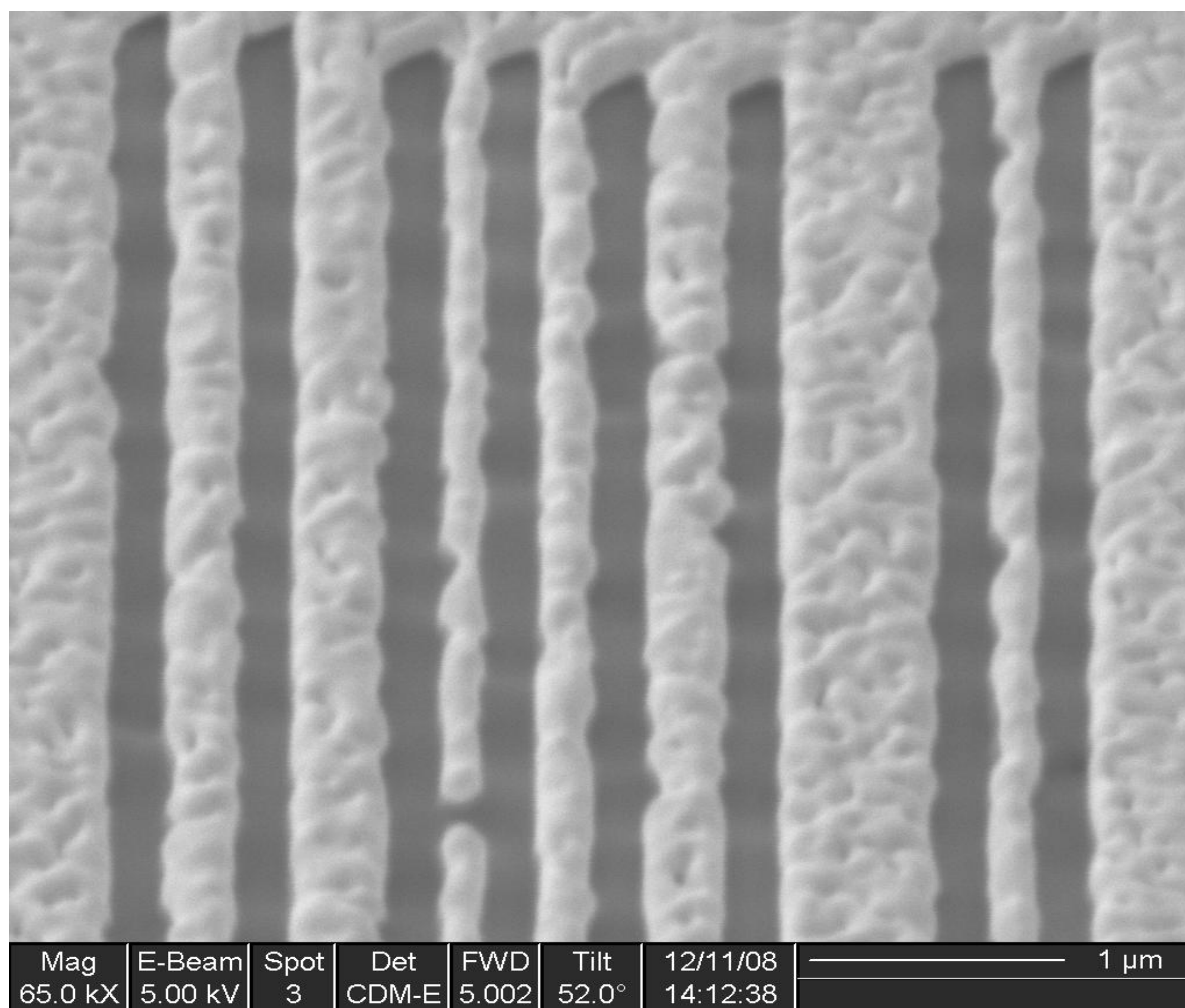

Figure 3.6: SEM image of gold nanowires with different sizes formed between nano channels

is not affected by the bombardment of the liquid metal ions will form nanowires. The size of the nanowire depends on the distance between two nano channels. Figure 3.6 exhibits the area between the two adjacent nano channels forms a nanowire. The minimum size of the stable nanowire achieved by this process was ~ 8 nm (detailed in Chapter 5). Figure 3.7 shows the fabricated nanowires of different sizes on the silicon nitride membrane as a substrate. Pure silicon is a semiconductor; however, silicon nitride is a non conductive material. It is essential to have a nonconductive substrate for the electrical measurement of the fabricated nanowires. The electrical and mechanical measurements on the nanowires are described in Chapter 6 and 7.

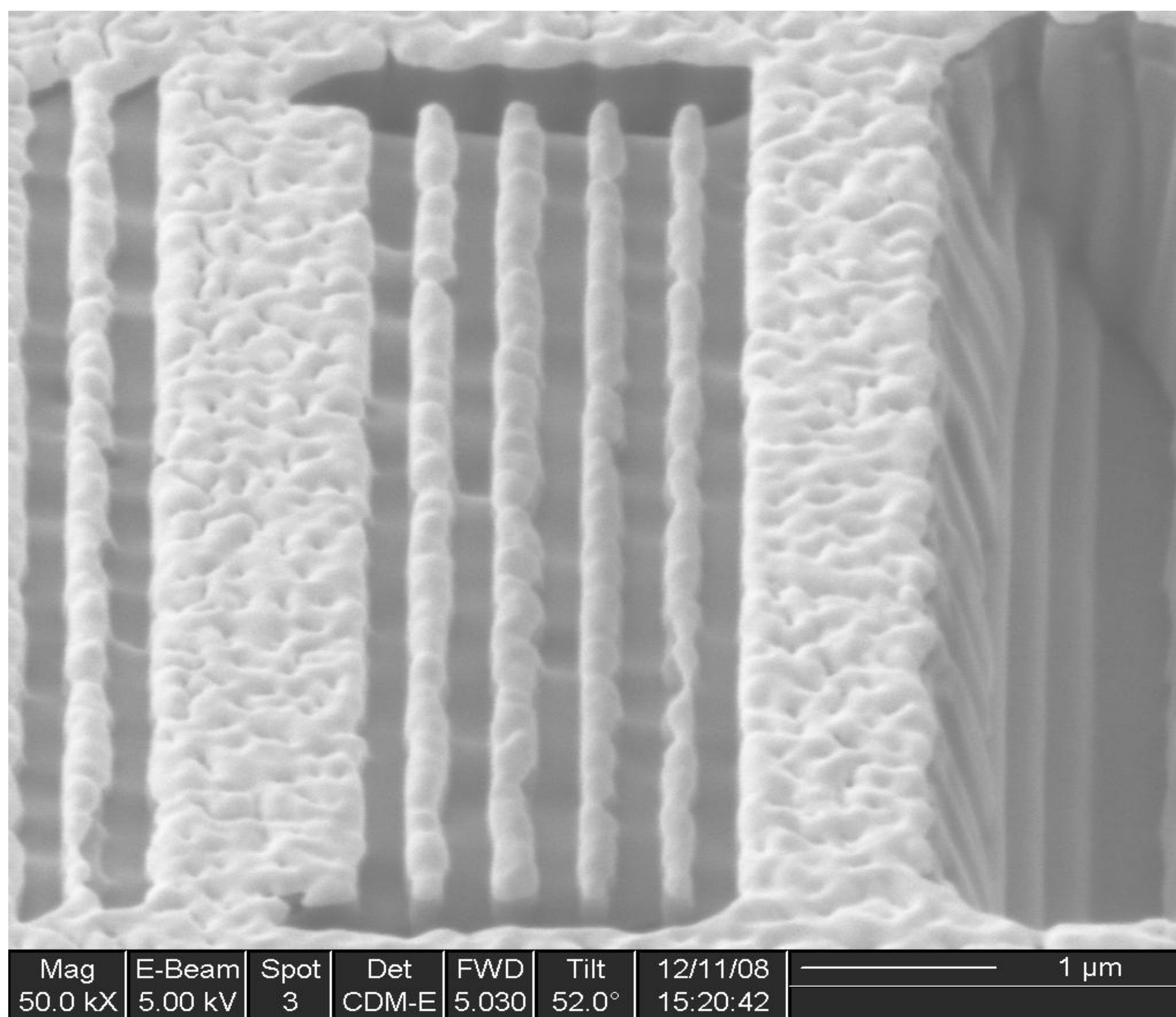

Figure 3.7: SEM image of the different sizes of free nanowires suspended in the Si_3N_4 substrate

3.5 Scanning Electron Microscopy (SEM)

Scanning Electron Microscopy (SEM) is the most commonly used characterisation technique in the nanofabrication process. Nanofabrication processes require high quality images, for the understanding of nanostructures and improvement of synthesis strategies. This makes SEM an indispensable tool for characterisation and therefore it is combined with the latest technology used to fabricate nano structures (e.g. in the FIB/SEM dual beam by FEI). The SEM uses an electron beam focused into a small spot, emitted from a tungsten filament source, to perform parallel linear scans (raster) across the specimen. Eventually the electrons

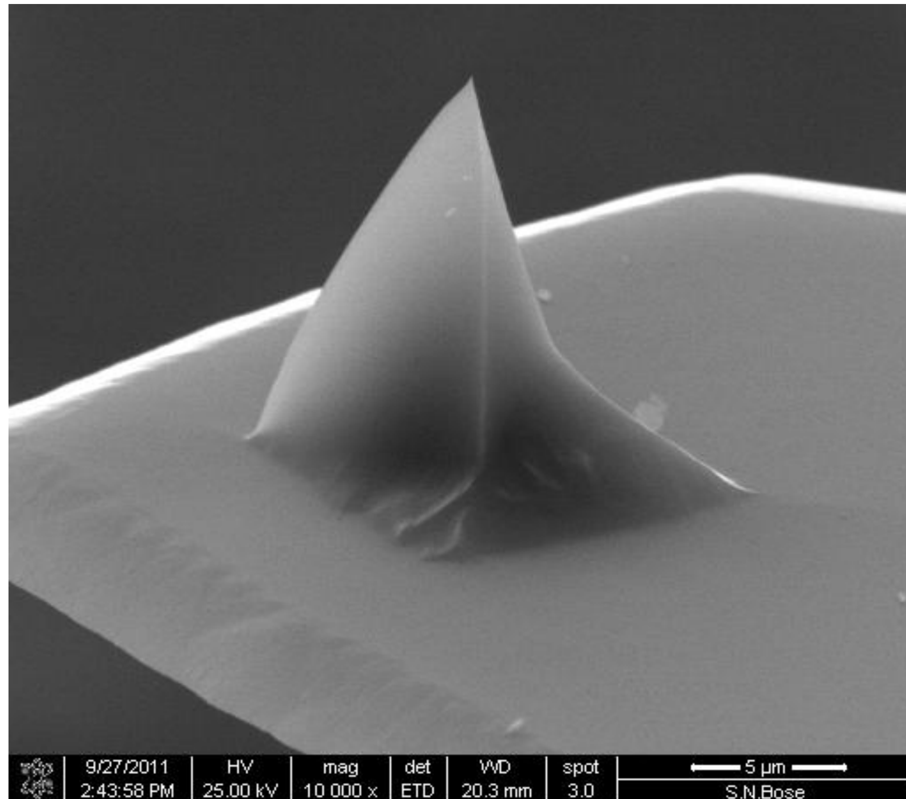

Figure 3.8: An example of SEM image of an AFM cantilever tip used for mechanical measurement.

transmit the output signal of their interaction with the specimen, which is collected by several detectors and converted into the visual signal displayed on the cathode ray tube (CRT) or computerised interface display [7-9]. Figure 3.8 shows a typical example of an SEM image of an AFM cantilever tip for mechanical measurements on a nanowire sample. Excluding the concept of backscattering of the electrons, the interactions between the specimen and the electron beam can be classified into two major categories: elastic interactions with the nucleus and inelastic interactions with the nucleus, where in both types the incident electron losses its energy [7]. Incident electrons, that are elastically scattered through an angle of more than 90°, are called backscattered electrons (BSE), which are significantly smaller in number than those discussed above [7-8]. When the incident beam interacts with the sample, it also generates X-Ray, Auger electrons, cathodoluminescence and secondary electrons [7-9] as shown in the Figure 3.9 [7].

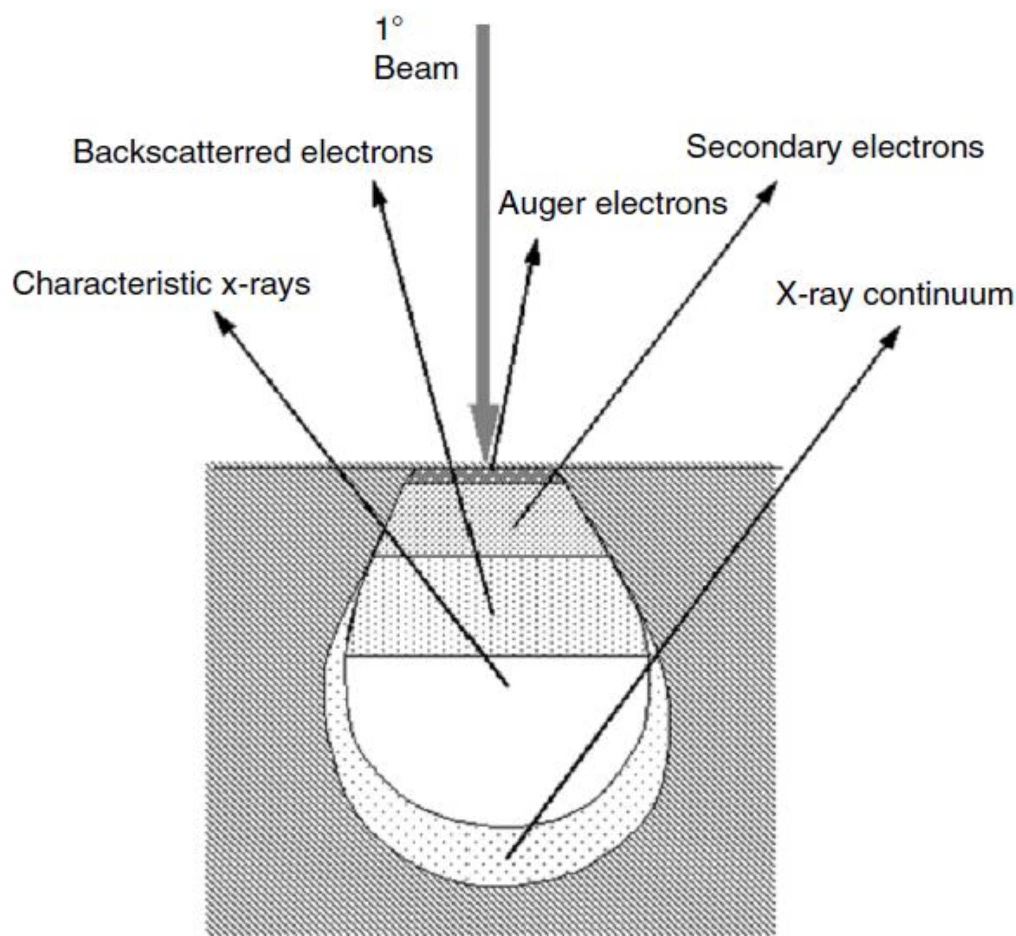

Figure 3.9: An example of incident beam interaction with a sample and several signals generated by the incident electrons in the Scanning Electron Microscope (SEM) and the regions from which the signals can be detected [7].

Imaging of the nanowire experimental samples described in Chapter 4 was carried out using standard conditions with typical beam energy of 10keV instead of standard 30keV (in Chapter 5) to provide better surface sensitivity. Charging of these samples was not an issue. Despite the microcantilever MEMS system being predominantly insulating silicon nitride (Chapter 6) charging was not a problem due to the presence of metal tracks which allowed charge to leak away during imaging.

3.6 Electron Beam Lithography (EBL)

Electron Beam Lithography (EBL) was used in the present work to fabricate nanowires ranging from 10 – 100 nm in diameter in order to compare them with nanowires fabricated by

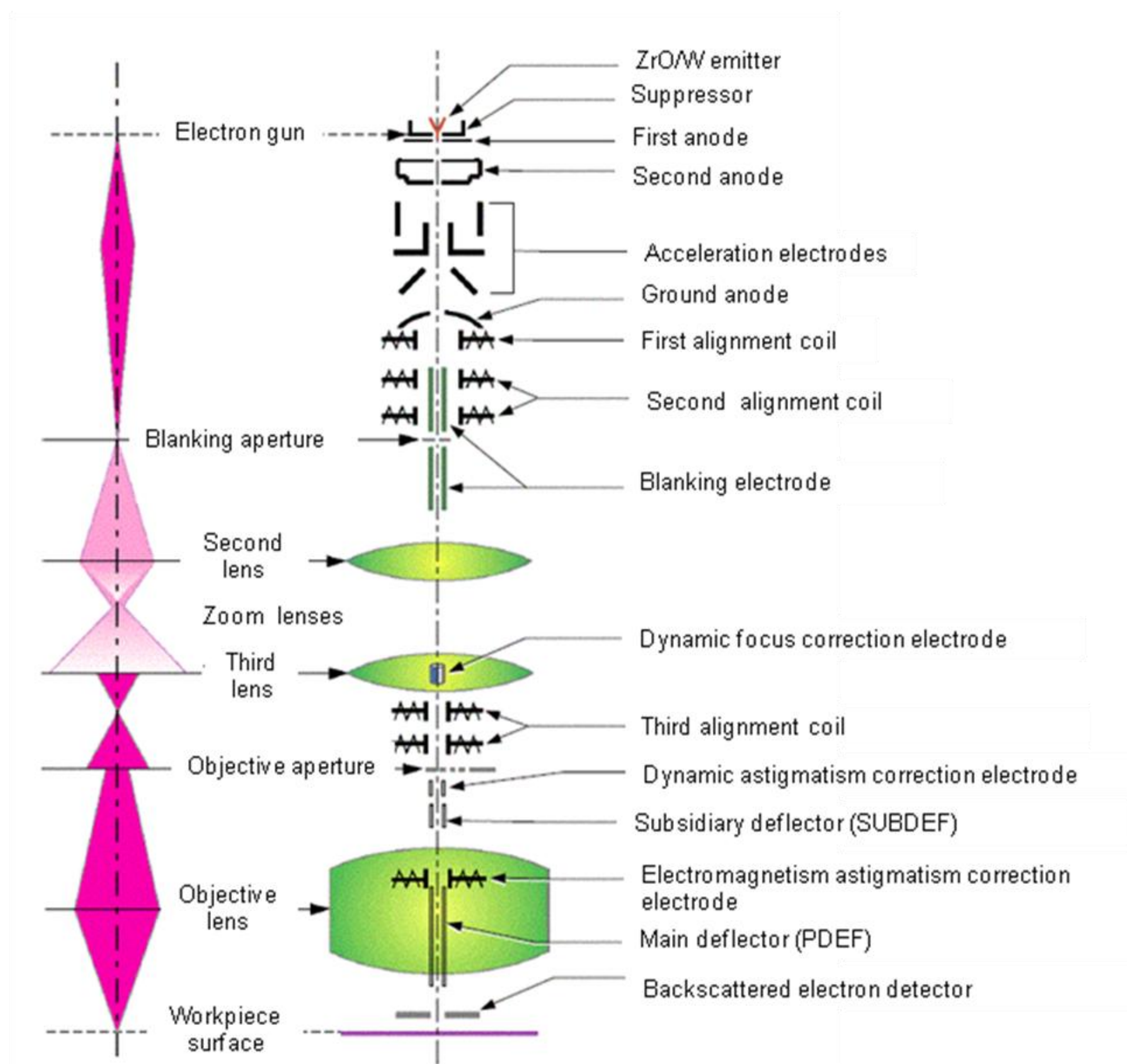

Figure 3.10: Schematic of the Electron Beam Writer [10].

Focused Ion Beam (FIB). A typical SEM system can be used for lithographic fabrication by controlling the XY position of the electron beam and adding a beam blanker [7]. Two resists were used for the present work: S1805 and Poly methyl methacrylate (PMMA). Chapter 3.4.1 describes the nano channels which were fabricated using FIB on S1805 resist in order to electrodeposit the nanowire. However, the process resulted in poor quality nanowires. Subsequently, the PMMA based EBL was used for the fabrication of gold (Au) and chromium (Cr) nanowires at Rutherford Appleton Laboratory, Oxford with the help of Dr Yifan Chen. The EBL fabrication process is very similar to the photoresist spin coating process as described earlier in Chapter 3.2. It involves spin coating of the PMMA at 6000

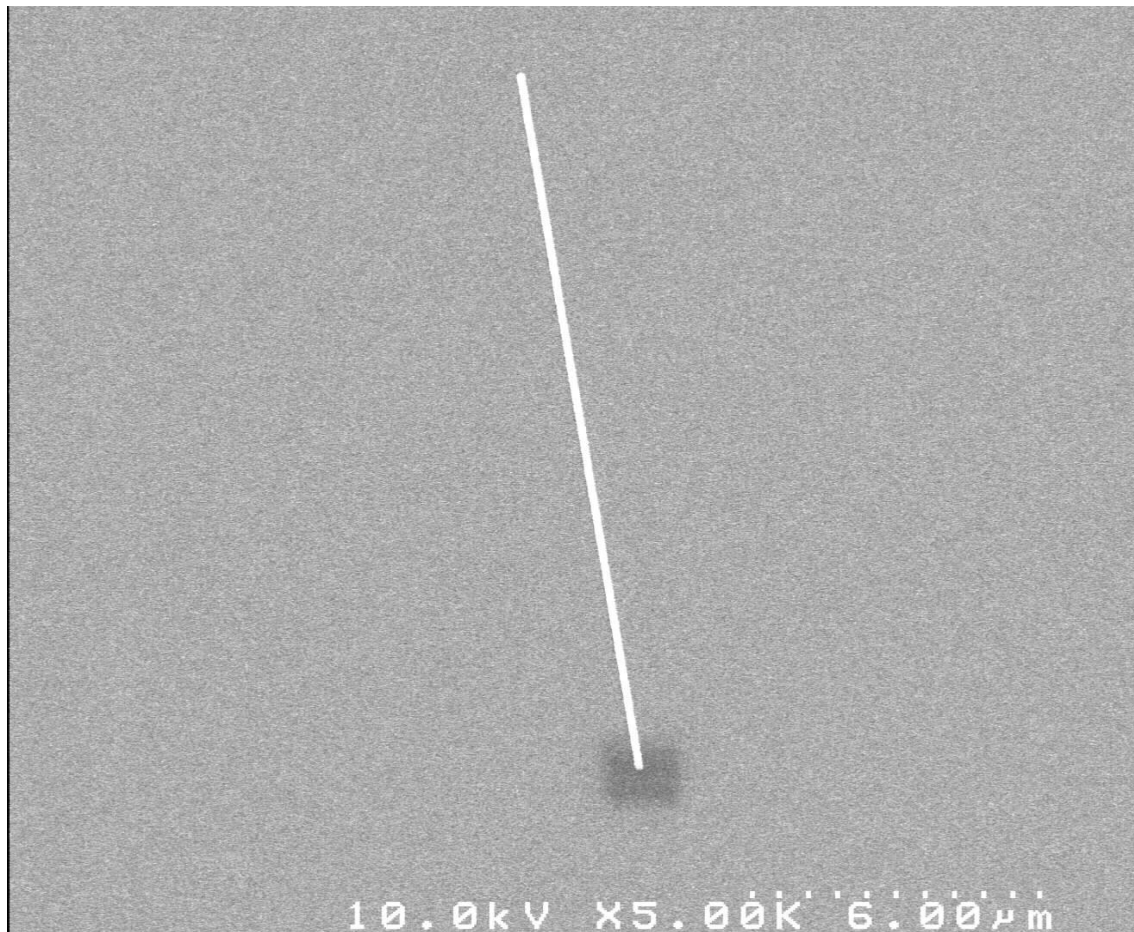

Figure 3.11: SEM image of the gold (Au) nanowire fabricated by Electron Beam Lithography

rpm for 45 seconds, followed by baking of the coated wafer at 150 °C for 30 minutes. After baking, the resist coated samples are exposed at 10 keV in the E-beam writer. Direct pattern writing eliminates the use of a mask during the exposure and provides a higher resolution than optical lithography. Figure 3.10 is a schematic of a typical E-Beam writer. The exposure dose is very significant to the behaviour of the PMMA [11]; at a lower dose electrons break the bond of the polymer atoms giving a positive tone resist, while at very high doses, PMMA atoms solidify and create a stronger bond in negative tone resist behaviour [12]. After the developing process, the fabricated nano channels on the sample are mounted to the thermal evaporation chamber for metal deposition. The lift off process follows metal deposition to remove the residual PMMA using acetone. This leaves the metal nanowires on the substrate. Optical lithography has a resolution limit of typically 200 nm due to its wavelength

diffraction effects [7]. The EBL process has significant advantages over photolithography due to the capability of E-beam to produce structures of less than 10 nm line-width using field emission electron source. Figure 3.11 shows a nanowire of 50 nm width fabricated by us at Rutherford Appleton Laboratory, Oxford.

3.7 Energy Dispersive X-Ray Spectroscopy (EDX)

Energy Dispersive X-Ray Spectroscopy (EDX) is a characterisation technique to extract information about the elemental composition of a sample by absorbing the X-ray spectrum emitted by the area of interest on the sample surface. The basic phenomenon that every element has a different atomic structure is utilised for the analysis. An element distribution image can be produced by quantitative analysis of intensified X-Ray line; where number of photons in an X-Ray defines its intensity. A beam of highly charged particles, with a spot size of ~ 5 nm, can be focused on the sample for the probe [13-14], which excites the electron in the inner shell of the element and replaces it with the highly charged one resulting in the emission of the X-Ray. Rutherford-Bohr model explains that the electrons orbit around the positive nucleus representing the energy level. Energy level is relatively low at the nucleus compared to the electrons far from nucleus. The low energy electron tends to jump to the outer orbit, when the energy is added. The dispersive spectrometer is used to analyse the elements with different energy levels from which the X-Ray is emitted. The radius R_x (μm) of these X-Rays can be given by Equation 3.1 [13],

$$R_x = 0.04 \frac{V^{1.75}}{\rho} \tag{3.1}$$

where V (kv) is the acceleration voltage and ρ (g/cm^3) is density. If the beam spot diameter is d then the analysis radius R is given by Equation 3.2 [13],

$$R = \sqrt{R_x^2 + d^2} \tag{3.2}$$

Figure 3.12 shows an example of Energy Dispersive X-Ray Spectroscopy (EDX) carried out on the gold (Au) nanowires fabricated by Focused Ion Beam (FIB) on a silicon nitride (Si_3N_4) membrane.

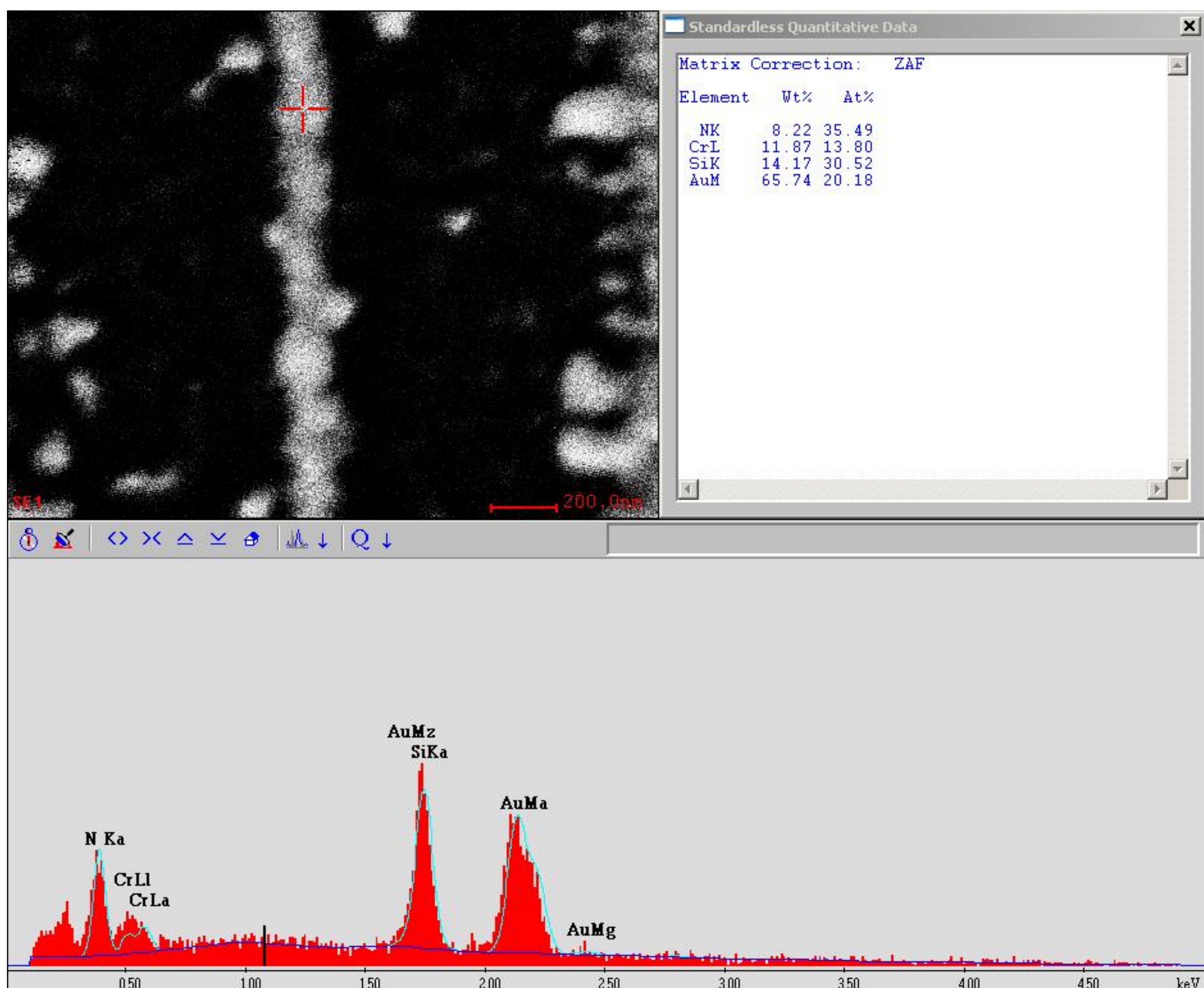

Figure 3.12: Energy Dispersive X-Ray Spectroscopy (EDX) carried out on the gold (Au) nanowire on Si_3N_4 substrate.

3.8 References

[1] Microposit S1800 Series Photo Resist data sheet. Shipley Europe Ltd.

[2] Adnan Malik, Course on *Deep Silicon Plasma Etch*, Rutherford Appleton Laboratory, Oxford (September 2011).

[3] Docker P. T., Kinnell P., Ward M. C. L., *A dry single-step process for the manufacture of released MEMS structures*, J. Micromech. Microeng., 2003, **13**: p 790–794.

[4] Tan Y., Zhou R., Zhang H., Lu G., Li Z., *Modeling and Simulation of LAG Effect in Deep Reactive Ion Etching Process*, J. Micromech. Microeng., 2006, 16: p 2570–2575.

[5] Professor N Cheung, EE143 Lecture 15-16, EE143 F2010, University of California, Berkeley (2010).

[6] Prewett P. D., Mair G. L. R., *Focused ion beams from Liquid metal ion source,* Research Studies Press, John Wiley & Sons Inc., 1991.

[7] Zhou W., Wang Z. L., *Scanning Microscopy for Nanotechnology*, (Springer 2006).

[8] Reimer L, *Scanning Electron Microscopy: Physics of Image Formation and Microanalysis*, (Springer 1998).

[9] Birdi K. S., *Scanning Probe Microscopes: Applications in Science and Technology*, (CRC Press, LLC 2003).

[10] Devin K. Brown, Presentation on *Electron Beam Lithography: Focus & Height* (2008).

[11] Duan H., Zhao J., Zhang Y., Xie E., Han L., *Preparing patterned carbonaceous nanostructures directly by overexposure of PMMA using electron-beam lithography*, Nanotechnology, 2009, **20**: p 135306.

[12] Gautsch S., Studer M., de Rooij N. F., *Complex nanostructures in PMMA made by a single process step using e-beam lithography*, Microelectronic Engineering, 2010, **87**: p 1139-1142.

[13] Franssila S., *Introduction to Microfabrication*, John Wiley & Sons (2004).

[14] Goldstein J., *Scanning Electron Microscopy and X-Ray Microanalysis*, Springer London Limited (2003).

Chapter 4

Study of Instabilities in Nanowires Fabricated by Focused Ion Beam Lithography

4.1 Introduction

Focused Ion Beam (FIB) technology has become an indispensable enabling tool for micro and nano fabrications. One important application is to use FIB for patterning conducting nanowires of metals down to a few tens of nanometre for applications such as interconnects, heaters and temperature nanosensors. A series of experiments on Au nanowires fabricated by FIB on Si_3N_4 membrane show those nanowires with width ≤ 50 nm can have structural instabilities. These are liquid-like and first show-up as undulations in nanowire width with clearly defined wave lengths. For smaller widths (~ 20 nm) the instabilities grow and the wires eventually break-up into spherical balls. Further experiments show that the nanowires can be made stable to smaller widths by the use of a Cr underlayer to enhance surface wetting. In order to use the metallic nanowires in nano-device applications such as interconnects they must be stable and of controlled geometry. It has previously been observed that nanowires with small lateral dimensions may show instabilities which can eventually lead to break up into small spheres [1-2]. Even nanowires formed so as to be embedded in templates show oscillations/fluctuations in diameters leading to corresponding fluctuations in resistance [3]. Such structural or morphological instabilities have been attributed to the Rayleigh-Plateau instability [4-6] where surface energy dominates within the system and are

a major potential concern to the nanotechnology community. Experiments presented in this chapter are typical of approximately 10 similar results.

4.2 Rayleigh – Plateau Instability, Surface Energy and Critical Radius (R_c)

In 1873 Joseph Plateau explained experimentally that the fluid column will break up into spherical droplets when the wavelength is approximately three times greater than the diameter [5]. In 1878 Lord Rayleigh considered instabilities in a liquid cylinder due to surface tension and explained the modulation of its free surface in the form of spatial oscillations having wavelength larger than the circumference of the cylinder [4].

Rayleigh – Plateau instability also occurs in solid materials when the radius (R) falls below the value of $\frac{\sigma_s}{\sigma_y}$ where σ_s Nm^{-2} is the surface stress and σ_y Nm^{-2} is the liquid yield stress. The critical radius $R_C = \frac{T}{\sigma_y}$, where T Nm^{-1} is the surface tension (explained in Chapter 2.5.2). Below this critical radius ($R < R_C$), the surface stress is larger than the yield stress and the instability can grow and lead ultimately to fragmentation. In solids the yield force is many orders larger than that of liquids and as a result the phenomena so ubiquitous in liquids cannot be seen in metals until the lateral dimension falls below a few tens of nanometre. For Au, the material investigated in this chapter, $\sigma_y \approx 100$ MPa and $T \approx 1.3$ Nm^{-1}, so that $R_C \approx 13$ nm. For Cu, with higher yield force $\sigma_y \approx 201$ MPa, R_C has the significantly lower value of 7 nm [7]. It is thus expected that for metal nanowires with lateral dimensions below a few tens of nanometres such instabilities may occur. It is also clear that a number of factors like the degree of wetting of the substrate surface by the nanowires, impurities, strain and temperature may either enhance or inhibit the instabilities.

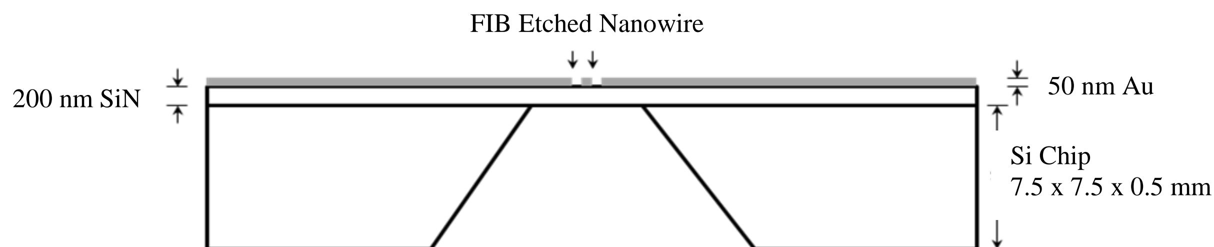

Figure 4.1: Cross-section of the Si_3N_4 membrane with FIB etched nanowire.

Past studies of liquid-like instabilities in metal nanowires have been mostly carried out in cylindrical geometry [1-3] and the wires were not supported. These wires were typically made by chemical routes such as electrochemical deposition and were mostly single crystalline. The motivation of this chapter is to investigate liquid-like instabilities in nanowires with non-cylindrical cross section, made by "top-down" fabrication such as patterning by Focused Ion Beam (FIB). Such nanowires are more likely to be actually used in nano-device applications. In our case, the FIB patterned Au nanowires were formed on Si_3N_4 membranes which are widely used to make nanosensors of various kinds.

4.3 Fabrication of Nanowires on Si_3N_4 Substrate

The typical substrate used in our experiments is a 7.5 x 7.5 mm^2 silicon chip with an etched square window of 200 µm x 200 µm. There is a silicon nitride (Si_3N_4) membrane, of a thickness of 200 nm, covering the entire chip, as shown in Figure 4.1. The nitride window was first coated with a layer of sputtered gold to a thickness of 50 nm (described in Section 3.4.2). The nanowires were fabricated by patterning with FIB using a FEI Strata™ Dual Beam 235 machine with built-in Scanning Electron Microscope (SEM). The focused ion beam of 30 keV gallium (Ga+) ions with spot size of 10 – 15 nm was used to sputter the gold film from two sides to form a 5 µm long nanowire supported on the membrane. Nanowire widths ranged from more than 200 nm down to 20 nm with rectangular cross section. The dual beam capability of the FEI Strata™ Dual Beam 235 FIB/SEM allows in-situ imaging of

the nanowires by SEM immediately after fabrication, without removing them from the specimen work chamber.

The patterning by FIB also leads to implantation of Ga^+ into the body of the Au film. The penetration depth of Ga^+ at this energy in Au is in the range of ~ 10 nm so that the ions stop inside the body of the film. However, the contamination by Ga^+ as detected by Energy Dispersive X-ray Analysis (EDX) attached to the SEM is small, at less than 2%.

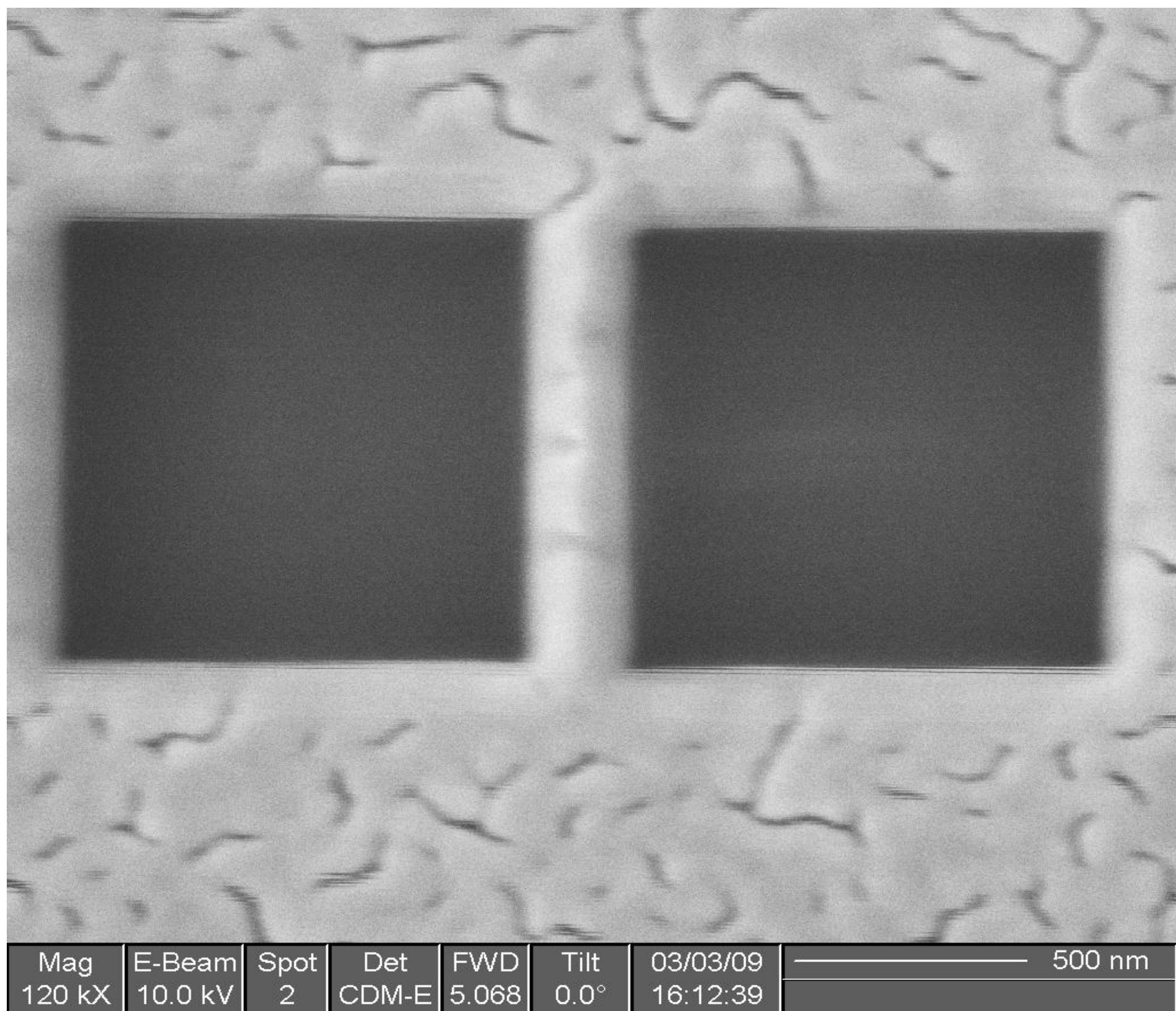

Figure 4.2: SEM image of the 200 nm gold wire without size dependent variations in width.

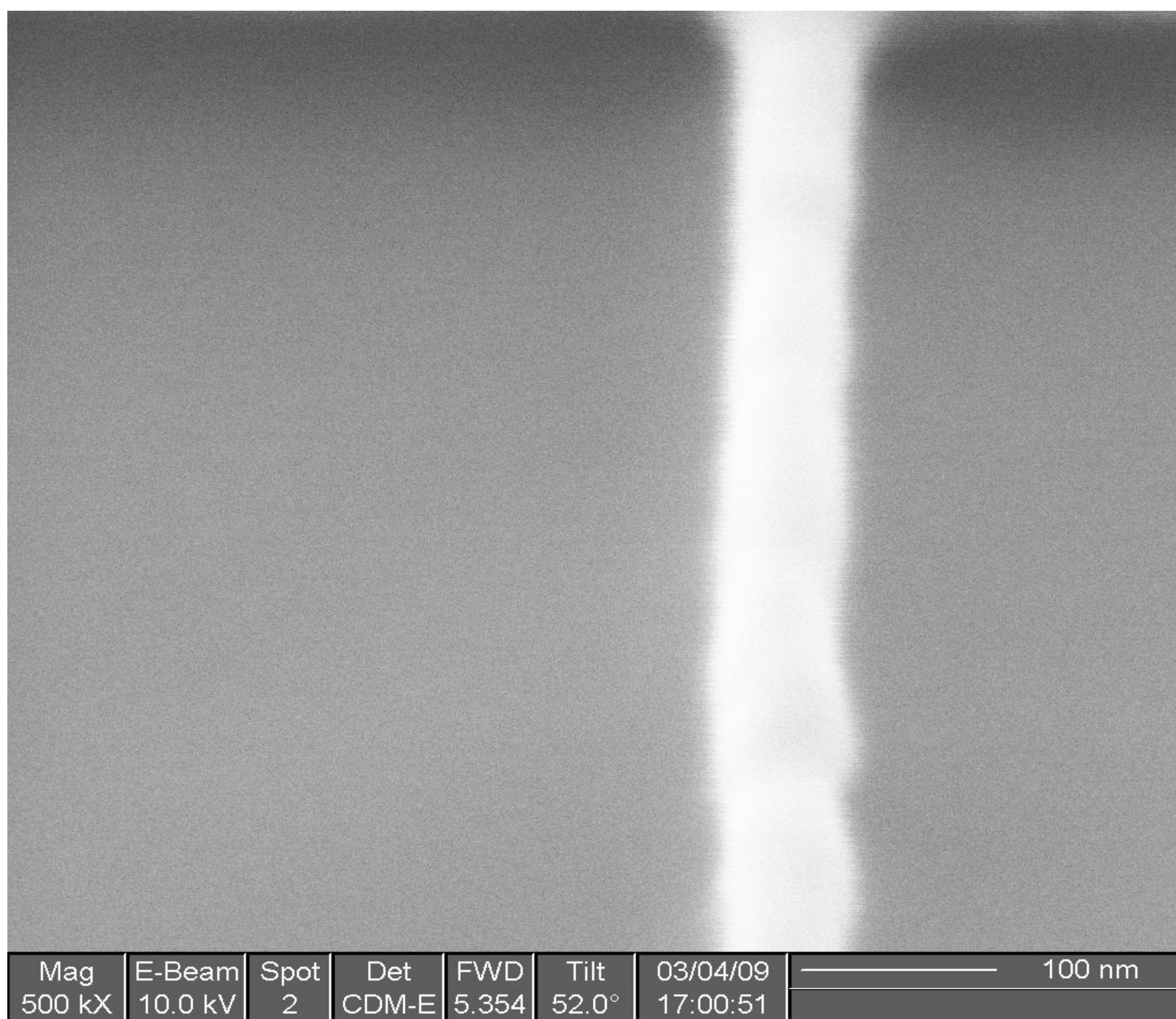

Figure 4.3: SEM image showing 60 nm wire with the appearance of the diameter variation.

4.4 Hydrodynamic Instabilities

Figure 4.2 shows the SEM image of a gold nanowire of width ~ 200 nm. The image clearly shows that the wire is unperturbed and retains its as-fabricated rectangular cross-section along its length. However, as nanowire width is reduced to about 60 nm, undulations start to appear at some locations along the length of the wire, as shown Figure 4.3. With further width reduction to below 50 nm the morphological instability becomes prominent. In Figure 4.4, a nanowire of width below 50 nm shows clear spatial oscillation of width along the whole length of the wire, with well-defined wavelength along both edges (as identified in Figure 4.5). The average wavelength (λ) calculated from the SEM image is found to be about

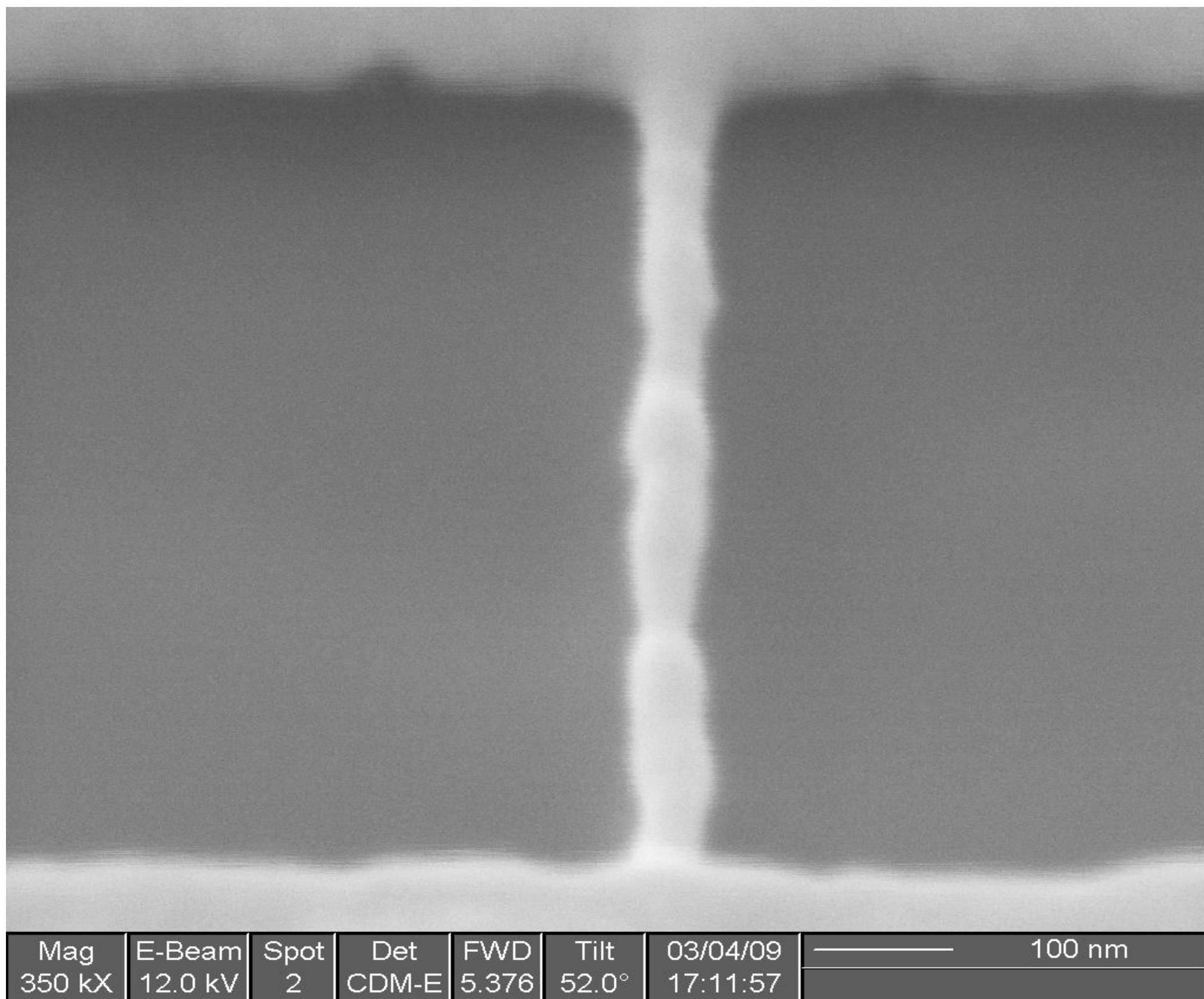

Figure 4.4: SEM image of a nanowire below 50 nm in diameter with periodic variation of the width.

165 nm measured from the SEM images in Figure 4.5. The undulation instability grows progressively as the width is further reduced (diameter ≤ 20 nm) and this leads ultimately to fragmentation of the wire (see Figures 4.5 and 4.6). The developing morphological instability of the nanowire breaks it like a liquid and the fragmented parts make near-spherical balls.

The main results from our experiments are that, for FIB fabricated nanowires of thickness 50 nm and width below ~ 50 nm, morphological instabilities become apparent in the nanowires even though they are supported by the silicon nitride substrate. The observed instabilities in the nanowires of rectangular cross-section are very similar to the liquid-like instabilities observed in free standing nanowires of cylindrical cross-section of similar lateral dimension

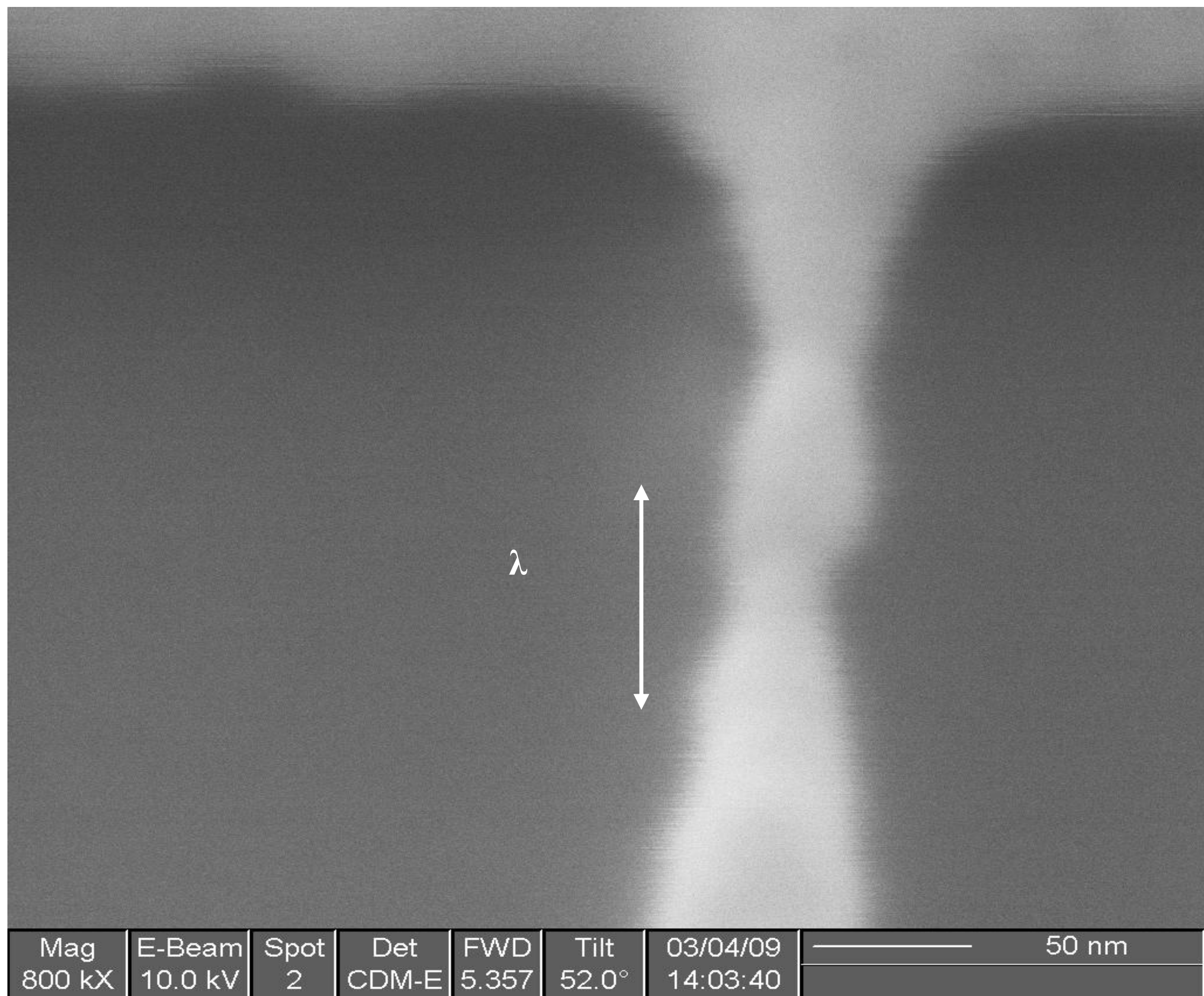

Figure 4.5: SEM image of the beginning of the formation of the droplet in the instable nanowire.

(diameter ~ width). The instabilities appear to have been initiated in absence of any explicit thermal treatment and as discussed below may be triggered by the ion beam process itself.

4.5 Analysis and Characterisation of the Instabilities

The fact that the instabilities occur below a width of 50 nm and the nature of the undulation suggest that these are caused by the Rayleigh–Plateau instabilities. For a pristine Au nanowire with cylindrical geometry, such instability should start when the diameter falls below 25 nm [3-7]. The observed undulations in the width which we take as the onset of the instability, start at a somewhat higher value of the width (~ 50 nm), but the break-up and fragmentation occurs for a width of ≈ 20 nm which is very close to what one would expect for a cylindrical wire.

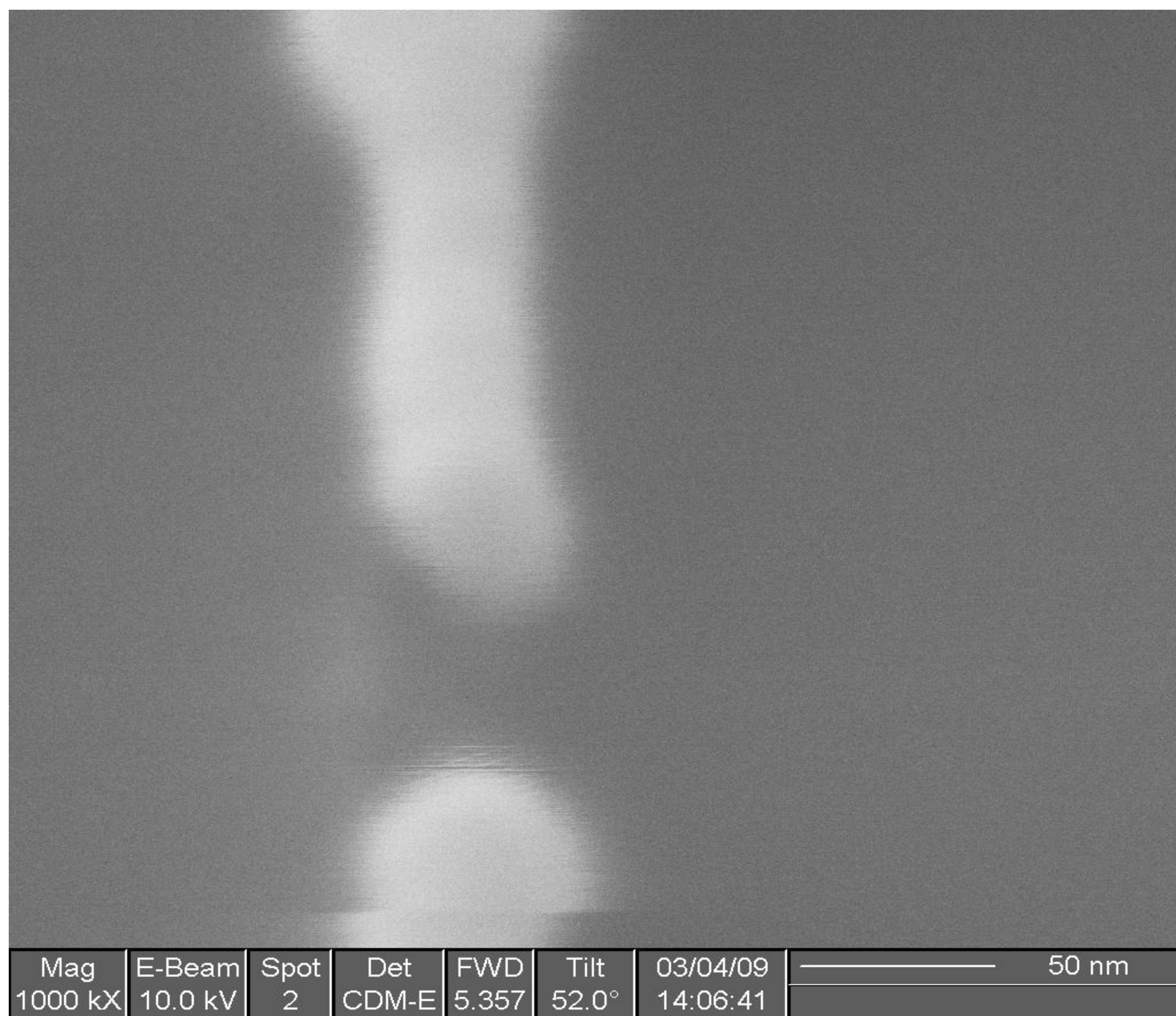

Figure 4.6: SEM image showing a discontinuous nanowire.

In Rayleigh-Plateau instability the wavelength for undulation in the diameter is linked to mass diffusion which sustains the instability. According to accepted models, the hydrodynamic instability gives rise to a spectrum of modes with different wavelengths. There is a wavelength which grows fastest at the instability [6-8] which for a cylindrical wire (with isotropic surface energy) with radius R occurs for $\lambda_m \approx \sqrt{2}(2\pi R)$. The value of λ_m is dependent on a number of factors, including the mode of diffusion and isotropy/anisotropy of the surface energy. The observed undulation is thus expected to have a wavelength close to λ_m theoretically. In our case onset occurs at a width of ≈ 50 nm. This corresponds to an effective radius $R_{eff} \approx \frac{circumference}{2\pi}$, so that for a wire of width of 50 nm and thickness of 50

nm, $R_{eff} \approx$ 32 nm and the expected $\lambda_m \approx$ 282 nm. The final fragmentation occurred at a width of ≈ 20 nm, $R_{eff} \approx$ 22 nm, and we would expect $\lambda_m \approx$ 198 nm. The observed average wavelength of ~ 165 nm, though smaller, is close to the expected range of values. It is therefore proposed that the observed instabilities are due to the Rayleigh-Plateau instability phenomenon.

Since it involves mass transport, the Rayleigh-Plateau instability is often assisted by thermal processes which enhance the rate of mass diffusion [9-10]. These may include defects which can lower the activation energy and strains, which can enhance mass migration and thus trigger the instability. Often instabilities in somewhat wider metal lines made by E-beam evaporation can be triggered by exposing them to ion beams leading to dewetting [11]. In our case, however, it is not clear what leads to the initiation of the instability; although ion-bombardment induced dewetting at the edges of the nanowire is a possible cause which should be investigated further including the energy input during the SEM characterisation.

To check the role of dewetting, an additional experiment was conducted using a 4 nm Cr adhesion layer on Si_3N_4 membrane surface before the Au film was deposited by thermal evaporation at a pressure of 2 x 10^{-6} Torr. The film was then exposed to the same schedule of patterning using FIB. In this case, the instability was inhibited and the film began to fragment only when its width was below 15 nm compared with 10 nm or 8 nm in the case of passivated low doped silicon or un-passivated highly doped silicon substrate (as discussed in Chapter 5). It is also reasonable to conclude that enhanced adhesion of the film of Cr layer inhibited the ion induced dewetting and delayed the onset of the Rayleigh – Plateau instability. The use of an adhesion layer to produce FIB-patterned nanowires with significantly reduced width is encouraging and allows fabrication of stable ultra-narrow nanowires for a range of applications.

4.6 Conclusion

An experimental investigation of the morphological stability of Au nanowires patterned using FIB on a silicon nitride membrane substrate has been completed. Below a certain width (~ 40 – 50 nm) the nanowires develop liquid-like instabilities. The observed behavior has been explained as a manifestation of the Rayleigh – Plateau instability which occurs below a critical width when the surface energy dominates. It has been found that use of an adhesion layer of Cr inhibits the onset of the instability and shows potential for stable ultra-narrow FIB-etched nanowires for nanosensors and other applications. Further work reported in the next chapter investigates, amongst other things, the effects of different substrates and doping elements on nanowire stability.

4.7 References

[1] Sun Y., Mayers B., Xia Y., *Transformation of silver nanospheres into nanobelts and triangular nanoplates through a thermal process.* Nano Letters, 2003, **3**(5): p 675–679

[2] Toimil-Molares M. E., Balogh A. G., Cornelius T. W., Neumann R. Trautmann C., *Fragmentation of nanowires driven by Rayleigh instability*, Appl. Phys. Lett., 2004, **85**: p 5337.

[3] Bid A., Bora A., Raychaudhuri A. K., *Low frequency conductance fluctuations (1/f_ noise) in 15nm Ag nanowires-Implication on its stability*, Phys. Rev B, 2005, **72**: p 113415.

[4] Lord Rayleigh, Proc. London Math. Soc., 1878, **10**: p 4.

[5] J Plateau, *Transl. Annual Reports of the Smithsonian Institution*, 1873, p 1863.

[6] S. Chandrasekhar, *Hydrodynamic and Hydromagnetic Stability*, Dover press, New York, 1981, p 515–574.

[7] Zhang C.H., Kassubek, F. Staford C.A., Surface Fluctuations and the Stability of Metal Nanowires, Phys. Rev B, 2003, **68**: p 165414.

[8] Nichols F. A., Mullins W. W., *Surface (Interface) and Volume Diffusion Contributions to Morphological Changes Driven by Capillarity.* Trans. Metal. Soc. AIME, 1965**, 233**: p 1840.

[9] Powers J. D., Glaeser A. M., *High-Temperature Healing of Cracklike Flaws in. Titanium Ion-Implanted Sapphire*, J. Am. Ceram. Soc., 1993, **76**: p 2225-2234.

[10] Karim S., Toimil-Molares M. E., Balogh A. G., Ensinger W., Cornelius T. W., Khan E. U., Neumann R., *Morphological evolution of Au nanowires controlled by Rayleigh instability*, Nanotechnology, 2006, **17**: p 5954-5959.

[11] Zhao K., Averback R. S., Cahill D. G., *Patterning of metal nanowires by directed ion-induced dewetting*, Appl. Phys. Letts, 2006, **89**: p 053103.

Chapter 5

Effects of Substrate on the Instabilities in Nanowires Fabricated by Focused Ion Beam

5.1 Introduction

Owing to considerable interest for a range of applications in nanotechnology including interconnects in NEMS devices, experimental gold nanowires were produced using the FIB etch process on a variety of substrates and were found to demonstrate liquid-like structural instabilities, the occurrence of which depends upon the type of substrate and the presence of an adhesion layer. Chapter 4 demonstrates the existence of these instabilities. Most importantly, the instabilities depend upon the lateral dimension of the nanowires which typically onset below approximately 50 nm nanowire width. The instabilities can ultimately lead to break-up of the nanowires into islands of metal and are clearly of the Rayleigh-Plateau type. In this chapter we have demonstrated that on insulating substrates there is evidence of electrohydrodynamically formed Taylor Cones. The liquid-like behaviour is most likely to be the consequence of the low dimensions of the nanowires. Nano-scale structures and their use in nano-electronics, including single charge electronics, molecular electronics [1] and quantum computing have been reported previously [2]. Metallic nanowires must have well defined stable geometries for these applications, i.e. interconnects, sensors & actuators. NEMS devices are most frequently made using silicon micro-fabrication technology so it is important to study the fabrication of conducting nanowires on different types of silicon substrates (i.e. SiO_2/Si, Si_3N_4/Si etc) to develop robust methods for producing them under varying surface conditions. Recently published work has suggested that sub 10 nm structures

suffer serious line roughness problems which render devices with these dimensions "intrinsically unmanufacturable" [3]. Focused ion beam machining has emerged as an important tool for experimental fabrication and rapid prototyping of nanoscale devices. The purpose of the work reported here is to study the results of using FIB as a lithography tool to produce gold nanowires, on technically important surfaces such as silicon, with and without an oxide layer, and on silicon nitride surfaces. This work also studies the limits of the structural integrity of these nanowires as a function of their width and substrate surface conditions.

It has previously been observed that nanowires with small lateral dimensions may show instabilities which lead to their break-up into small spheres [4-5]. Even nanowires constrained by templates show fluctuations in diameter leading to corresponding variations in local resistance [4]. In displaying these structural or morphological instabilities, nanowires display properties which are more like those of a liquid than a genuine solid. These variations in morphology have therefore been attributed to the Rayleigh-Plateau instability [4-7] and are of significant potential concern to the nanotechnology community. Initial experiments to form gold on silicon nanowires by Focused Ion Beam etching have also revealed these effects [8] and have stimulated the more detailed study reported here. The new work bears comparison with that of Tuboltsev and Raisanen [9] who studied the use of low energy ion beams to produce Au nanowires of <10 nm diameter by "downsizing" larger nanowires through ion beam sputtering. They found that Ar+ irradiation at 200 eV beam energy produced stable nanowires by sputter "downsizing" of 60 nm wide, 50 μm long wires on a silicon wafer. Strongly contrasting results were obtained using a 500 eV beam of Ga+ ions focused to a spot of diameter 11 μm. The gallium content of the downsized structure was found to have a destructive effect, causing the ensuing nanowire to break-up into a collection of islands. This was explained in terms of the interaction between the Au deposit

and nanocondensates of gallium in the form of liquid droplets. That this occurs at room temperature was explained by the fact that gallium nanoparticles have lower melting point than bulk gallium [10]. Our work reported here takes a different approach in which a finely focused beam of much higher energy (30 keV) is used to form nanowires by etching a pair of rectangles on either side of the nanowire. The ion spot employed is much smaller (< 30 nm) than that used by Tuboltsev and Raisanen. Though this spot diameter is of the same order as the width of the nanowires studied in the present work (see below), the dose of gallium ions received by the bulk of the nanowire is far lower than in the work of Tuboltsev and Raisanen (who deliberately irradiated the wire) and is concentrated at the edges of the structure instead of across its entire width as in their case. The destructive effect of the gallium nanocondensates observed by Tuboltsev and Raisanen is thereby significantly lower in our case and the instabilities observed are rather different. The nanowire instabilities we observe closely resemble classic liquid instabilities and suggest that Au nanowires with diameters of a few tens of nanometres are liquid-like. Experimental results presented in this chapter are typical of approximately 20 similar results.

5.2 Liquid-like Instabilities

In this chapter the liquid-like instabilities are considered using slightly different theoretical and experimental approach to that in Chapter 4. This chapter investigates the effects of different substrates and doping elements on nanowire stability. The driving force for this surface modulation is derived from the decrease of the surface area and thus the total surface energy when the spatial oscillation is present, thus making the modulation energetically favourable. Rayleigh's work also explained the break-up of liquid jets into droplets [7]. Sir G I Taylor [11] considered electrically driven liquid jets for which the Maxwell electric surface stress provides additional effects, including the formation of Taylor Cones, while Nichols and

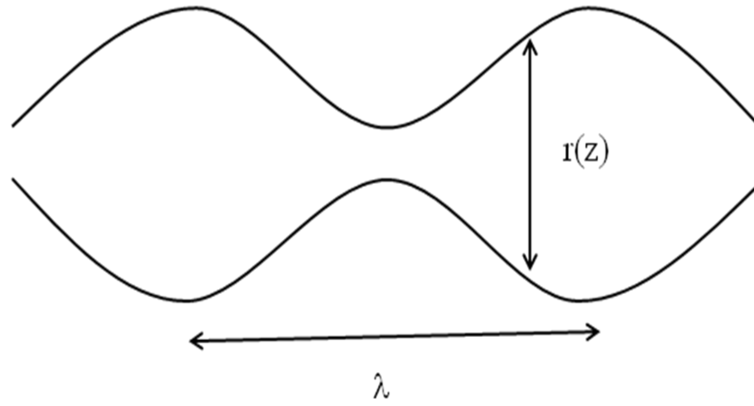

Figure 5.1: Schematic showing the radial perturbation of a nanowire due to Rayleigh instability.

Mullins extended Rayleigh's perturbation approach to solids [4]. Taylor's contribution is of particular relevance to the case of FIB etched nanowires since, depending on substrate conductivity, the nanowires may charge up under the ion beam during fabrication, giving rise to a significant electric stress. It is also interesting to note evidence for lowering of the melting point with size in gold nanoparticles dating back to the early work of Takagi [12], and it is reasonable to assume that this will also be the case for FIB etched nanowires.

The basic situation is illustrated in Figure 5.1 which shows a cylindrical wire treated as a liquid column with a sinusoidal perturbation distributed along its length. The wire has a volume-conserving fluctuation with wave vector $k = \frac{2\pi}{\lambda}$ in the *z* direction. The radius of the wire at a distance *z* along its axis is given by Equation 5.1 [13],

$$r(z) = r_0 + b\sin\left(\frac{2\pi}{\lambda}\right)z \tag{5.1}$$

where r_0 is the radius of the unperturbed wire, *b* is the perturbation amplitude and λ is the wavelength of perturbation. The maximum stress that the wire can sustain before the onset of plastic flow is σ_y, the yield strength. The surface stress in a thin wire is $\sigma_s = \frac{T}{r_o}$ where *T* is the surface tension and if $\sigma_s > \sigma_y$ the wire will undergo plastic flow [14-16]. If the

perturbation wavelength is greater than the circumference of the wire, i.e. if $\lambda > 2\pi r_0$, the wire will break-up under this surface tension stress, as in the case of the Rayleigh instability of a column of liquid [7-8, 14-17]. This rough model suggests that the surface tension should drive a crossover from crystalline solid behaviour to plastic or fluid behaviour below a minimum radius of solidity, $r_{\min} = \frac{T}{\sigma_y}$. For Au, $\sigma_y \approx 100$ MPa and $T \approx 1.3$ N/m, giving $r_{min} \approx$ 13 nm. This analysis implies that for metal nanowires with lateral dimension of a few tens of nanometres liquid instabilities should occur. Structures on this order may appear stable, notwithstanding some line-width roughness due to noise effects in nanofabrication, in particular where high sensitivity resists have been used in electron beam lithography. However, closer inspection can reveal evidence of liquid-like instabilities, as discussed above for the lines shown in Figure 5.1. This liquid-like behaviour is also promoted by the small number of atoms across the diameter of nanowires of these dimensions, which consequently do not possess the long range order typical of a solid, hence increasing the tendency to fluid–like behaviour for the thinnest nanowires. It is a moot point as to whether the instability is sustained by diffusion or by genuine fluid flow, but the presence of defects caused by ion irradiation is expected to reduce the activation energy for diffusion and also promote the growth of the instability. Apart from the width of the wire and charging, additional factors like impurities, strain and temperature can also influence these instabilities. Attempts have been made recently to understand thin nanowire instabilities through theoretical and experimental studies [5, 13]. The break-up of nanowires into chains of nanospheres due to Rayleigh instabilities with increasing annealing temperature has been observed for Cu and Au nanowires on a SiO_2 substrate [18, 19]. Toimil-Molares *et al* [18] have demonstrated that copper nanowires start to fragment during annealing at temperatures of approximately one third of the melting temperature of bulk copper with ultimate decomposition into a chain of

nanospheres at higher temperatures. The Rayleigh instability, assisted by the uniform volume shrinkage created by the reduction of CuO nanowires to metal, is proposed as the mechanism driving the formation of the nanochains in this case [19]. There has been very little previous work on ion beam effects in nanowires, but ion beam irradiation of thin Au and Pt lines has been shown to promote the formation of a linear array of metal dots with spacing consistent with the Rayleigh instability [20-21]. Among the few reported studies involving gold nanowires, Karim *et al* investigated the stability of gold nanowire under annealing [19]. Their work found that instabilities could be introduced within nanowires of diameter in the range of 50 – 100 nm using such a process. Karim [19] states that these instabilities at lower temperatures should be taken into account before fabricating NEMS devices.

It is noteworthy that most of the nanowires studied to date were freestanding nanowires, while surface deposited or templated nanowires are of greater relevance to the requirements of interconnects in nanotechnology, which will in most circumstances be produced by a variety of lithographic methods. These include FIB lithography as a key experimental prototyping tool and this is the motivation of the present work in which we explore the existence of instabilities of the liquid Rayleigh-Taylor type in gold interconnect nanowires fabricated using FIB. The work reported here includes detailed studies of the importance of nanowire dimension, surface charging and substrate type and condition in determining how destructive the instability becomes. In addition to affecting charging of the nanowire, the substrate will also affect its adhesion, thereby mediating plastic flow and break-up under stress.

5.3 Fabrication Process of Nanowires on Different Substrates

Au films, with Cr adhesion layer, were vacuum deposited on three different silicon substrates to study the effects of substrate surface conditions on stability of the nanowires. For all

substrates, a thin Cr adhesion layer ~ 4 nm thick was first deposited by evaporation, followed by a 50 nm thick layer of Au from which the nanowires were formed using FIB etching. The deposition was performed at a pressure of 2 x 10^{-6} Torr and the thickness of the films were controlled using a quartz crystal oscillator thickness monitor.

The substrates used in these experiments were (i) Si (100) with two different conductivities (ii) 300 nm SiO_2 on Si (100) and (iii) 200 nm thick Si_3N_4 on Si (100). Space charge build up during ion etching may affect the stability of the nanowires, so in order to explore this effect, both lightly doped p-type Si and heavily doped p-type Si were used alongside the oxide coated wafer substrate. To investigate the effect of surface passivation of the substrates on resistance to flow and hence the mechanical strength of the nanowires, experiments were conducted using Si treated with buffered HF for both heavily and lightly doped substrates.

The nanowires were fabricated by etching out the gold film from both sides by gallium (Ga+) ions using an FEI Helios 600 Dual Beam system with a beam current ~ 30 pA at energy of 30 keV. The nanowires produced have rectangular cross-section with widths ranging from more than 200 nm down to 10 nm; their length in each case is 2 μm. Scanning Electron Microscopy of the nanowires (using a field emission gun source) was done in situ, immediately following fabrication, together with Energy Dispersive X-Ray Analysis (EDX).

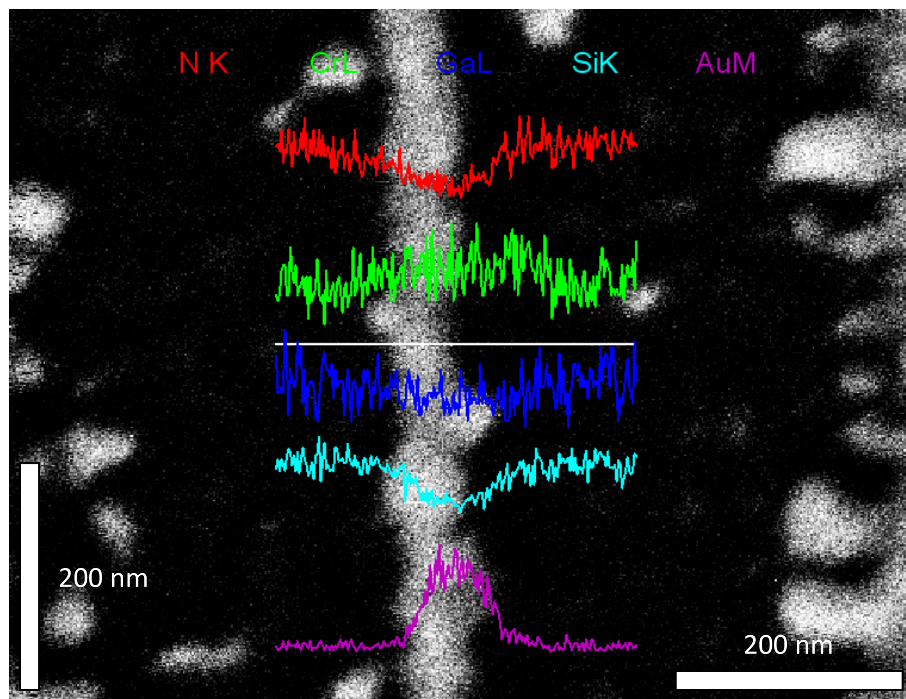

Figure 5.2: EDX analysis results showing atom concentrations across the nanowire

5.4 Critical Radius and Hydrodynamic Instabilities on Different Substrates

A line scan EDX measurement was carried out across the gold wire along the line shown in Figure 5.2 to reveal the distributions of Au, Cr, Si, N and Ga. The N and Si peaks appear from the substrate while Au and Cr are due to the wire and its adhesion layer. As expected, the concentration of Au shows a steep rise in the wire region where there is also a small increase in the concentration of Cr. The Ga contamination is localised at the outer edges of the wire where the effects of the ion beam milling are concentrated, with some limited spread into the nanowire due to the non Gaussian tails on the Focused Ion Beam [22]. It has been suggested that, near the point of impact of the 30 keV gallium ion beam, the temperature may increase locally above the melting point of gold within the beam interaction volume (voxel), the dimensions of which are of the same order as the nanowires. The pixel dwell time during the FIB etch process is 1 μs so that the local heating is transient and largely confined to the

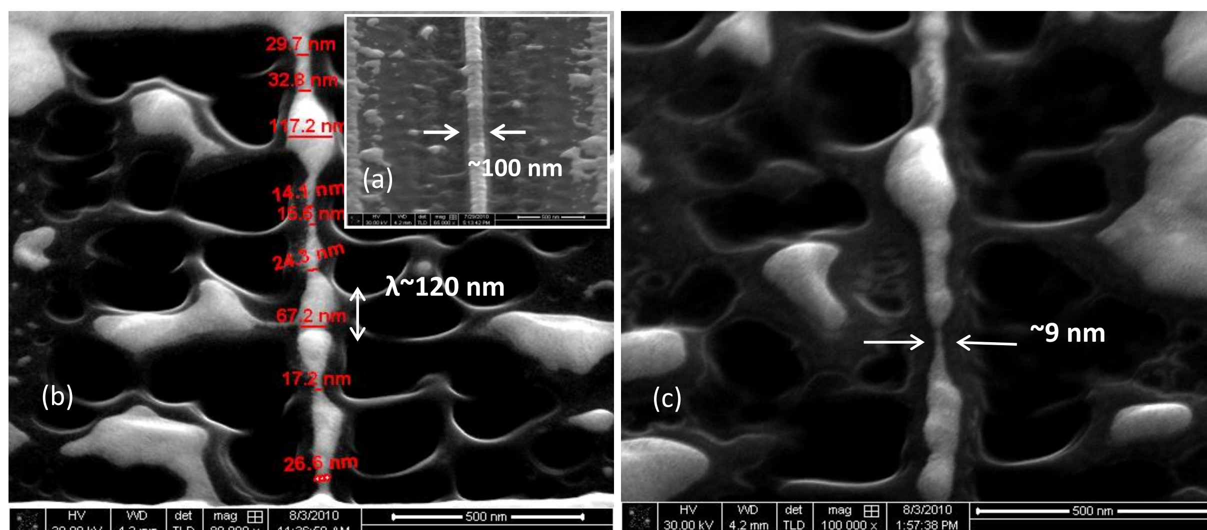

Figure 5.3: SEM image of instability in thin gold nanowire (Sample A) on (a) nearly perfect nanowire with thickness of 100 nm (b) lightly doped Si with native oxide (c) instability seen on unpassivated lightly doped Si.

edges of the nanowire. However, it cannot be totally rejected as a possible contribution to at least some of the liquid-like behaviour observed.

The patterning studies were done on nanowires with starting width of ~ 300 nm. The FIB-fabricated nanowire on lightly doped Si (ρ ~ 5 ohm-cm; no HF treatment) is shown in Figure 5.3; the substrate has a layer of native oxide of thickness 4 nm. Figure 5.3(a) shows a more or less perfect wire of 100 nm width with no significant variation in diameter. However, on further thinning the wire to less than 50 nm, flow is observed, as shown in Figure 5.3(b). This leads to a tendency for the Au to form spheres of more than 100 nm diameter in a number of locations, producing an irregular structure. A nanowire of width ~ 15 nm was then achieved with the formation of more spherical regions due to fluid flow. The wavelength of the modulation λ is around ~ 120 nm. To achieve the lowest possible dimension the Au line width was reduced by adjusted FIB milling. As shown in Figure 5.3 (c) the lowest possible width observed was ~ 9 nm. Figure 5.4 shows the results for a Au wire fabricated on unpassivated and passivated substrate B which has very low resistivity, ρ ~ 0.01 ohm-cm. Passivation can be defined as making the substrate (Si) passive and unaffected by

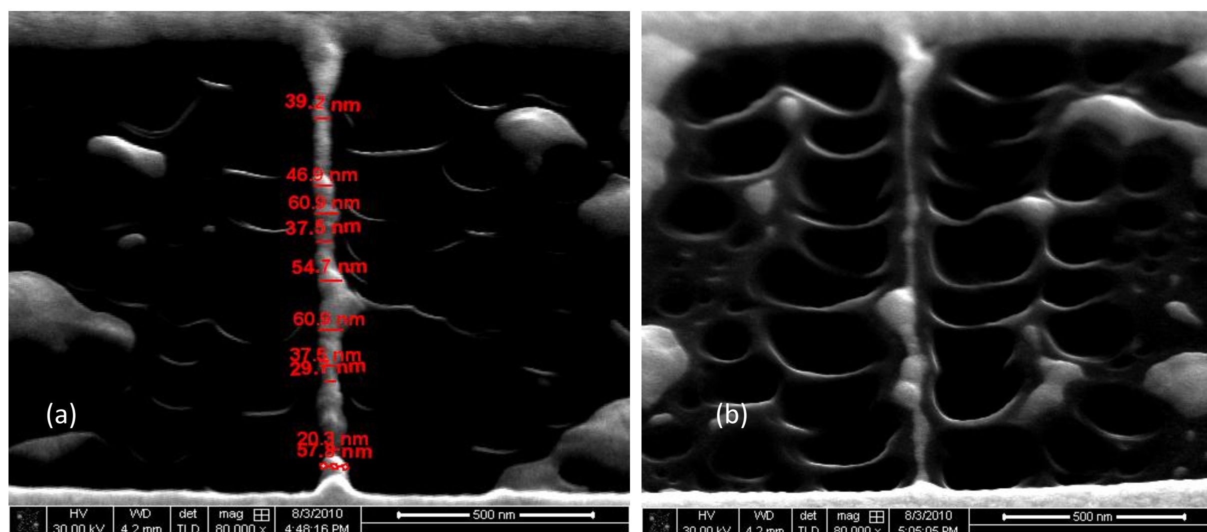

Figure 5.4: (Sample B) (a) Au nanowire ~ 40 nm wide fabricated on unpassivated highly doped Si (b) thin straight nanowire with limited instability fabricated on passivated highly doped Si.

environmental factors. The passivation layer on the wafers used in this work was the native oxide. For some experiments, this was removed using HF treatment leaving a more chemically active substrate surface due to the so called "dangling bonds". Thinner wires can be patterned before break-up, in marked contrast to the previous lightly doped cases. Figure 5.4(a) shows a wire of about 50 nm diameter with a small radial variation. The wavelength of modulation is λ ~ 90 nm. This was then further thinned down to achieve a wire of minimum width of ~ 8 nm, having connected spheres of diameter ~ 30 nm in an extended "peanut" shape. The unpassivated surface leads to a relatively long (~ 1 μm) uniform wire of diameter ~ 10 nm as shown in Figure 5.4(b). Thus, from both samples A and B it is seen that surface passivation leads to higher instability and unpassivated substrate can leads to formation of wires with considerable smaller width.

The results demonstrate a noticeable change in the stability of the wire depending on the resistivity of the Si surface, which can be controlled by doping of the substrates, and on the presence of different native oxide layers, presumably because charging is reduced using highly doped substrates. Removal of the native oxide from the substrate also contributes to improved stability through better adhesion due to silicon dangling bonds.

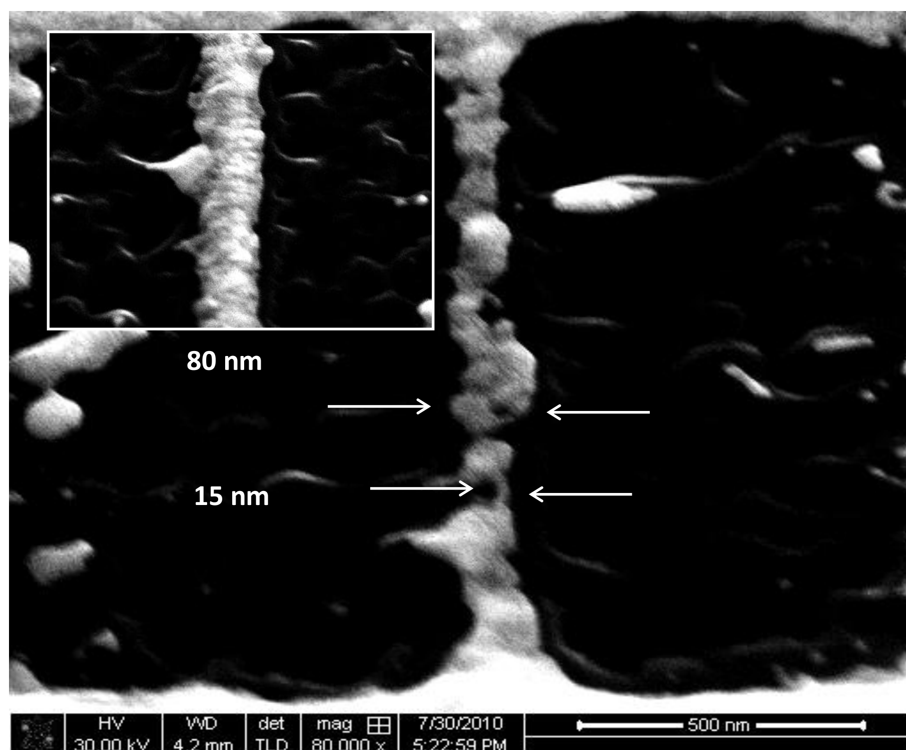

Figure 5.5: SEM image of Au nanowires fabricated on SiO_2 (300 nm)/Si (Sample C) showing more pronounced liquid-like instability. (inset showing evidence of Taylor Cone formation with apex jetting).

In order to investigate further the effects of substrate conductivity and charging effects on the patterned nanowire stability, the experiments were repeated for two further substrates C and D. Figure 5.5 shows the results for the sample C (300 nm SiO_2/Si). The liquid instabilities are apparent even for the wider wires in this case. In addition, for substrates with lower conductivity, the charging due to the FIB process leads to the formation of Taylor Cones [11] on the sides of the nanowire. Figure 5.5 shows several features of approximately conical shape. Some of these may be simple line roughness artefacts of the manufacturing process. Others are thought to be Taylor Cones formed by charging during FIB etch or by charging during SEM examination. For example, the feature shown in the inset has a half angle of approximately 50°, close to the Taylor's theoretical prediction of 49.3°. It also has a jet feature at its apex, which is associated with significant ion emission. It is therefore

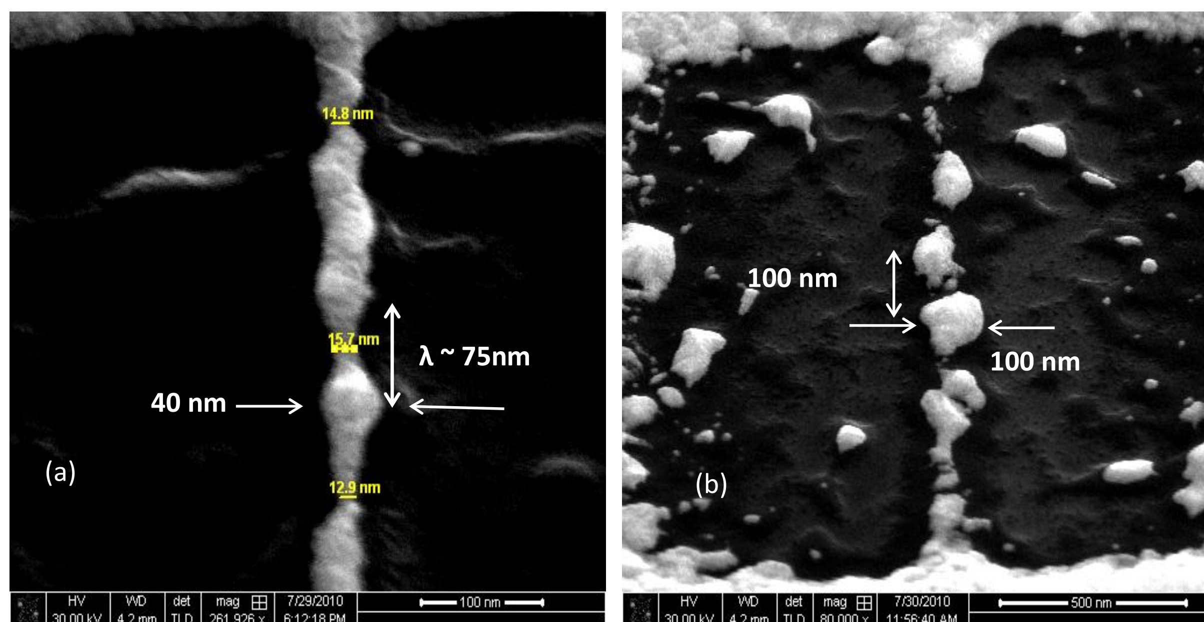

Figure 5.6 (a) Nanowire on Si_3N_4 (200 nm)/Si (Sample D) at the onset of fragmentation. (b) Nanowire fragmented into spheres.

concluded that this is indeed a Taylor cone, either "frozen in" during the FIB manufacturing process or occurring due to charging during acquisition of the SEM image. It is not possible to be sure which without further experiments focused on this phenomenon. The results for sample D (200 nm Si_3N_4/Si substrate) are similar to those for sample C, as seen in Figure 5.6(a). The enhancement of the surface resistivity and inhibition of the charge flow leads to greater distortions in the patterns for samples C and D. In Figure 5.6(a) the instability of the wire becomes more prominent, with thinning to regions in which spherical beads of radius of 40 nm are just connected through regions of ~ 15 nm width. The wavelength derived from the SEM image is found to be λ ~ 75 nm (as marked in Figure 5.6(a)), which is more than the circumference, consistent with Rayleigh's theory [7]. Finally, the liquid-like instability causes the wire to fragment into nanoparticles of size ~ 100 nm diameter spaced by ~ 100 nm shown in Figure 5.6(b). The appearance of instabilities with an associated wavelength is a signature of liquid-like behaviour and this is observed in all cases studied. However the wavelength λ depends on the substrate as well as on details of the surface passivation. A summary of data for the Rayleigh liquid instability extracted from the SEM pictures is given in Table 5.1. The critical diameter for each case is also shown in the table. Here we find the

λ/d value to be less than the expected value of ~ 3 predicted by the Rayleigh – Plateau model of falling liquid. This is almost certainly due to the modification of the nanowire by its interface with the supporting surface where adhesion plays a major role. The critical diameter is found to be in the range of 10 – 20 nm, lowest for highly doped Si and maximum for SiO_2, which have respectively the lowest and highest resistivity of the four different samples studied.

Table 5.1: Properties of the nanowire instability for different substrates (the average data shown are the result of approximately 20 repeated experiments)

Substrate	Resistivity	Average Diameter (d)	Average Wavelength (λ)	λ/d	Smallest diameter obtained
Passivated low doped Si (Sample-A)	5×10^{1} Ω-cm	65 nm	120 nm	1.8	14 nm
Un-passivated low doped Si (Sample-A)	5×10^{1} Ω-cm	50 nm	90 nm	1.8	10 nm
Un-passivated Highly doped Si (Sample-B)	1×10^{-2} Ω-cm	55 nm	90 nm	1.7	8 nm
Passivated Highly doped Si (Sample-B)	1×10^{-2} Ω-cm	55 nm	80 nm	1.5	10 nm
Si_3N_4 (Sample-D)	1×10^{14} Ω-cm	35 nm	75 nm	2.2	13 nm
SiO_2 (Sample-C)	10^{14}-10^{16} Ω-cm	80 nm	140 nm	1.8	15 nm

5.5 Conclusion

The structural and morphological stability of Au nanowires, fabricated by Focused Ion Beam etch of gold films on different substrates, has been investigated experimentally as a function of nanowire width. The results are different from those reported in the literature for free standing nanowires and this is explained in terms of different surface bonding effects. Nevertheless, even in the presence of surface adhesion, there is a clear tendency for liquid-like behaviour with associated electrohydrodynamic instabilities for narrower nanowires on all substrates. The stability of the wires is noticeably better in the case of conducting Si substrates than for silicon coated with the insulators SiO_2 or Si_3N_4. This is attributed to the influence of better bonding of gold with Si and to the greater conductivity of Si which minimises space charge effects during FIB fabrication. Instabilities are reduced still further for the same reason by the use of highly doped Si. FIB heating effects cannot be excluded as a contributory factor due to local transient beam induced melting during FIB etch, an effect which is worthy of further study. The Buffer HF treatment of Si to remove the native oxide from the surface, gives improved resistance to instability due to the much improved adhesion of the gold film. The instabilities investigated in this study could severely limit the use of gold nanowires in nanosensors and other nanoscale devices. The instabilities can ultimately lead to break-up of the nanowires into islands of metal and are clearly of the Rayleigh-Plateau type. On insulating substrates there is also clear evidence of electrohydrodynamically formed Taylor Cones that form due to charging during patterning by FIB or during the inspection in SEM.

5.6 References

[1] Petty M. C. Molecular Electronics, *Molecular Electronics: From Principles to Practice*, (2007), Weinheim: Wiley – VCH.

[2] Mooij J. E., Nazarov Y. V., *Superconducting nanowires as quantum phase-slip junctions*, Nature Physics, 2006, **2**: p 169-172.

[3] Kelly M. J., *Intrinsic top-down unmanufacturability*. Nanotechnology, 2011, 22: p 245303.

[4] Nichols F. A., Mullins W. W., *Surface (Interface) and Volume Diffusion Contributions to Morphological Changes Driven by Capillarity.* Trans. Metal. Soc. AIME, 1965**, 233**: p 1840.

[5] Hobi E. Jr, Fazzio A., da Silva A. J., *Temperature and Quantum Effects in the Stability of Pure and Doped Gold Nanowires*, Phys Rev Lett., 2008,**100**(5): p 056104.

[6] Plateau, J., *Transl. Annual Reports of the Smithsonian Institution*, 1873, p 1863.

[7] Lord Rayleigh, Proc. Longon Math. Soc, 1878, 10: p 4.

[8] Naik J. P., Prewett P. D., Das K., Raychaudhuri A. K., Instabilities in Focused Ion Beam-Patterned Au Nanowires, Microelectronics Engineering, 2011, 88: p 2840-2843.

[9] Tuboltsev V., Raisanen J., *Ion beam processing of gold nanowires*, Nanotechnology, 2009 **20**: p 335302.

[10] Parravicini G. B., Stella A., Ungureami M. C., Merli P. G., Migliori A., Kofman R., *New approach to study melting processes in metal nanoparticles: capacitance measurements*, Physica Status Solidi (B), Applied Research, 2003, **237** (1): p 374-380.

[11] Taylor G I, *Disintegration of water drops in an electric field*, Proc. R. Soc., London AV., 1964, **280**: p 383–397.

[12] Takagi M., *Electron-Diffraction Study of Liquid-Solid Transition of Thin Metal Films*, J Phys. Soc. Jpn., 1954, **9**: p 359.

[13] Bid A., Bora A., Raychaudhuri A. K., *Low frequency conductance fluctuations (1/f_ noise) in 15nm Ag nanowires-Implication on its stability*, Phys. Rev B, 2005, **72**: p 113415.

[14] J Burki, C A Stafford, *On the stability and structural dynamics of metal nanowires*, Appl. Phys. A, 2005, 81: p 1519–1525.

[15] S. Chandrasekhar, *Hydrodynamic and Hydromagnetic Stability*, Dover press, New York, 1981, p 515–574.

[16] Zhang C.H., Kassubek, F. Staford C.A., *Surface Fluctuations and the Stability of Metal Nanowires*, Phys. Rev B, 2003, 68: p 165414.

[17] Daniel F Urban, Dissertation, Stability, *Symmetry Breaking, and Scaling Properties of Metallic Nanowires*, Albert Ludwigs University, Berlin, January 2006.

[18] Toimil-Molares M. E., Balogh A. G., Cornelius T. W., Neumann R., Trautmann C., *Fragmentation of nanowires driven by Rayleigh instability*, Appl. Phys. Lett., 2004, 85: p 5337

[19] Karim S., Toimil-Molares M. E., Balogh A. G., Ensinger W., Cornelius T. W., Khan E. U., Neumann R., *Morphological evolution of Au nanowires controlled by Rayleigh instability*, Nanotechnology, 2006, 17: p 5954-5959.

[20] Qin Y, Lee S-M, Pan A, Gosele U, and Knez M, *Rayleigh-instability-induced metal nanoparticle chains encapsulated in nanotubes produced by atomic layer deposition*.Nano Lett., 2008, **8**: p 114-118.

[21] Zhao K., Averback R. S., Cahill D. G., *Patterning of metal nanowires by directed ion-induced dewetting*, Appl. Phys. Letts, 2006, **89**: p 053103.

[22] Prewett P D, Mair G L R, *Focused Ion Beams from Liquid Metal Ion Sources*, J Wiley Microengineering Series, Electronic and Electrical Engineering Research Studies, 1991, p 155-258.

Chapter 6

Study of Electrical Properties of Nanowires Fabricated by Focused Ion Beam Metal Deposition

6.1 Introduction

For MEMS or NEMS devices to function effectively, it is desirable to have precise knowledge of the piezoresistive effects in nanowires and the force generated by microscopic actuators such as bimorph cantilevers, which are of significant interest in the application of nanoscale strain gauges. This chapter describes a two stage experimental study on the fabrication method and the behaviour of a bimorph cantilever. The research was carried out in collaboration with Mr Manotosh Chakravorty from DST Unit for Nanoscience, Department of Material Sciences, S. N. Bose National Centre for Basic Sciences, Kolkata, India with the sponsorship and support of UKIERI (British Council, HMG). My contribution was to design and fabricate the nanowires as well as the four probe connection to the nanowires, which had a width and thickness ranging from 50 – 150 nm, which is described in this chapter. I also designed and fabricated the stencil mask for the contact pads, the process parameters for which are described in Chapter 3.3. Mr Chakravorty was responsible for designing and conducting the electrical measurements. Interpretation of the experimental results and subsequent publication [1] were a joint effort including also our supervisors Professor Philip D Prewett and Professor Arup K Raychaudhuri.

The first *Section **A*** includes the fabrication of platinum (Pt) nanowires on an oxidised silicon wafer, using FIB metal deposition, and then the measurement and understanding of their temperature dependent resistance. It has been reported that FIB deposited Pt nanowires are carbon-metal composites, which can be described as a two phase 3D percolating system [2]. If this is correct then the nanowire will have a negative temperature coefficient of resistivity (NTC). The first section of this research also investigates the temperature dependent resistivity of nanowires, of length ranging from 5 – 20 μm, deposited by Focused Ion Beam induced decomposition of an organometallic precursor. A number of 4 – terminal resistance measurements were carried out on the nanowire. We have experimentally shown that the observed electrical transport depends on the metal content and can be described using theories of disordered conductors in the presence of Coulomb charging [3] or by multi-step tunnelling between metal grains through the intervening composite phase [4-5]. The experiments conducted on the FIB grown nanowires contrasts with work carried out by Raychaudhuri *et al* [6-7] on the single crystal nanowire of 15 nm diameter demonstrating metallic conduction characterised by positive temperature coefficient of resistance.

In the second *Section **B*** nanowires fabricated in this way are used to create a multiple meander heater on the bimorph cantilever. Subsequently an Atomic Force Microscope was used to measure the force generated in the bimorph cantilever fabricated in a silicon nitride membrane using Focused Ion Beam prototyping. These experiments include, prototype Si_3N_4/Au bimorph microcantilevers of length < 10 μm, which were made using Focused Ion Beam (FIB) etch and metal deposition, where their force – deflection actuation characteristics were measured accurately using an Atomic Force Microscope (AFM). These actuators are reproducible and can be characterised accurately for the deflection and force produced for a given “drive” current. These types of cantilevers can also be used as micromechanical switches as reported by Majumbar *et al* [8]. Battiston *et al* [9] have fabricated a micro-

cantilever array to be used as a chemical sensor using the method of simultaneous resonance-frequency and bending readout. Lammel *et al* [10] used a laser beam to calibrate actuation measurements. Focused Ion Beam (FIB) technology provides a useful tool for the development and prototyping of experimental nanotechnology devices. For example FIB metal deposition can be used to modify prototype chips by making or breaking connections. Compared to making mask changes, which can take weeks and be expensive, the use of FIB metal deposition allows the changes to be made in a matter of hours [11].

Previously, Teng *et al* [12] and Al Aioubi *et al* [13] used FIB to fabricate similar bimorphs but somewhat larger microcantilevers (approximately 100 microns in length). They were able to measure deflection using SEM and optical beam lever methods respectively. In both cases, the measurements of deflection were relatively inaccurate and force was not measured at all. We have undertaken simultaneous measurement of displacement and force with a high degree of accuracy due to the use of direct contact between the tip of the actuator and the AFM tip.

A combination of Focused Ion Beam milling and metal deposition using organometallic precursor gas has been used to form the platinum nanowire in both sections of the experiment. The metal deposition of platinum (Pt) using FIB is usually achieved by the ion beam decomposition of carbon rich precursors like methylcyclopentadienyl platinum trimethyl $(CH3)_3(CH3C5H_4)Pt$. Such precursors lead to Pt films with high resistivity (ρ) and the negative temperature coefficient of resistivity (NTC) where the temperature coefficient $\beta = \frac{1}{\rho}\frac{d\rho}{dT}$ can vary by a large amount depending on the carbon content in the film [3, 4]. Experimental data in this chapter are typical of approximately 10 similar results.

6.2 Section A

6.2.1 Percolating System

As previously stated, FIB deposited Pt nanowires can be described as a percolating system. It has been known for some time that micro or nano structures produced using FIB metal deposits contain carbon from the decomposed precursor as the majority phase and that gallium from the incident beam is also incorporated [3-5]. Energy dispersive x-ray spectroscopy showed the nanowires are composed of up to 70% by volume carbon, the remainder being principally platinum and gallium from the ion beam. The experimental evidence demonstrates that the metallic phase exists in the form of nano clusters, randomly distributed in the matrix of carbon. Measured data are in line with the observation, demonstrating the conduction threshold effect which is typical of percolation models for electron transport. Results show an unexpected temperature dependence of resistivity also consistent with thermal strain effects due to the mismatch in thermal coefficients of expansion between the nanowire and the silicon dioxide substrate. The observed phenomenon can be incorporated in MEMS and NEMS devices for temperature measurement and strain sensor applications.

In such a system, the volume concentration of the conducting material plays the key role and a threshold concentration of the conducting phase is expected to be present in experimental data. The resistance of the system is most sensitive to the volume fraction of the percolating metallic phase and, above threshold, the inter-particle separation and corresponding resistance are sensitive to small changes in strain. The aim of this work is to consider these effects in FIB deposited nanowires with a range of metallic platinum concentration determined by variation of beam energy. The work presented here is not an extensive consideration of the deposited Pt as a percolating system, but it reveals new experimental

information concerning the strain dependent behaviour of Pt-C nanowires when the metal content is close to the percolation threshold.

6.2.2 Sample Preparation for 4 – Probe Electrical Measurements

The nanowires were fabricated using two similar types of FIB system; initial work for the sample preparation was carried out at University of Birmingham using the FEI Strata^{TM} Dual Beam 235 FIB/SEM, however, at DST Unit for Nanoscience, Department of Material Sciences, S. N. Bose National Centre for Basic Sciences, the Dual Beam Helios 600 system from FEI was also used for the four probe connections. A precursor gas of methylcyclopentadienyl platinum trimethyl $(CH_3)_3(CH_3C_5H_4)Pt$ was decomposed by a gallium ion (Ga^+) beam with four different beam energies to form the Pt-C composite nanowires. The beam current was in the range 28 – 30 pA in each case. The length of the

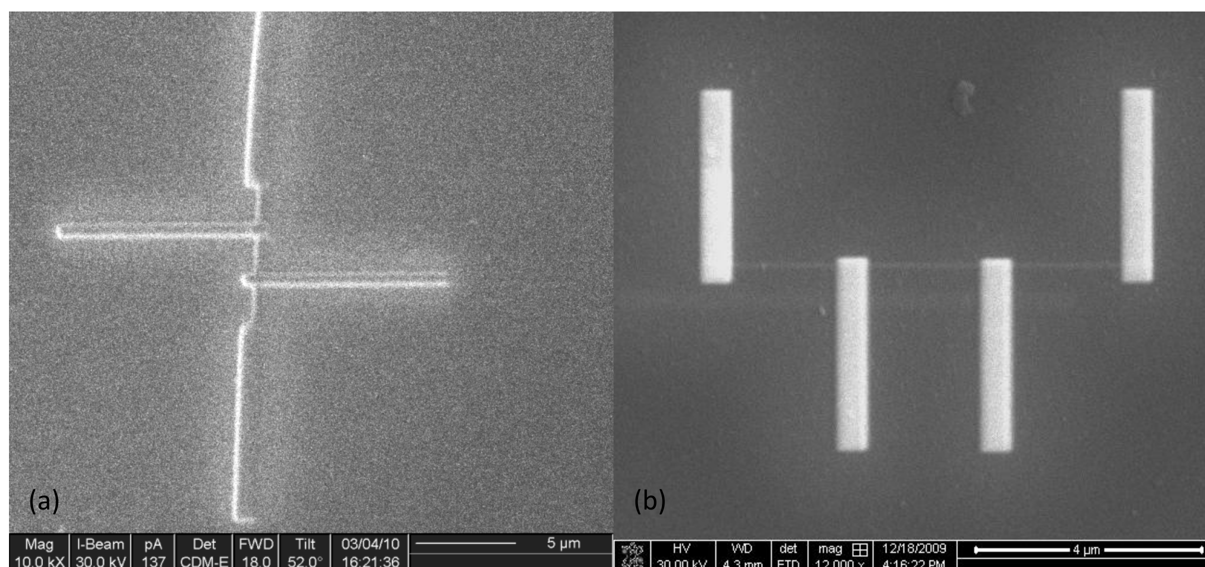

Figure 6.1: (a) Ion beam image of 4 – probe connection on nanowire of length 5 μm and width and thickness of 130 nm deposited by FIB at 29 pA on Si_3N_4 substrate. (b) SEM image of nanowire of length 5 μm and width and thickness of 50 nm deposited at 29 pA on SiO_2 substrate.

nanowire was ranged from 5 – 20 μm with width and thickness ranges of approximately 50 – 150 nm. They were grown on a bi-layer substrate of approximately 190 nm thick silicon dioxide (SiO_2) on a 525 μm thick silicon (Si) wafer and 200 nm thick silicon nitride (Si_3N_4) membrane on 7.5 x 7.5 mm silicon chip with a window of 200 x 200 μm. Figure 6.1 shows

the sample images taken while in preparation. Figure 6.1(a) shows the ion beam image of 4 – probe connection on nanowire of length 5 μm and width and thickness of 130 nm deposited by FIB at 29 pA on Si_3N_4 substrate. Figure 6.1(b) shows the SEM image of 4 – probe connection on nanowire of length 5 μm and width and thickness of 50 nm deposited by FIB at 29 pA on SiO_2 substrate. Contact pads of Au on a Cr adhesion layer were formed on the oxide layer by deposition through a silicon stencil mask. The latter was produced by contact optical lithography using an acetate film mask, followed by plasma etching completely through the wafer using an STS 100 inductively coupled plasma etcher with a gas mixture of SF_6/O_2. The shortest distance between contact pads was 200 μm and the final connection to the nanowire was made by FIB deposition of Pt interconnects. These were 1 μm wide and 500 nm thick, deposited at 30 keV beam energy and 28 pA beam current. The effects of contact resistances on subsequent electrical measurements on the nanowires were avoided by using four probe connections to the contact pads. The experimental chip containing the nanowires was mounted onto a DIL chip carrier and a gold wire bonder was used to connect the contact pads to the carrier legs. Figure 6.2 shows the nanowire sample connected to the contact pads using interconnects.

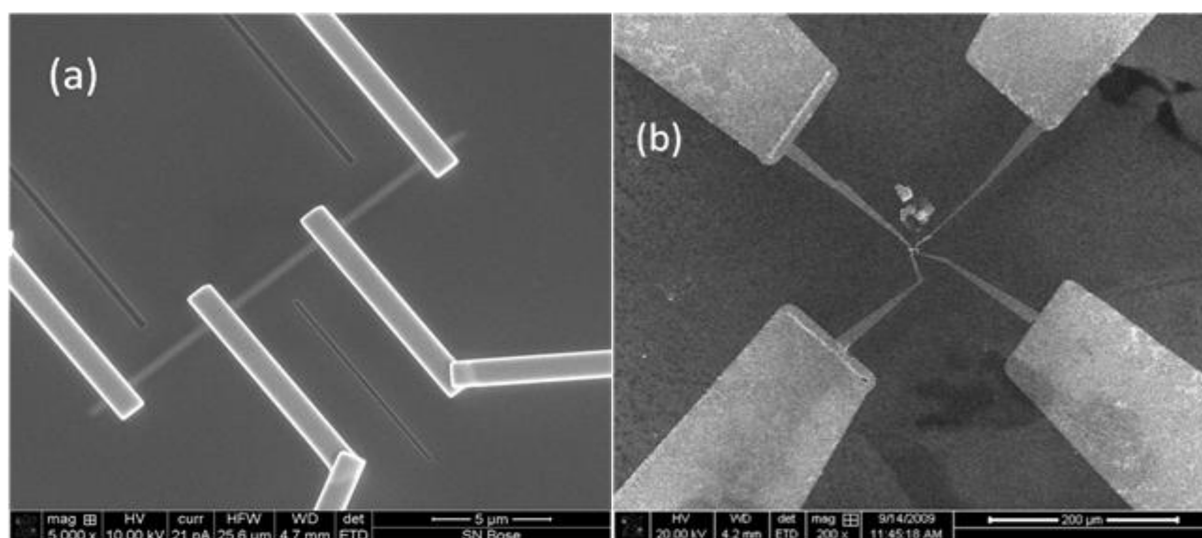

Figure 6.2**:** (a) 4 – probe connection on FIB deposited nanowire of length 20 μm (b) Demagnified view showing FIB deposited electrical connections to Au/Cr contact pads [1].

6.2.3 Microscopic Analysis of the 4 – Probe Nanowire Sample

Energy Dispersive X-ray (EDX) analysis, using a Field Emission Scanning Electron Microscope (FEGSEM), was carried out at S. N. Bose National Centre to determine the composition of the wires grown by varying the Ga^+ ion accelerating voltage. This confirmed that the FIB deposited structures are essentially a C-Pt composite. This composite also contains Ga from the ion beam bombardment, but this is at lower levels, depending on the deposition energy. In the discussion and analysis of conduction mechanisms which follows, we therefore choose to treat the nanowires as a two-component composite conductor with low resistivity islands mostly composed of Pt inside a higher resistivity matrix composed principally of carbon. It is not clear whether the Ga is uniformly distributed in this matrix or whether it too clusters either with the Pt or separately. However, because of the relatively low levels of Ga, this is a second order effect, which may require further study. The EDX data presented in Table 6.1 (next page) shows how the

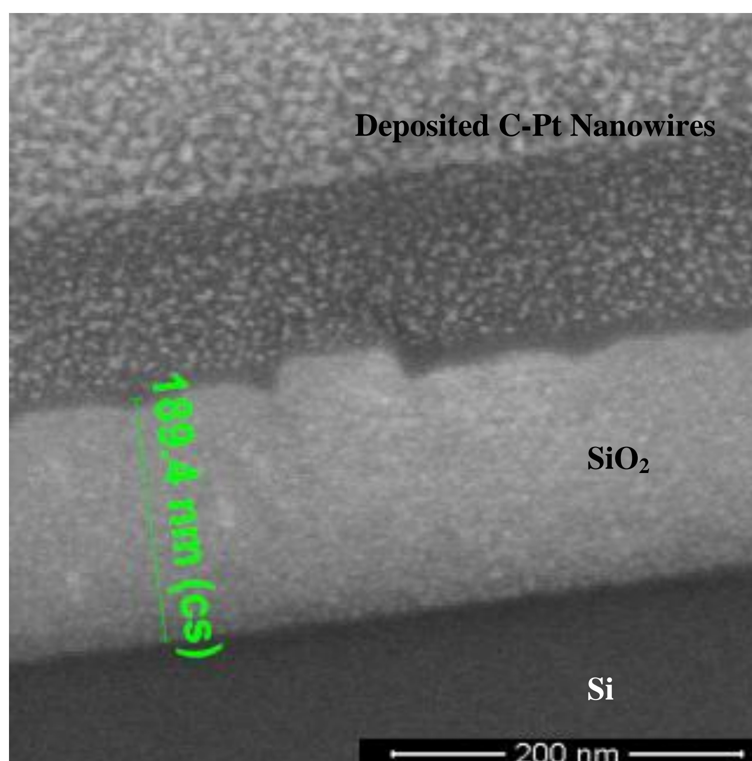

Figure 6.3: Cross-section of FIB deposited C-Pt on SiO_2/Si wafer substrate. Pt islands are distributed in a high resistivity carbon matrix [1].

Pt component in the nanowire increases with the kinetic energy of the beam. This is due to the increased number of secondary electrons at higher beam energy which are available to break the chemical bonds of the organometallic precursor molecule. Since the bulk electrical resistivity of Pt $(1.06\times10^{-8}\Omega m)$ and Ga $(1.47\times10^{-8}\Omega m)$ are three orders of magnitude smaller than that of amorphous carbon $(1.5\times10^{-5}\Omega m)$, the model of conducting clusters or nanoparticles in a non conducting matrix, discussed in Section 6.2.5 below, is not unreasonable. The cluster size is typically 7 nm with spacing ~ 15 nm, as seen from the cross sectional data in Figure 6.3.

Table 6.1: Volume concentration of conducting and non conducting elements with FIB energy at 28 pA beam current (+/- 0.1%) [11]

Sample	Beam Energy (keV)	Vol% of conducting component (Pt+Ga)	Vol% of non-conducting component (principally C)
S1	10	30.8	69.2
S2	20	33.7	66.3
S3	25	36.0	64.0
S4	30	37.0	63.0

6.2.4 Temperature Sensitive Resistivity Measurements of the 4 – Probe Nanowire

The electrical measurements were carried out in a closed cycle helium refrigerator at temperatures ranging from 50 ºK to 300 ºK at a base pressure ~ 10^{-5} mbar. The electrical measurement experiments were carried out by Mr Manotosh Chakravorty from DST Unit for Nanoscience, Department of Material Sciences, S. N. Bose National Centre for Basic Sciences, Kolkata, India. 4 – probe current-voltage measurements were carried out at 63.33 Hz using a phase-sensitive AC technique [6]. This method avoids thermoelectric effects,

allowing greater accuracy to be achieved. To avoid damage to the composite by electromigration, the maximum current passing through the nanowire was kept below 5 μA.

6.2.5 Analysis of the Results in 4 – Probe Electrical Measurements

As explained earlier in Section 6.2.3, the SEM image in Figure 6.3 demonstrates the cross-section of Focused Ion Beam deposited platinum nanowire, where the

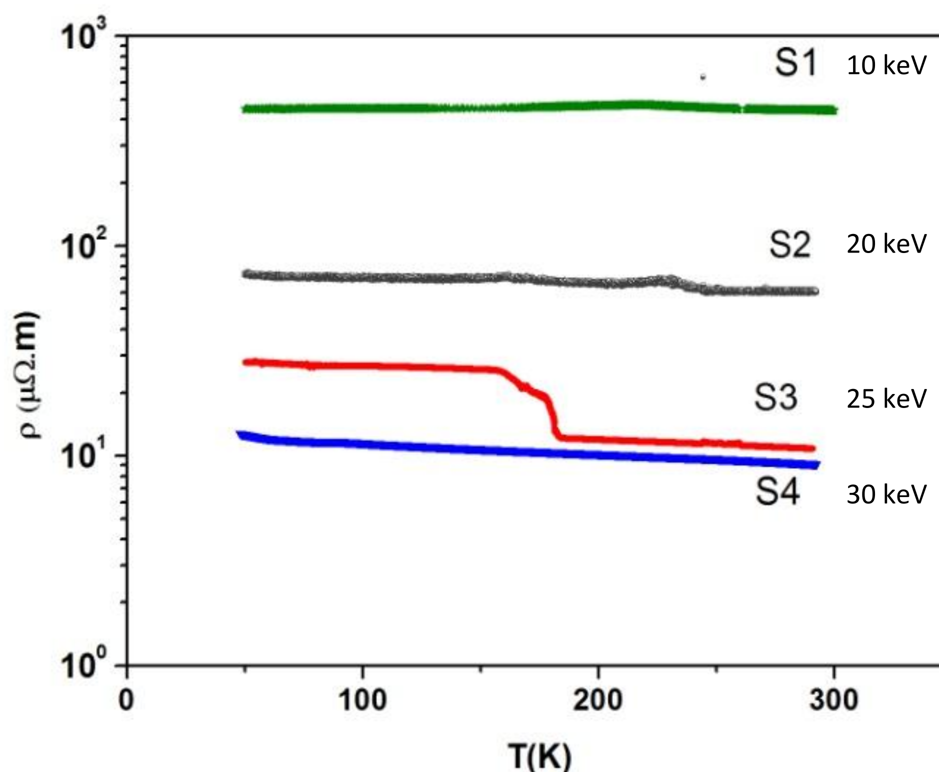

Figure 6.4: Resistivity vs Temperature of four nanowires (S1 - S4) [1].

top layer is the deposited Pt-C composite material. The brighter areas of the image show islands of Pt surrounded by the carbon matrix, which is represented by the darker areas of the image. Figure 6.4 shows the resistivity (ρ) versus temperature measurements on four nanowires with different volume concentrations of Pt deposited by FIB.

The measured data demonstrates variation of negative temperature coefficient of resistivity, β. At the room temperature of 272.3 °K the value of $\beta = -0.0003\ K^{-1}$ increases to $\beta = -0.0018$

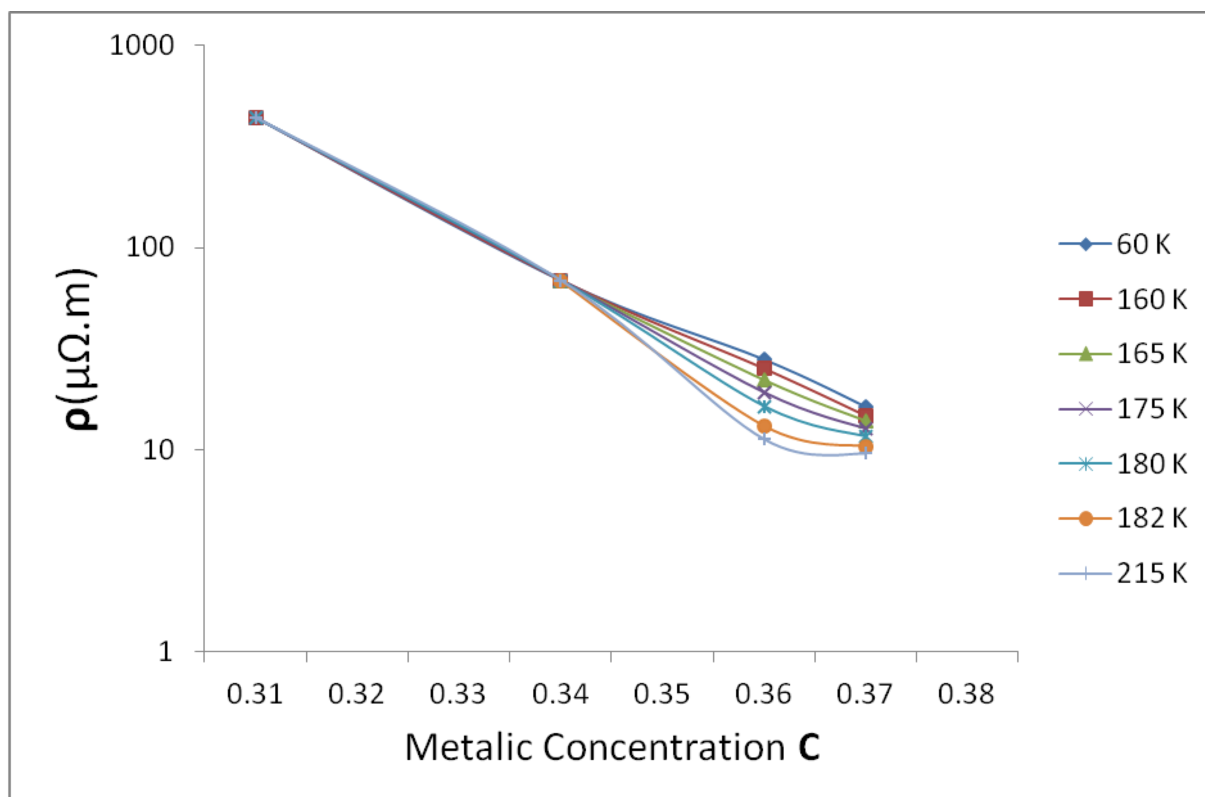

Figure 6.5: Resistivity (ρ) Vs Metallic Concentration (C) for different temperatures [1].

K^{-1} with the decrease in temperature of 228.8 °K in contrast to the amorphous carbon of β = -0.0005 K^{-1} at room temperature. The resistivity decreases significantly with reduction in carbon concentration due to relatively increased metallic phase concentration. Eventually the effect flattens out beyond a total metallic phase concentration of 36% (17.5 At% Pt, 7.9 At% Ga) as shown in Figure 6.5. The measurements support the threshold effect predicted by percolation theory, where resistivity decreases ~ 40 times with respect to variation of concentration from 31% to 36%. However the effect is significantly smaller (~ 1.2 times) for concentration variation from 36% to 37%. These should be compared to the work of Fernández-Pacheco *et al* [3], which indicated the thickness induced insulator to metal transition occurring for concentrations of ~ 17.5 At% Pt, 10 At% Ga. They did not consider the C concentration. Our threshold resistivity of 10 Ωm is very close to the value of 30 Ωm reported by Fernández-Pacheco *et al* [3].

Figure 6.5 shows that the measured data are consistent with the composite 3D percolation model of conduction, with a matrix of C with a conducting phase of Pt contaminated with Ga. The volume concentration of the conducting component increases with beam energy until the critical concentration of 36% is reached. This suggests a resistivity dependence on volume concentration v according to Equation 6.1 [2],

$$\rho = \rho_0 + A|v - v_c|^a \tag{6.1}$$

where ρ_0 is the "background" resistivity of the C-Ga matrix, A is Avogadro's number and the second term is the percolation resistivity, subject to a threshold effect at the critical metallic volume concentration (CMVC) value v_c [2]. Standard percolation theory [2] suggests a value of ~ 30 vol% compared with our experimental result of 36 vol%. This discrepancy may arise from the nature of the interface for the C-Pt nano-composite which, if strongly insulating as in our case, could change the threshold to a higher volume fraction. Evaluation of the critical exponent α requires more detailed experimental measurements near threshold and is beyond the scope of the present work.

The second effect that we observe reproducibly is the anomalous temperature dependence of the resistivity, seen near 150 °K only when the metallic phase concentration is near the 36 vol% threshold value. This is visible in Figure 6.5 as a jump in resistivity in the temperature range 175 °K to 150 °K. It is not seen when the concentration is other than very close to critical, either above or below. We propose that this effect is due to the nano-composite nanowire's enhanced sensitivity to strain near the percolation threshold. Thermal induced strain in the nanowire increases the interparticle separation of the conducting nanoparticles, consequently reducing the metallic component volume concentration, thus affecting the second term in Equation 6.1. The nanowire was deposited on the insulating SiO_2 surface of a bi-layer substrate of Si/SiO_2 and Si has greater thermal expansion coefficient than SiO_2 [14,

15], so that when the temperature is decreased, the curvature of substrate which is initially convex upwards as shown is reduced. The initial curvature creates a strain in the composite, which creates a tensile strain in the nanowire, provided adhesion is maintained. When the temperature of the system increases, the greater thermal expansion of the silicon reduces the curvature thereby also reducing the strain in the nanowire. The resistivity of the nanowire is therefore reduced with increase of temperature.

The strain difference (Δε) between Si and SiO_2 layer is given by Equation 6.2,

$$\Delta\varepsilon_{\mathrm{T}} = \int_{T_1}^{T_2} (\alpha_{Si} - \alpha_{SiO_2})dT \qquad (6.2)$$

where α_{Si} and α_{SiO_2} are the thermal expansion coefficients of Si and SiO_2 respectively.

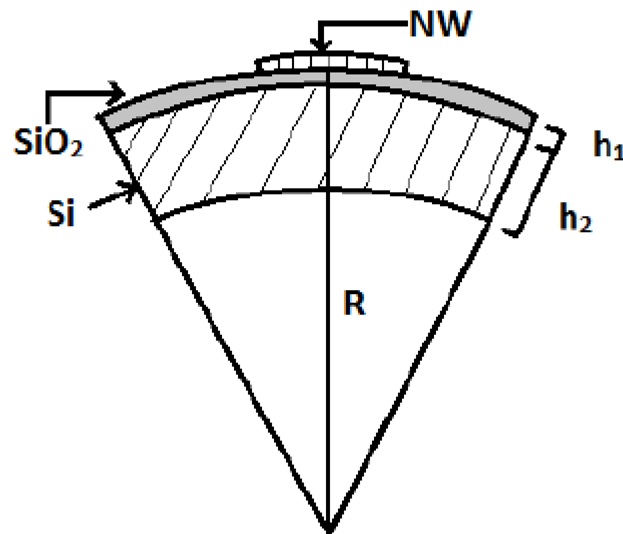

Figure 6.6: Deflection of the bi-layer substrate of Si and SiO_2 [1]

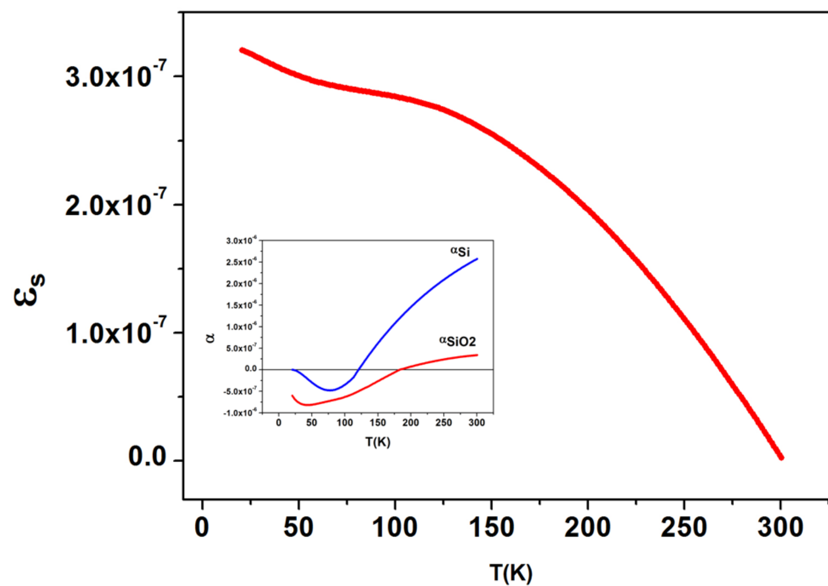

Figure 6.7: Surface strain (ε_s) due to bending of the substrate. Inset shows the thermal expansion coefficient (α) of Si and SiO_2 [1-2].

The radius of curvature (R) of the bent nanowire is given by Equation 6.3 [14],

$$\frac{1}{R} = \frac{6\Delta\varepsilon(1+m)^2}{h\left\{3(1+m)^2 + (1+mn)\left(m^2 + \frac{1}{mn}\right)\right\}} \tag{6.3}$$

where, $m = h_1/h_2$, $n = E_1/E_2$ and $h = h_1 + h_2$.

h_1, h_2 are the thicknesses of the bi-layer materials and E_1, E_2 are their Young's moduli values (see Figure 6.6).

Using simple geometry, from Figure 6.6 the surface strain can be easily expressed as

$$\varepsilon_s = \frac{(h/2)}{R} \tag{6.4}$$

The surface strain calculated from Equation 6.4 is shown in Figure 6.7. The tensile strain will increase the interparticle separation of the Pt islands thus reducing the overall volume fraction. The effect of strain is largely visible near the volume concentration of v_c, where ρ is

most susceptible to volume fraction changes. The strain in the nanowire is not sufficient to reduce the volume concentration below the CMVC so that the percolation model represented by the second term in Equation 6.2 still applies. However the volume concentration v is reduced sufficiently for the effect on resistivity to be apparent within the experimental temperature range. The trigger value of the temperature for the maximum change will be dependent on the exact composition and the proximity to v_c. The change in ρ will be most significant at that temperature when the strain induced change in v takes it through v_c.

Our observation suggests that the thermal strain in the nanowire is only $\approx 10^{-3}$ while the volume strain needed to cause a factor 3 change in resistivity near the percolation threshold is $\approx 2\times10^{-2}$. Thus, the strain effect at the percolation threshold cannot alone explain the magnitude of the observed resistivity change. The probable explanation is that the percolating system is augmented by electron tunnelling conduction between the metallic nanoparticles as discussed in [4]. Since the tunnelling probability varies as the exponential of the interparticle distance, a small strain induced increase in separation of the metallic nanoparticles produces a substantial increase in resistivity, as observed. In summary, the FIB fabricated Pt nanowire is a percolating two-component system with a significant contribution to conduction arising from tunnelling between adjacent nanoparticles. The strain/temperature resistivity effect associated with these composite nanowires make them of interest for strain gauge micro-sensor applications.

6.3 Section B

6.3.1 Sample Preparation for Bimorph Cantilever

This section concerns work on the fabrication and test of bimorph cantilever with meander Pt-C composite heater produced entirely using FIB. This prototype device can be used as a micro-actuator. The bimorph micro-cantilever was FIB-etched from a membrane of silicon

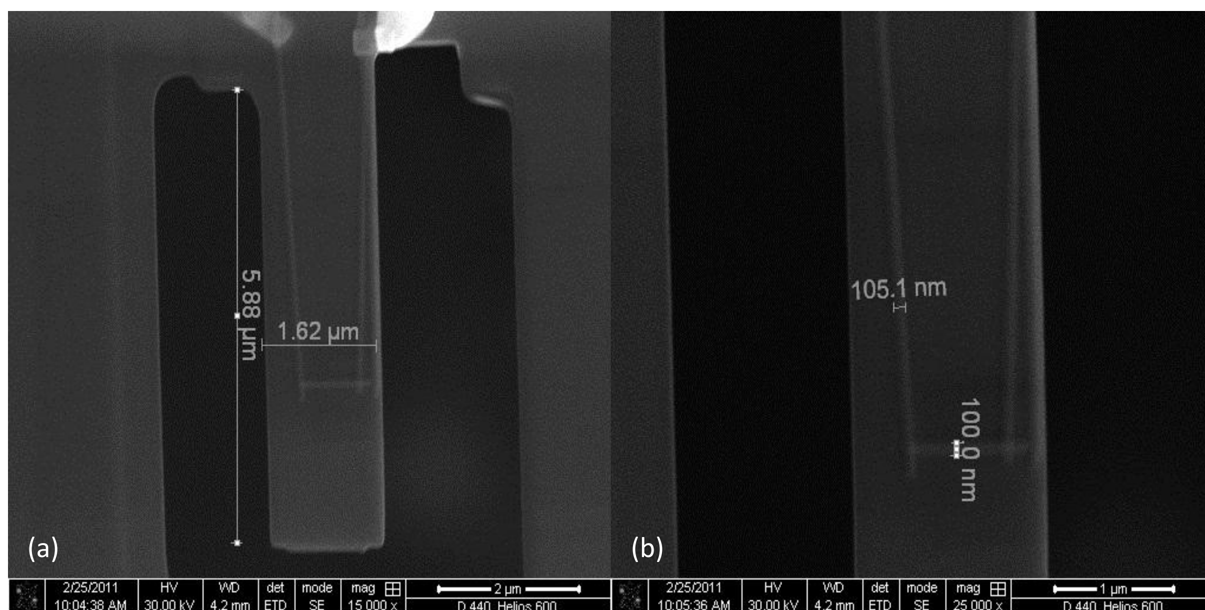

Figure 6.8: a) SEM image of cantilever (6 µm x 1.5 µm); b) single Pt heating meander of width of approximately 100 nm

nitride with a layer of gold on the back face. A meander pattern of Pt-C was deposited on the front face to form the heater using FIB deposition. The fabrication processes were carried out using the Helios Dual Beam 600 FIB-SEM tool at the S N Bose Centre for Research in the

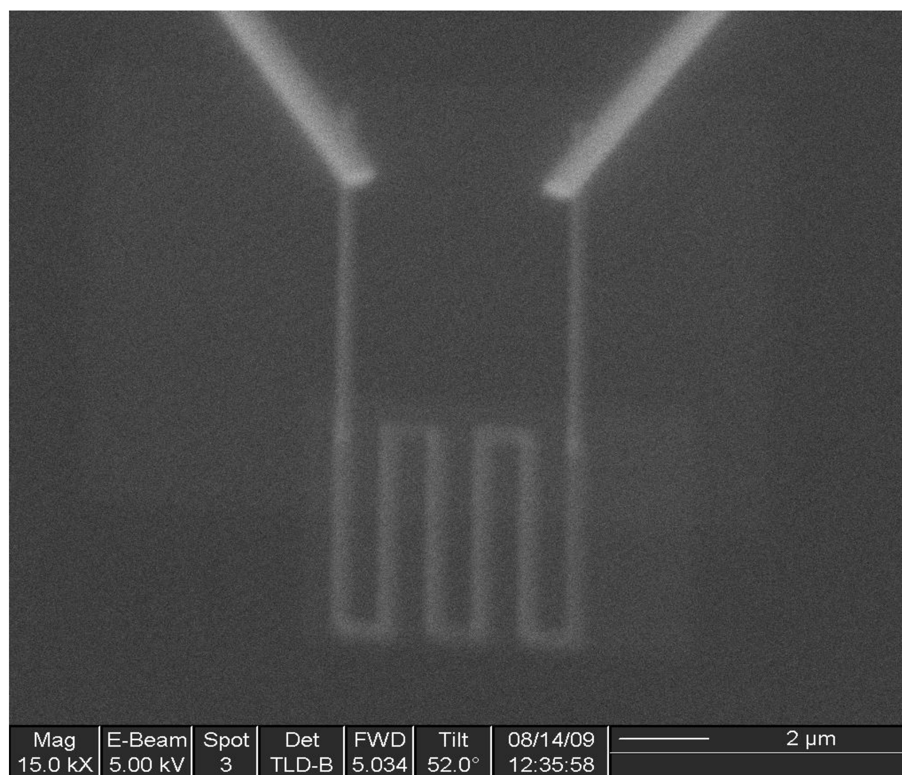

Figure 6.9: SEM image of triple meander Pt-C heater

Basic Sciences, Kolkata. A 200 nm thick silicon nitride membrane was etched by FIB milling to fabricate the cantilever with length 6 µm and width 1.5 µm. A back face coating of 65 nm thick Au was deposited by thermal evaporation coating. The Pt-C meander heater was deposited using a patterning beam of focused gallium ions at a beam energy of 30 keV with a precursor gas of methylcyclopentadienyl platinum trimethyl $(CH_3)_3(CH_3C_5H_4)Pt$. This process has been shown to produce a Pt-C composite which typically contains 33% clusters of Pt in a 67% carbon matrix This produces a strain and temperature dependent resistivity which has been explained using a percolation model [1] (See Section A, 6.2.1).

Figure 6.8 shows typical micro-cantilevers produced in this way; Figure 6.9 shows the triple meander Pt-C Heater. The heater ends were connected by Pt-C interconnects lines to gold contact pads on the silicon chip surrounding the nitride membrane. The contacts were formed by gold evaporation through a silicon stencil mask prior to the FIB prototyping.

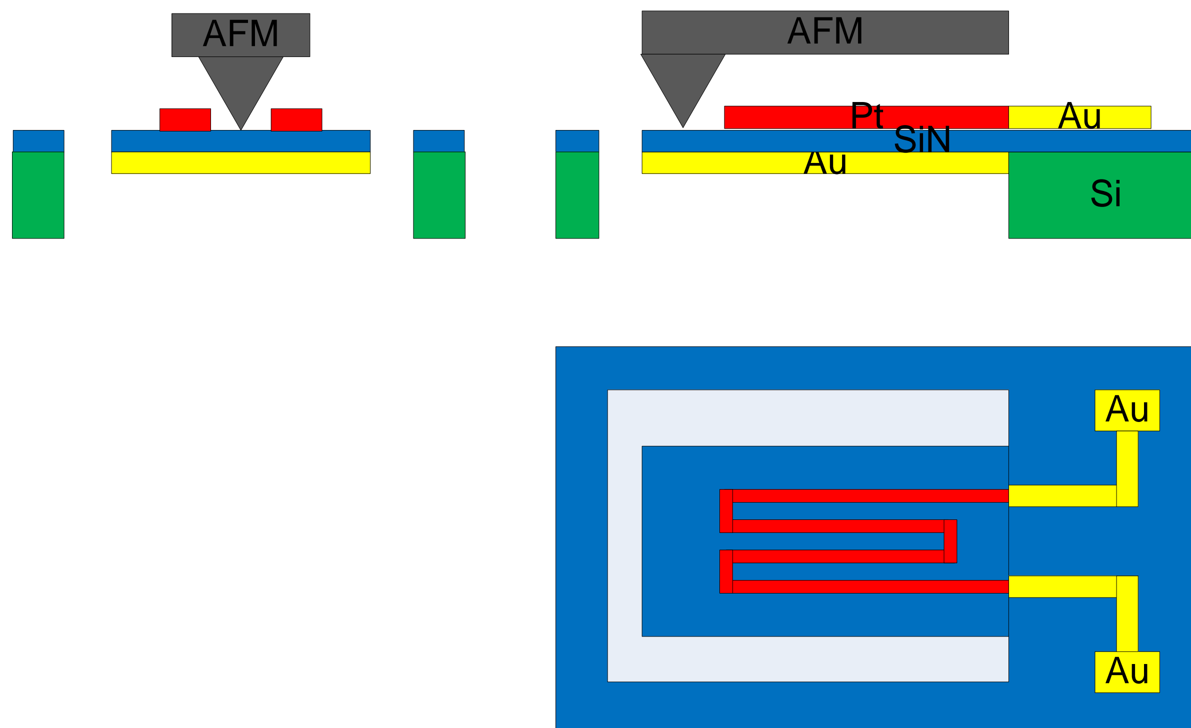

Figure 6.10: Schematic of the AFM Probe used to measure the force generated by the MEMS bimorph cantilever when a current is supplied through the Pt heater fabricated by FIB metal deposition on the surface of the Si_3N_4 membrane.

6.3.2 Force and Deflection Measurements on Bimorph Cantilever

For force measurements, the bimorph micro-cantilever was mounted under the AFM cantilever tip as shown in the schematic of Figure 6.10. The AFM tip was located at the end of the micro-cantilever to avoid damage to the heater or to the AFM tip by leakage current. The deflection sensitivity of the micro-cantilever, as measured by the AFM cantilever tip, takes the form of a force – deflection characteristic. The corresponding *I-V* characteristics of the FIB deposited Pt-C composite behaves linearly [1, 9]. The deflection can be calculated using the method of Teng et al [12, 16] using Equation 6.5, if the temperature difference (ΔT) is known,

$$\delta = 3(\alpha_1 - \alpha_2)\frac{(h_1 + h_2)}{(h_2)^2}\left[4 + 6\left(\frac{h_1}{h_2}\right) + 4\left(\frac{h_1}{h_2}\right)^2 + \frac{E_1}{E_2}\left(\frac{h_1}{h_2}\right)^3 + \frac{E_2}{E_1}\left(\frac{h_1}{h_2}\right)\right]^{-1} L^2 \Delta T \qquad (6.5)$$

where, $\alpha_1 = 1.42\times10^{-5}$ K^{-1} and $\alpha_2 = 3.3\times10^{-6}$ K^{-1} [1] is the thermal coefficient of expansion for the gold and silicon nitride membrane (Si_3N_4) respectively. According to this model, a temperature rise of just 0.83° K or C will produce a tip deflection of 1 nm. This high sensitivity is useful for NEMS actuators but the need for close control of environmental temperature is also highlighted. In our case, temperature is elevated locally by an on-board resistive heater and the bimorph actuator may be thought of as a current-deflection or current-force transducer. In these experiments, the force (*F*) is measured and converted to a deflection signal by AFM using the consolidated approach signal of the AFM cantilever tip in Figure 6.11. The effective force generated in the bimorph cantilever system (F_{eff}) can be calculated using the deflection signal (δ) in Equation 6.6,

$$F_{eff} = \frac{\delta(K_w K_c)}{K_w + K_c} \qquad (6.6)$$

where, K_w and K_c are the spring constants of the experimental cantilever and the AFM cantilever respectively. In this case, $K_c = 0.2$ N/m and the spring constant K_w for the bimorph

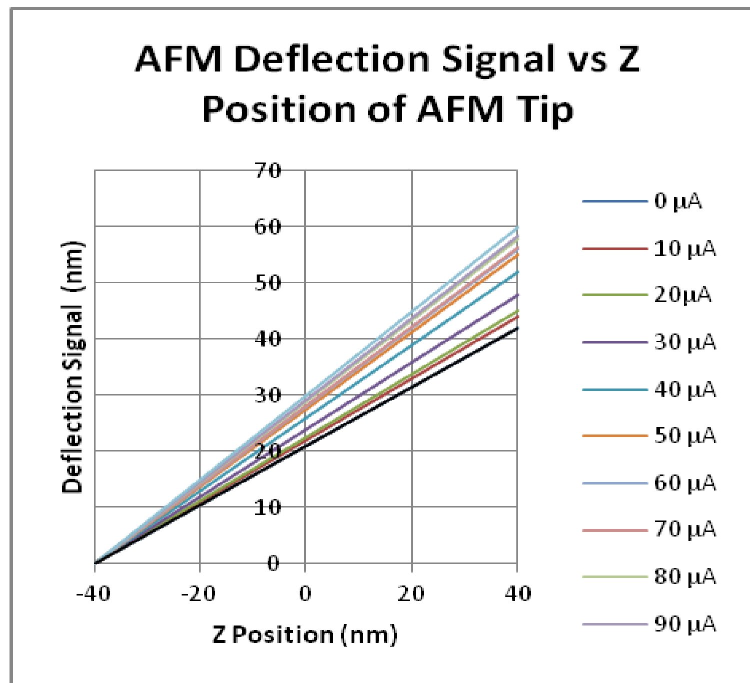

Figure 6.11: Consolidated approach signal from AFM tip
(used to measure Force/Deflection signal).

cantilever, with length *l*, width *w* and thickness *t* is K_w = 2.4 N/m, calculated from Equation 6.7 [17]:

$$K_w = \frac{Et^3 w}{4l^3} \tag{6.7}$$

where E is the elastic modulus of the bimorph cantilever. The change in the surface stress (σ_s) inside the bimorph is dependent on the radius of curvature (*R*), as shown in Equation 6.8 [17]:

$$\sigma_s = \frac{Et^2}{6R(1-\upsilon)} \tag{6.8}$$

where, υ is Poisson's ratio for the silicon nitride membrane.

6.3.3 Analysis of the Results from Measurements on Bimorph Cantilever by AFM

Application of a heating current (*I*) to the MEMS bimorph cantilever produced the expected upward bending due to the difference in the coefficient of expansion of the gold and silicon nitride layers. The current was initiated at 10 µA and increased in increments of 10 µA to a maximum of 100 µA. The end of the micro-cantilever was consequently deflected to push

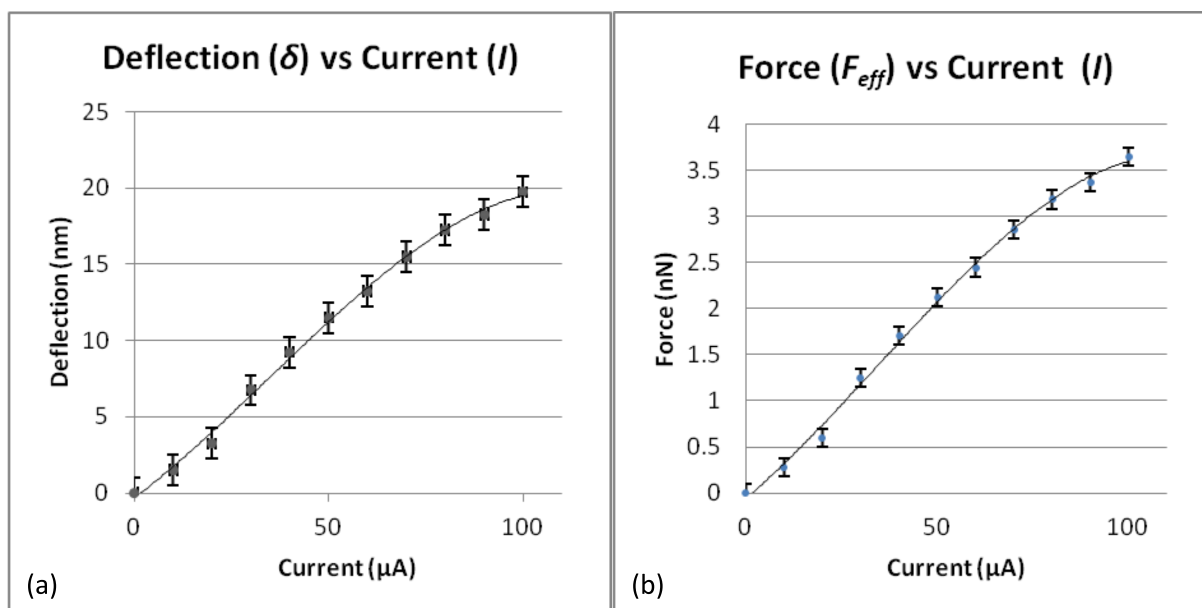

Figure 6.12: (a) Current (***I***) vs Deflection (***δ***), (b) Force (***F**eff*) vs Current (***I***)

against the AFM cantilever. Figure 6.12(a) shows this deflection as a function of the heater current. The deflection is nonlinear with respect to increase in current. This non linearity can be explained by the fact that the heater was deposited on the top of the silicon nitride (Si_3N_4) membrane using FIB metal deposition, which is a percolating system (described in Section A, 6.2.1). The deflection output signal was recorded during the heating and cooling process at similar stages and the error bars (<10 nm) shows the standard deviation in the output signal during heating and cooling, demonstrating the accuracy of the measurements. The deflection sensitivity is in the range of 1 – 4 nm /10 µA, which is higher than previously reported [12, 13, 18]. The effective force was calculated using Equation 6.6 and was found to vary with current as shown in Figure 6.12(b). The effective force (F_{eff}) generated in the micro-cantilever system is in the range of 0 – 4 nN for the supplied current range of 0 – 100 µA. Force as a function of drive current also appears to be nonlinear. Figure 6.12(a) shows that the deflection sensitivity reduces above 100 µA drive current.

6.4 Conclusion

In this chapter a fabrication technique to form Focused Ion Beam deposited platinum nanowires was presented. In the first section of the chapter, Section A, a study of beam energy dependence of metallic concentration and electrical measurement of consequential behaviour was carried out. The results of this study indicate that nanowires formed with such a process are a composite percolating system, where the metallic and insulating temperature dependant behaviour demonstrates the existence of the both phases simultaneously. The study demonstrated the percolation controlled conduction mechanism with a CMVC of 36% compared with predictions of 30% from standard percolation models and anomalous temperature dependence of resistance for metallic volume concentrations at 36%. This is the evidence for a percolation mechanism and can be explained by temperature induced strain in the nanowires, which changes the metallic volume concentration. However, the unexpectedly high magnitude of the resistivity change suggests that inter-particle electron tunnelling plays a significant role in the conduction mechanism. This deviation from the common type of strain effect might be exploited to fabricate actuators which can be suitable for simple nanosensor strain gauges, gas sensors or thermometers. The effect of thermally driven strain combined with tunnelling conduction on Focused Ion Beam deposited platinum, provides an opportunity for strain tuned resistance and strain gauge nanosensor applications.

In the second section of the chapter, Section B, experiments were conducted on the performance of a MEMS bimorph cantilever fabricated using FIB milling and metal deposition. An AFM was used to measure deflection and effective force generation as a function of drive current to the integrated heater. This is a direct measurement involving physical contact with the cantilever. In comparison with the indirect measurements by Teng and Al Aioubi this is thought to provide higher precision, though this has not been quantified.

The experiments on the micro-cantilever system showed higher deflection sensitivity than previously reported. However, the deflection and the force generated in the system are nonlinear. The experiment also demonstrates that due to the higher temperature sensitivity, the thermal isolation of any MEMS or NEMS device is an absolute requirement for controlled behaviour.

6.5 References

[1] Manotosh Chakravorty, Kaustuv Das, A. K. Raychaudhuri, J P Naik and P D Prewett, Temperature dependent resistivity of platinum–carbon composite nanowires grown by focused ion beam on SiO2/Si substrate. Microelectronic Engineering. 2011, 88: p 3360–3364.

[2] Scott Kirkpatrick, Percolation and Conduction. Rev. Modern Phys. 1973, 45: p 574.

[3] Fernández-Pacheco A., De Teresa J. M., Córdoba R., Ibarra M. R., Metal-insulator transition in Pt-C nanowires grown by focused-ion-beam-induced deposition, Phs. Rev. B., 2009, 79: p 174204.

[4] Pe˜nate-Quesada L., Mitra J., Dawson P., Non-linear electronic transport in Pt nanowires deposited by focused ion beam, Nanotechnology, 2007, 18: p 215203.

[5] Lin J. F., Bird J. P., Rotkina L., Bennett P. A., *Classical and quantum transport in focused-ion-beam-deposited Pt nanointerconnects*, Appl. Phys Lett., 2003, **82**: p 802.

[6] Bid A., Bora A., Raychaudhuri A. K., *Temperature dependence of the resistance of metallic nanowires (diameter ≥ 15nm): Applicability of Bloch-Gruneisen theorem*, Phys Rev B, 2006, **74**: p 035426.

[7] Kamalakar M. V., Raychaudhuri A. K., *Low temperature electrical Transport in ferromagnetic Ni Nanowires*, Phys Rev B, 2009, 79: p 205417.

[8] Majumder S., McGruer N. E., Zavracky P. M., *Electrostatically actuated micromechanical switches*, J. Vac. Sci. Technol. A, 1997, **15**: p 1246–1249.

[9] Battiston F. M., Ramseyer J. P., Lang H. P., Baller M. K., Ch. Gerber, Gimzewski J. K., Meyer E., Guentherodt H. J., *A chemical sensor based on a microfabricated cantilever array with simultaneous resonance-frequency and bending readout*, Sensors and Actuators B, 2001, **77**: p 122–131.

[10] Lammel G., Schweizer S., Renaud P., *Optical Microscanners and Microspectrometers Using Thermal Bimorph Actuators*, Kluwer Academic Publishers, Dordrecht, 2002.

[11] Giannuzzi L. A., Stevie F. A., *Introduction to Focused Ion Beams*, Springer, Boston, 2005, p 88.

[12] Teng J., Prewett P. D., *Focused ion beam fabrication of thermally actuated bimorph cantilevers*, Sensors and Acuators A, 2005, **123–124**: p 608–613.

[13] Al Aioubi M. Y., Djakov V., Huq S. E., Prewett P. D., *Deflection and load characterisation of bimorph actuators for bio-MEMS and other applications* Microelectronic Engineering, 2004, **73–74**: p 898–903

[14] Lyon K.G., Salinger G. L., Swenson C. A., White G. K., *Linear thermal expansion measurements on silicon from 6 to 340 K*, Journal of Applied Physics, 1977, **48**: p 865.

[15] G. K. White, *Thermal expansion of reference materials: copper, silica and silicon*, J. Phys. D: Appl. Phys., 1973, **6**: p 2070.

[16] S. Timoshenko, Bending and buckling of bimetallic strips, J. Opt. Soc. Am. 11 (1925) 233–256.

[17] Gere J. M., Timoshenko S. P., Mechanics of Materials, 1990, Boston, Massachusetts, **Chapter 5**, p 868-882.

[18] Gaspar J., Chu V., Louro N., Cabeca R., Conde J. P., *Thermal actuation of thin film microelectromechanical structures*, Journal of Non-Crystalline Solids, 2002, **299–302**, p 1224–1228.

Chapter 7

Atomic Force Microscope Study of Mechanical Properties of Nanowire Fabricated by Focused Ion Beam Lithography

7.1 Introduction

This chapter presents the results of experiments in which Focused Ion Beam (FIB) fabricated free standing gold nanowire bridges were subjected to compressive loading until failure using an Atomic Force Microscope (AFM). Prior to failure the force-displacement data acquired as the nanowire bridge bends provides information regarding its elastic and plastic deformation and fracture strength. The experimental study on nanowire bridges with diameter < 50 nm showed that the mechanical properties of the nanowire bridge tend to change from conventional solid metallic properties to liquid-like behaviour with some extraordinary, previously unreported behaviour involving reforming of fractured gold bridges. This could have a significant impact on nanofabrication processes and future Nano Electro Mechanical Systems (NEMS) applications.

In this study the mechanical and hydrodynamic properties of FIB fabricated nanowire bridges with diameters in the range of 10 – 60 nm were investigated using an AFM nano tip cantilever to apply a point vertical load at the centre of the beam. Previous studies of the mechanical behaviour of nanowires are well documented [1-3]. Wu *et al* [1] reported the use of an AFM lateral loading method to measure the mechanical properties of electro chemically fabricated gold nanowires ranging from 40 – 200 nm in diameter and Cu nanowires with

diameter range of 20 – 80 nm. According to Wu [1], the 40 nm Au nanowires have yield strengths of 5.6 GPa and Cu nanowires have an average yield strength of 7 GPa. Their results demonstrate that strain hardening occurs during plastic deformation of Au nanowires. Wu estimates that the strain hardening indices range from 0.29 to 0.4, which are slightly lower than those expected for face-centred-cubic metals, such as gold. Wu hypothesises that the usual strain hardening mechanism which occurs in the bulk material, of dislocation motion and pile up, applies to nanowires of > 40 nm in diameter. Celik [2] used an AFM placed inside a SEM vacuum chamber in order to probe the behaviour of nickel nanowires fabricated by electrodeposition. They evaluated the elastic modulus and yield strength of the nanowires using this in-situ experimental arrangement and finite element simulation. However the size of the nanowires used by Celik [2] was ~ 10 times larger than those in our experiments. Lu [3] used in situ TEM to measure the tensile strength of nickel nanowires with a diameter of 360 nm. This system can provide real time data such as force-displacement. However, like Wu and Celik, this work discussed nanowires with a very large diameter in comparison to our work.

In the work presented here the compressive loading of the nanowire bridges is analogous to the centre point loading of a cylindrical beam which is fixed at both ends. For bulk Au the Young's modulus, *E*, of a cylindrical beam can be calculated using Equation 7.1 [1, 4],

$$E = \frac{\mathrm{FL}^3}{192\delta I} \tag{7.1}$$

where, *F* is the applied compressive load, *L* is the bridge length and δ is the nanowire deflection. The moment of inertia, *I*, for a bridge with a diameter *d*, can be calculated using Equation 7.2 [1].

$$I = \frac{\pi d^4}{64} \tag{7.2}$$

However, it has been shown that nanowires below ~ 50 nm in diameter develop apparent liquid-like instabilities [5] and therefore the Equation 7.1 and Equation 7.2, whilst valid for the bulk material may not apply for nanowires of such size. These instabilities, as well as the critical diameter of the nanowire structure have not been taken into consideration in the past while measuring the mechanical properties. This is due to a lack of experimental evidence and the difficulty associated with fabricating nanowires below 50 nm in diameter. Nevertheless, Yanson *et al* [6] have used scanning tunnelling microscopy and a mechanically controllable break junction (MCB) to produce and study the behaviour of chains of single gold atoms. A MCB, as described by van Rutitenbeek [7], is a purposely broken nanowire bridge suspended over a flexible substrate. As the substrate is flexed in one direction the two ends of the bridge are brought back into contact, and as it is flexed in the other direction the bridge is elongated until it reaches the failure point. Yanson [6] used a STM to measure the conductance of the MCB during the elongation phase. Their results show that as the MCB is elongated, the conductance decreases in a series of sharply descending steps, which have been shown by Rubio *et al* [8] to be the result of atomic structural rearrangements. During the last stage of elongation the conductance stays in a limited range of values corresponding to a chain of single atoms. This chain breaks at multiples of approximately 3.6 Å of elongation which is the length of a stretched Au-Au bond. Marszalek *et al* [9] reached a similar conclusion by carrying out AFM experiments on a gold coated substrate. They explain that the sliding of crystal planes generates stacking faults when the atomic structure changes within the nanowire material, known as a slip event. Their results showed that Au nanowires extend under force in steps of up to three integer multiples of 1.76 Å, which are the result of slip events [9].

Building upon this background, our study goes further and investigates the phenomenon of quantized plastic deformation in gold nanowires. Our previous work (see Chapters 4 and 5) suggests that, the surface stress in a thin wire is $\sigma_s = \frac{T}{r_o}$, where T is the surface tension and r_0 is the radius of the unperturbed wire. If the surface stress σ_s is greater than the yield stress σ_y, the wire will undergo plastic flow. If the perturbation wavelength is greater than the circumference of the wire, i.e. if $\lambda > 2\pi r_0$, the wire will break up under this surface tension stress, as in the case of the Rayleigh instability of a column of liquid [10, 12]. This model suggests that the intermolecular forces between atoms, which present microscopically and macroscopically as surface tension should drive a transition from crystalline solid behaviour to plastic or liquid-like behaviour below a minimum radius of solidity [10, 13], $r_{\min} = \frac{T}{\sigma_y}$.

7.2 Fabrication of the Nanowire Bridges

A thin layer of gold film of thickness ~ 50 – 100 nm was vacuum coated (thermal evaporation) on a single crystal p-type Si (100) substrate presenting a native oxide SiO_2 surface. The deposition was performed at a pressure of 2.7 x 10^{-6} mbar and the film thickness was controlled during deposition using a quartz crystal oscillator thickness monitor. The nanowires were fabricated by patterning with FIB milling using an FEI Dual Beam Helios 600 system machine with built-in Scanning Electron Microscope (SEM). The FIB milling was carried out using 10 keV gallium (Ga+) ions with spot size of 10 nm. Nanowires 500 nm in length were formed with diameters in the range 10 – 100 nm by milling two adjacent trenches through gold and silicon as shown in Figure 7.1. This produced a gold nanowire

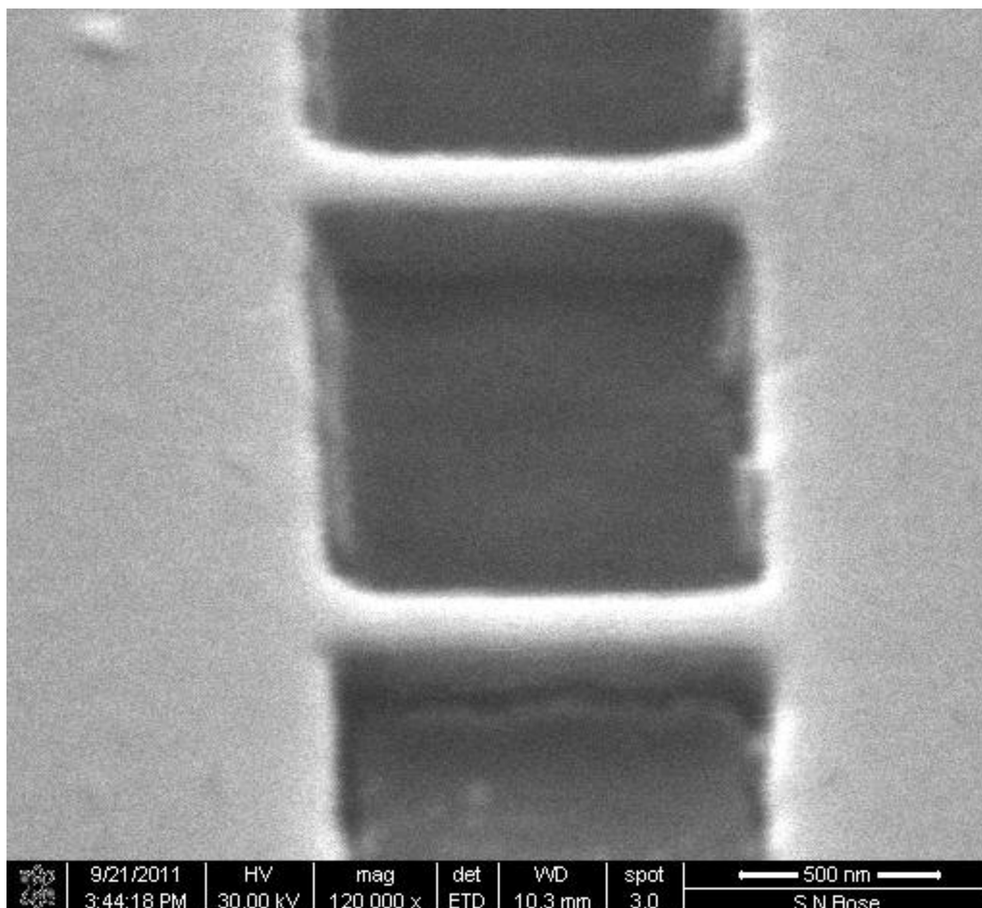

Figure 7.1: FIB fabricated gold nanowires on silicon bridges before the silicon removal by RIE

supported on a silicon bridge which was then removed using a Reactive Ion Etch (RIE) process in an STS Multiplex ICP DRIE etcher (STS Plc., UK) to a depth in the range of 10 – 100 nm underneath the nanowire, employing an etch rate of approximately 750 Å/min (fabrication method and parameters are described in Chapter 3.3.2.1). The resulting nanowire beam of cylindrical shape, as shown in Figure 7.2(a), will hereafter be referred to as a "*nanowire bridge*" and can be considered as a fixed-fixed beam in terms of structural mechanics.

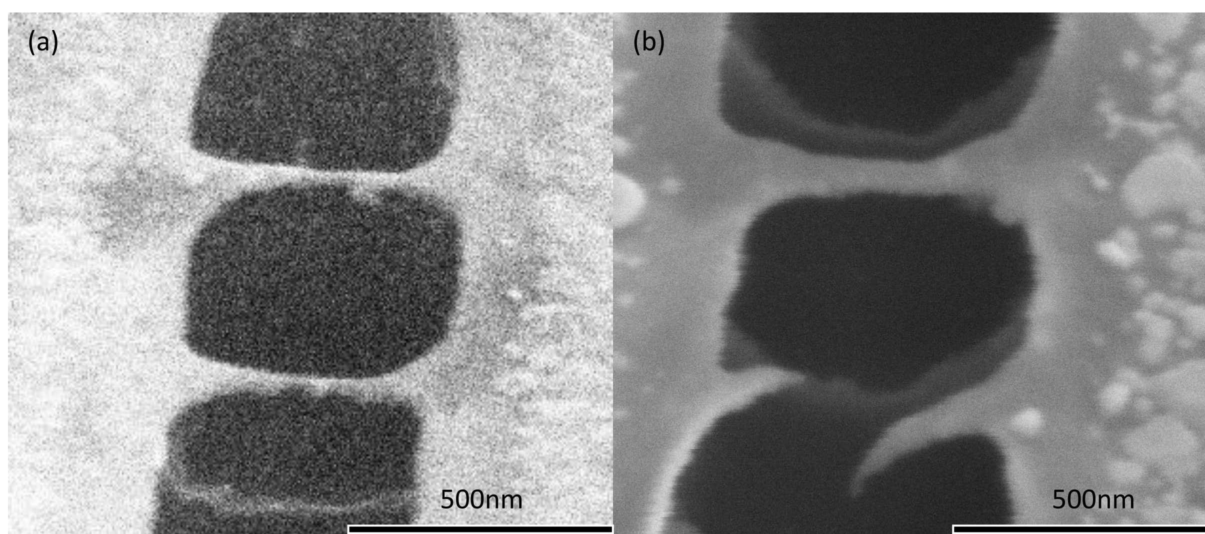

Figure 7.2: a) FIB fabricated nanowires after removing the silicon material under the gold nanowires to form a nanobridge by RIE process in STS plasma etcher (before the AFM loading). b) Nanobridge reaching its fracture point after AFM loading.

7.3 Atomic Force Microscopy on the Nanowire Bridges

The mechanical and hydrodynamic properties of these FIB fabricated nanowire bridges were investigated using an AFM cantilever with pyramidal tip of <10 nm radius of curvature (PPP-NCL, Windsor Scientific, UK) to compressively load the centre point and record force-displacement data. The compressive load applied by the AFM cantilever tip is positioned at the centre point of the nanowire bridges. As the compressive load increases the bridge

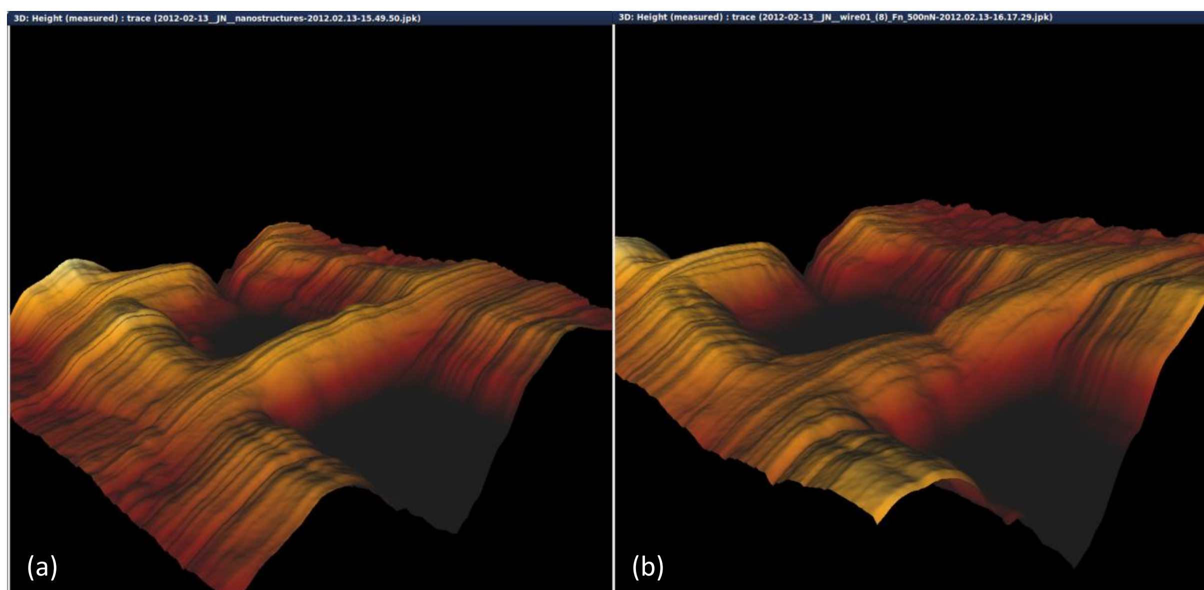

Figure 7.3: 3D images of, a) Nanowire bridge just before axial loading showing the elevated position at the midpoint and b) Two halves of the "nanowire bridge" just after reaching the fracture point.

undergoes (i) elastic deformation, (ii) plastic deformation, and (iii) fracture. Typically the motion of the tip is slightly tilted from the axis normal to the nanowire bridge.

Figure 7.3(a) shows a 3D reconstruction of the nanowire bridge, by the AFM, just before loading and Figure 7.3(b) shows an image of the nanowire bridge just after reaching the fracture point. This experiment was repeated on multiple nanowire bridge samples with diameters ranging from 60 nm down to 10 nm.

7.4 Microscopic Analysis of the Nanowire Bridges

Figure 7.2(b) shows a 60 nm diameter nanowire bridge which fractured under an applied compressive load of 508 nN. Figure 7.4(a) shows the loading and unloading curve of the same 60 nm nanowire bridge shown in Figure 7.2(b) (bottom). The fracture of the nanowire bridge resulted in two cantilever beams of approximately equal but elongated length. The tilted manipulation path of the AFM tip causes friction between the tip and the newly formed cantilever, which results in one cantilever beam being pushed downwards (during the

approach path of the AFM tip) and the other being pulled upwards (during the retraction path of the AFM tip). This can be clearly observed in Figure 7.2(b).

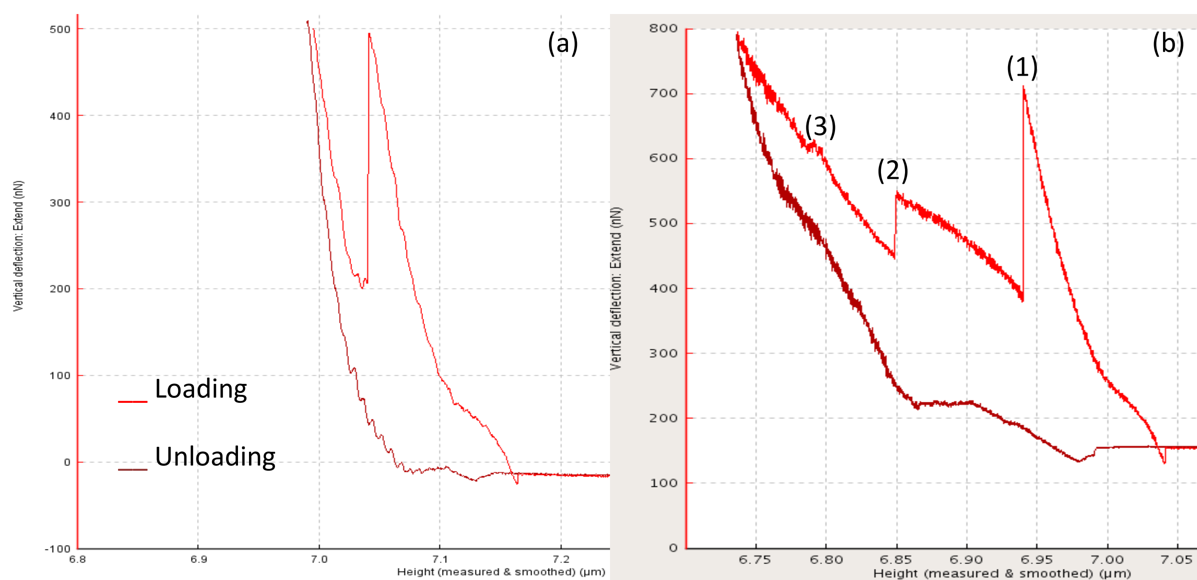

Figure 7.4: AFM tip manipulation path during the loading and unloading, a) A nanowire with diameter of 60 nm reaching fracture point at 508 nN (no rearrangement or retraction observed), b) A nanowire with diameter < 20 nm shows the constant rearrangement of gold molecules resulting in multiple fracture points (represented by 1, 2, 3).

After the RIE fabrication process to remove the silicon under the gold nanowire, nanowire bridges with diameter below 40 – 50 nm take a slightly elevated convex shape, as shown in the Figure 7.3(a). This observation can only be explained by the fact that the removal of the silicon atoms below the gold atoms can release the latter from the forces of adhesion between the substrate and the gold atoms. The mechanical properties like Young's modulus, explained by stress over strain, where the strain component has extended length (ΔL) of the beam eventually results in the elevation of the nanowire bridge.

A very interesting observation occurs at the fracture point of nanowire bridges below 20 nm in diameter. After reaching the fracture point, surface tension and atomic rearrangement of the gold atoms results in the Au atoms, within the two halves of the nanowire bridge, retracting towards their respective fixed ends of the nanowire. They then form a stable Au

liquid-like region as shown in the Figure 7.5(b). This observation is consistent with hydrodynamic behaviour previously reported for the nanowires below 50 nm in diameter [5, 10]. An Au nanowire bridge below critical diameter behaves neither as a solid metal nor a conventional liquid. However the observed result cannot be explained by a hydrodynamic interpretation alone. As the nanowire bridge approaches fracture, structural atomic

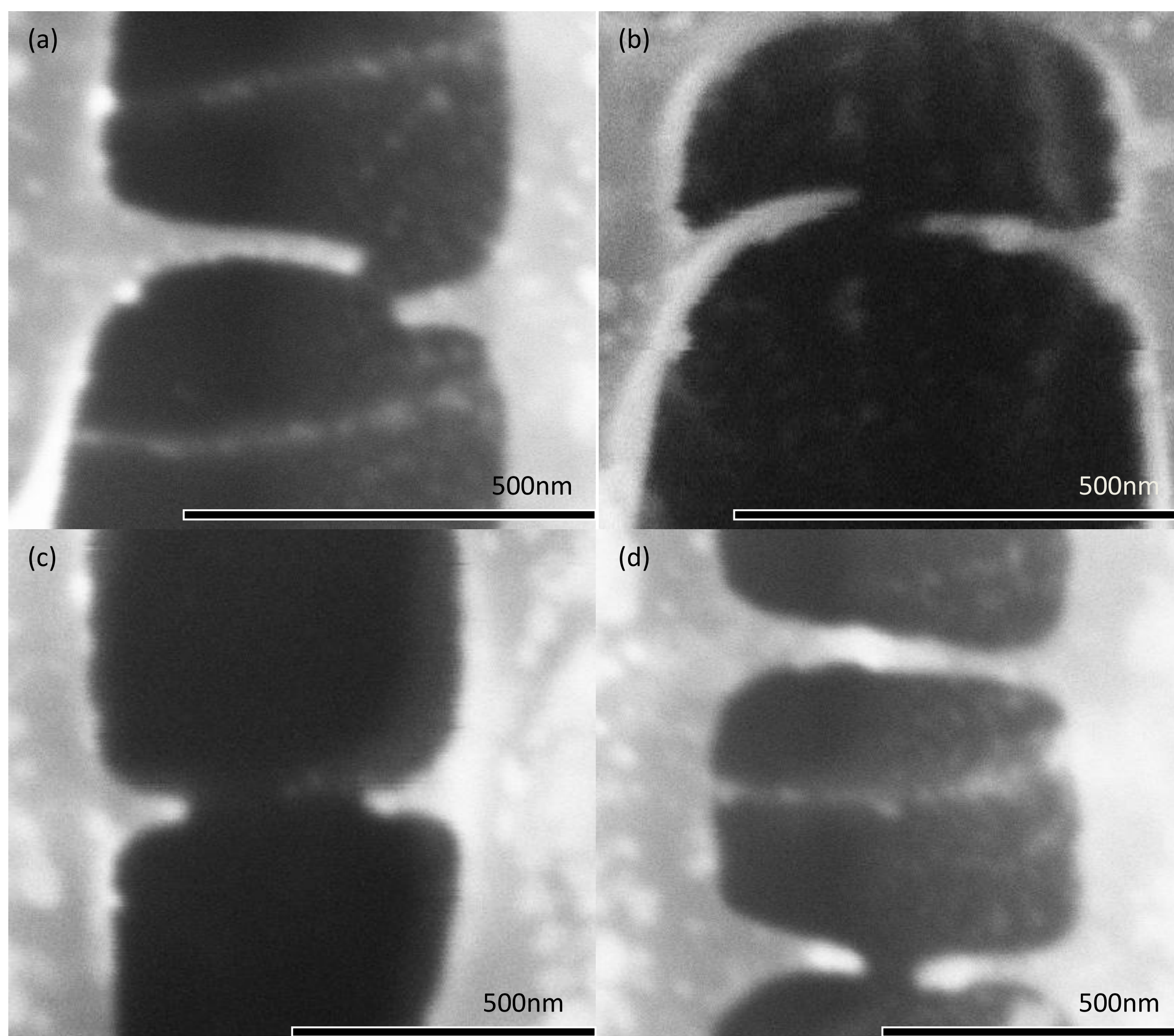

Figure 7.5: SEM image of "*nanowire bridge*", after reaching the fracture point, a) in nanowire bridge with 60 nm diameter (no retraction observed), b) in nanowire bridge with 40 nm diameter elongated to 20 nm (a small amount of retraction is observed), c) in nanowire bridge with 16 nm diameter and close to the critical diameter of the material (retraction of the gold molecules towards the surface of the substrate is observed), d) in nanowire bridge with 16 nm diameter (it is observed that the gold molecules rebind the two newly formed beams as result of *van der Waals* forces and liquid behaviour).

rearrangements occur. This atomic rearrangement phenomenon is well described by Marszalek *et al* [9]. According to their work, in normal circumstances, the arrangement of the Au atoms is face centred cubic (fcc). Under loading tension and before reaching the fracture point, there is a constant slip in the arrangement of the Au crystal planes from fcc to hexagonal close pack (hcp), which creates stacking faults [9]. Up to the fracture point the bridge behaves as solid. After reaching the fracture point, hydrodynamic behaviour dominates and the surface tension between the Au atoms causes the reverse and results in the transition from hcp back to fcc. The cycle of fcc – hcp – fcc continues until the structure achieves the minimum energy configuration and stabilises. This is due to the higher aspect ratio of the nanowire bridge combined with the attractive intermolecular forces between the Au atoms. Just before the fracture point, the nanowire bridge reaches the stage where a single strand of gold atoms (single atom nanowire) is formed. When this Au-Au bond breaks, the reaction force within the Au atoms in the resultant cantilever causes a spring effect due to the elastic strain energy stored during AFM loading. The combination of these events results in the liquid-like retraction of the Au atoms towards their respective fixed ends of the nanowire bridge as shown in the Figure 7.5(c).

Figure 7.4(b) shows the loading and unloading of a nanowire of diameter < 20 nm. In this case the nanowire bridge has multiple fracture points; Where 1 represents the first fracture of Au-Au bond. At the point of initial fracture of Au-Au, *van der Waals* forces bind the ends of the newly formed cantilever beams to the AFM tip [12]; 2 and 3 in Figure 7.4(b) represents the subsequent fracture between AFM tip and newly formed components of nanowire bridge.. After further loading the two cantilevers also fracture in two new locations and retract to the fixed end of the nanowire bridge as described earlier. If the retraction of the Au atoms is not fast enough and the separated ends of the cantilever come into contact with each other, then the Au-Au bond re-establishment takes place and the bridge subsequently reforms.

Continuous loading by the AFM tip on the nanowire bridge can result in multiple fracture points as shown in the Figure 7.4(b). However if the loading is not continuous or if it does not reach multiple fracture points then the re-established Au-Au bond will be preserved and this resulted in the self healing of the fractured nanowire bridge, as shown in the Figure 7.5(d). Where there are multiple fracture points the second point is below the first point due to the obvious reason that the *van der Waals* force between the Au atoms and the AFM tip is weaker when compared to the Au-Au metallic bond.

Figure 7.5(a) shows a nanowire bridge of 60 nm diameter, where no molecular rearrangement or retraction of the Au atoms takes place, even though the load was applied closer to one of the fixed ends of the beam. Figure 7.5(b) shows an intermediate state, where a 40 nm

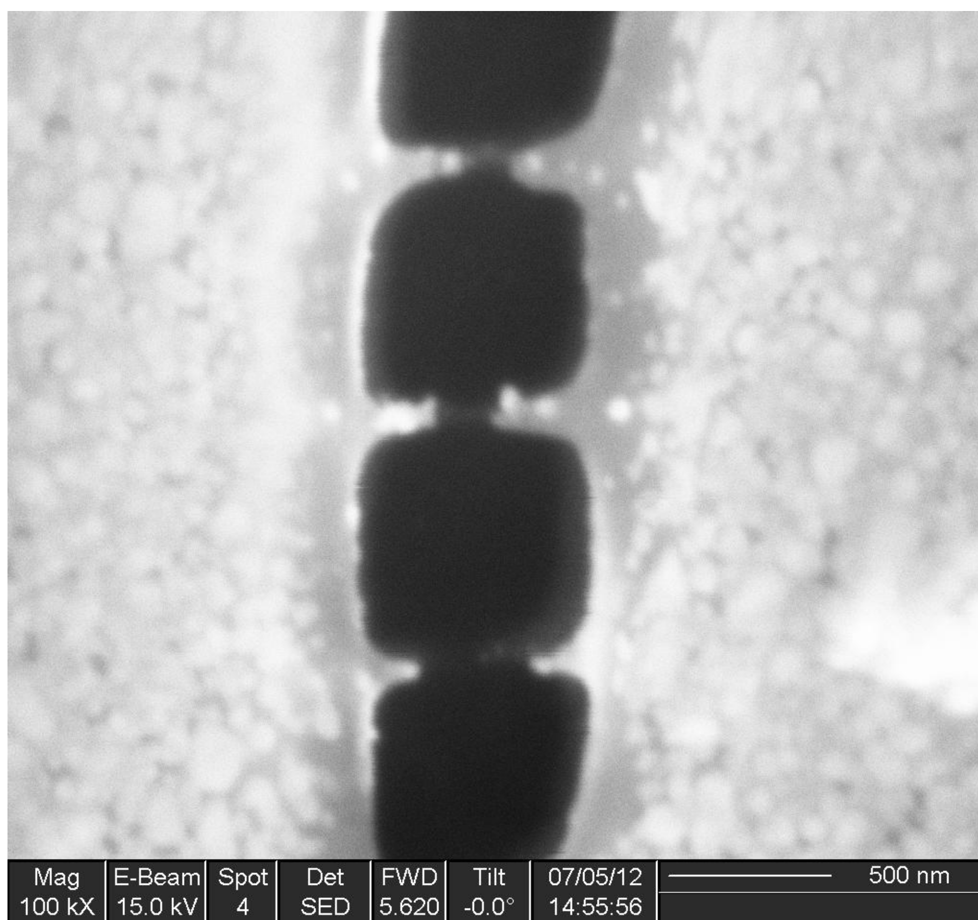

Figure 7.6: SEM image of nanowires of 40 nm (top), 30 nm (middle) and 16 nm (bottom) reaching their fracture points and achieving increasing amounts of retraction depending on their decreasing diameter.

diameter nanowire bridge has been elongated to below 20 nm diameter along some of its length. This result clearly indicates that rearrangement or retraction only takes place along the part of the nanowire bridges where the diameter falls below 20 nm (at or below the critical diameter of the gold material [10]).

Figure 7.6 shows the perfect example which demonstrates that the retraction is dependent to the diameter of the cross section of the nanowire bridge. Figure 7.6 shows the nanowires with diameter of 40 nm (top), 30 nm (middle) and 16 nm (bottom). The magnitude of the molecular rearrangement is different in each case where the nanowire of 40 nm retracted the least and the 16 nm nanowire retracted the most. The observation that the nanowire retracts more or less depending on the diameter requires further theoretical and experimental study.

Figure 7.7 and Figure 7.8 shows a step by step schematic of the two nanowire bridge behaviour scenarios during AFM tip loading, retraction and healing respectively. Figure 7.7(a) and Figure 7.8(a) show the approach path of the AFM tip to the nanowire bridge. Figure 7.7(b) and Figure 7.8(b) demonstrate the phenomenon of the *van der Waals* forces acting on the AFM tip and pulling the tip downwards to make contact with the Au atoms in the nanowire bridge. Figures 7.4(a) and (b) confirm the downward movement of the tip; a negative region, which represents an attractive force, can be seen at the end of the flat line (red line) in the approach path. In Figure 7.7(c) and Figure 7.8(c), the AFM tip penetrates the gold material and creates a disturbance in the stacking arrangement of the gold atoms in the {100} plane. This sets off the transition process from fcc to hcp to fcc and the reduction in diameter under loading tension, which continues until it reaches the point where only a single atom Au-Au bond exists just before the fracture point as shown in the Figure 7.7(d) and Figure 7.8(d).

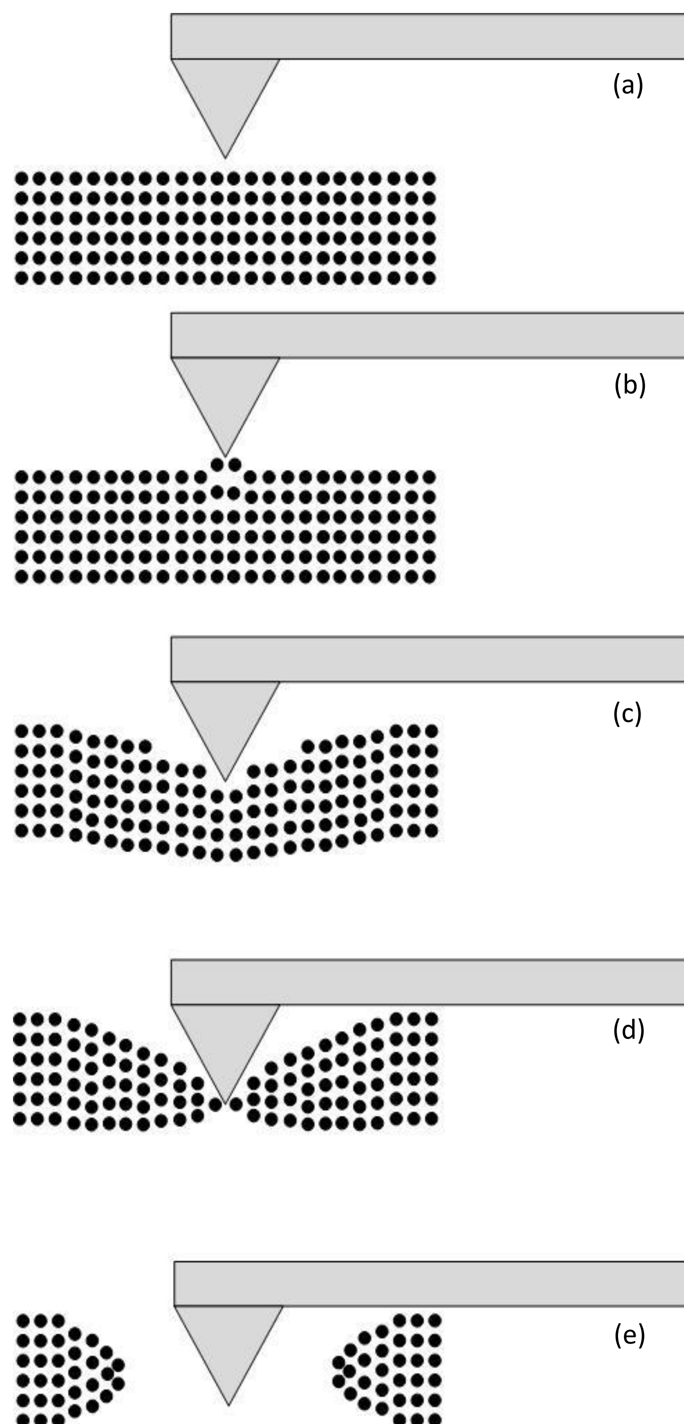

Figure 7.7: Schematic diagram of scenario one, where the bridge retracts, showing the AFM tip movement and the step-by-step behaviour of the nanowire bridge under tension; a) the AFM tip approaches the midpoint of the nanowire bridge, b) just before the tip touches the nanowire bridge the gold atoms pull the cantilever downwards due to *van der Waals* force, c) the AFM tip dislocates the gold molecules in the nanowire bridge due to forced elongation, d) just before the fracture point the nanowire bridge thins down to a single atom Au-Au bond under loading tension, e) just after reaching the fracture point the Au-Au bond breaks and because of the spring effect the gold atoms retract until the structure achieves the minimum energy configuration.

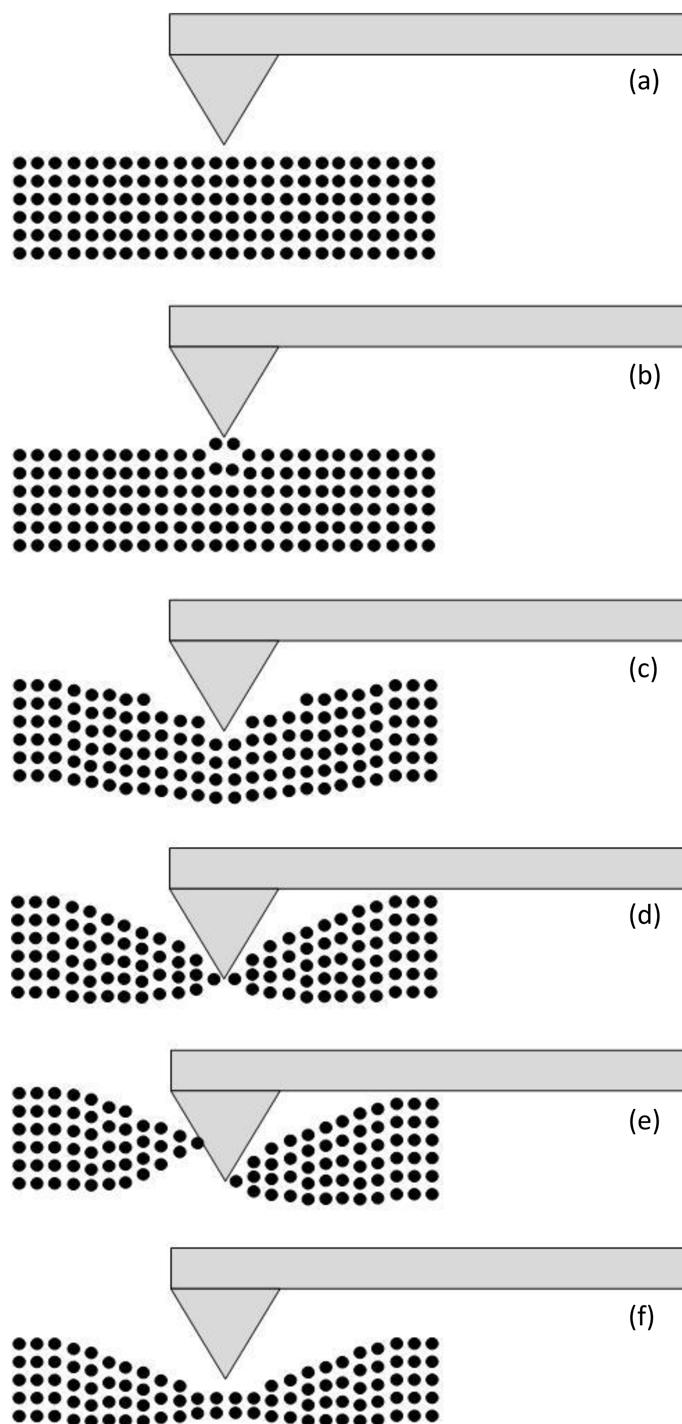

Figure 7.8: Schematic diagram of scenario two, where the bridge heals, showing the AFM tip movement and the step-by-step behaviour of the nanowire bridge under tension however the loading was retracted immediately after fracture point; a), b), c) and d) are repeated steps from scenario one, e) just after reaching the fracture point the Au-Au bond breaks, however, unlike scenario one the ends of the two newly formed beams have created a bond with the AFM cantilever tip surface under the influence of *van der Waals* force. f) the AFM tip was retracted after the fracture point and the ends of the newly formed beam re-establish the Au-Au bond which can be described as a self healing process.

After the fracture point the experiments have shown two different types of results as explained by the schematics in the Figure 7.7 and Figure 7.8. In scenario one the Au molecule retracts back due to the spring effect, which was observed and recorded in Figure 7.5(c and the bottom nanowire in d). Figure 7.7(e) demonstrates the complete retraction of the gold atoms towards the substrate after reaching the fracture point (this only occurred in wires of diameter < 20 nm). In scenario two, the AFM tip surface can establish a bond with the ends of the newly created beams under the influence of *van der Waals* forces as shown in the Figure 7.8(e). When the AFM tip is in the retraction mode immediately after the fracture and if two gold atoms come within 3.6 Å of each other (the distance between two Au-Au atoms in a stretched condition) [6], the re-establishment of the Au-Au bond takes place which can be described as a self healing process. The self healing process is observed during the experiments which can be seen in Figure 7.5(d) (top nanowire) and explained in the schematic of Figure 7.8(f).

7.5 Conclusion

Focused Ion Beam lithography was used, followed by Reactive Ion Etching, to fabricate nanowire bridges of diameter ranging from 60 nm down to 10 nm. An atomic force microscope was used to carry out experiments on the FIB fabricated nanowire bridges, by subjecting them to compressive loading until the fracture point was reached. Experimental evidence suggests that nanowires with a diameter above 60 nm simply fracture like a conventional solid material, whereas nanowire bridges with diameter below 20 nm tend to undergo retraction of the gold molecules after reaching the fracture point. The results show that the amount of retraction increases with decreasing diameter. These experiments demonstrate that post fracture rearrangement of the Au atoms takes place at a critical radius and the magnitude of the rearrangement is dependent on the cross sectional diameter of the bridge. The slide phenomenon of the crystal planes under the loading tension results in

stacking faults and the subsequent spring effect is the cause of the atomic retraction after the fracture point. One interesting observation is that if the loading tension on the nanowire bridge is not continuous then after fracture the nanowire can re-establish the Au-Au bond and eventually undergo a healing or reforming process. If the AFM tip is not retracted after fracture, but the loading is continuous then the ends of the two newly created beams can bond with the AFM tip, due to *van der Waals* forces. These bonds create multiple fracture points. All of the above experimental evidence supports the idea that nanowires material near or below critical radius have liquid-like behaviour.

7.6 References

[1] Wu B., Heidelberg A., Boland J. J., *Mechanical properties of ultrahigh-strength gold nanowires*, Nature Materials, 2005, **4**: p 525-529.

[2] Celik E, Guven I, Madenci E, *Mechanical characterization of nickel nanowires by using a customized atomic force microscope*, Nanotechnology, 2011, **22**(15): p 155702.

[3] Lu Y., Peng C., Ganesan Y., Huang J Y, Lou J, *Quantitative in situ TEM tensile testing of an individual nickel nanowire*, Nanotechnology, 2011, **22**: p 355702.

[4] Gere J. M., Timoshenko S. P., *Mechanics of Materials*, Fourth Edition, (1997), p 690.

[5] Naik J. P., Prewett P. D., Das K., Raychaudhuri A. K., *Instabilities in Focused Ion Beam-Patterned Au Nanowires. Microelectronics Engineering*. 2011, **88**: p 2840-2843.

[6] Yanson A. I., Bollinger G. R., Van den Brom H. E., Agrait N.,van Ruitenbeek J. M., *Formation and manipulation of a metallic wire of single gold atoms*, Nature (London), 1998, **395**: p 783–785.

[7] van Ruitenbeek J. M., Alvarez A., Piñeyro I., Grahmann C., Joyez P., Devoret M. H., Esteve D., Urbina C., *Adjustable nanofabricated atomic size contacts*, Rev. Sci. Instrum., 1996, **67**(1): p 108.

[8] Rubio G., Agraıt N., Vieira S., *Atomic-Sized Metallic Contacts: Mechanical Properties and Electronic Transport*, Phys. Rev. Lett., 1996, **76**: p 2302–2305.

[9] Marszalek P. E., Greenleaf W. J., Li H., Oberhauser A. F., Fernandez J. M., *Atomic force microscopy captures quantized plastic deformation in gold nanowires*, PNAS, 2000, **97**(12), p 6282-6286.

[10] Naik J P, Prewett P D, Das K, Raychaudhuri A K, *Liquid-like instabilities in gold nanowires fabricated by focused ion beam lithography*, Appl. Phys. Lett., 2012, **101**: p 163108.

[11] Rayleigh L., Proc. London Math. Soc., 1878, **10**, p 4.

[12] Aradhya S. V., Frei M., Hybertsen M. S., Venkataraman L., *van der Waals interactions at metal/organic interfaces at the single-molecule level*, Nature Materials, 2012, **11**: p 872–876.

[13] S. Chandrasekhar, *Hydrodynamic and Hydromagnetic Stability*, Dover press, New York, 1981, p 515–574.

Chapter 8

Summary and Conclusion

8.1 Summary

This thesis presents research work on nanowires fabricated by Focused Ion Beam (FIB) lithography, including fabrication and characterisation techniques, and experiments to understand better their mechanical, electrical and hydrodynamic properties.

Focused Ion Beam lithography was used to etch nanowires ranging from 200 nm down to less than 10 nm in diameter (Chapter 3). Microscopic characterisation was conducted to investigate the hydrodynamic instabilities present in the nanowire geometry (Chapter 4). The effect of different substrates on these instabilities were also investigated (Chapter 5). Due to time constraints it has not been possible to perform a statistical analysis on the presence of hydrodynamic instabilities in the nanowire samples reported here. However, comparison with the work of others suggests that the results shown are not atypical. Electrical measurements were conducted on the Pt nanowires fabricated by FIB metal deposition (Chapter 6). The first section, *Section **A***, of this chapter investigated the temperature dependent resistivity and provides evidence that such nanowires are a two phase percolating system. In the second section, *Section **B***, experiments were conducted on a MEMS bimorph cantilever fabricated by the combined process of FIB etching and metal deposition, by which a small heater with multiple meander was deposited on the top of the cantilever. An Atomic Force Microscope (AFM) was used to measure the deflection and effective force generation as a function of drive current to the integrated heater with a higher accuracy than hitherto achieved. Focused Ion Beam lithography was used, followed by Reactive Ion Etching, to fabricate nanowire bridges with diameters ranging from 60 nm down to 10 nm. These FIB

fabricated free standing gold nanowire bridges were subjected to compressive loading until failure using an AFM, in order to understand their mechanical behaviour (Chapter 7).

8.2 Detailed Conclusions

Chapter 3 describes various fabrication techniques to produce nanowires ranging from 200 nm down to less than 10 nm in diameter. In particular, Focused Ion Beam lithography was used to fabricate nanowires below 10 nm which had not previously been achieved. Electron Beam Lithography and Photolithography (UV lithography) were also used to fabricate nanowires of few nanometres in diameter to compare the instabilities with those fabricated by FIB.

Microscopic characterisation of Au nanowires fabricated by FIB demonstrates that these nanowires develop hydrodynamic instabilities below a certain width (~ 50 – 40 nm). These are liquid-like instabilities and first show-up as undulations in nanowire width with clearly defined wave lengths. The observed behaviour has been explained as a manifestation of the classical Rayleigh – Plateau instability which occurs when the surface energy dominates (described in Chapter 4). It has been found that use of an adhesion layer of Cr inhibits the onset of the instability and shows potential for stable ultra-narrow FIB-etched nanowires for nanosensors and other applications. For smaller widths (~ 20 nm) the instabilities grow and the wires eventually break-up into spherical balls. Further experiments in Chapter 5 investigate *inter alia* the effects of different substrates and doping elements on nanowire stability.

Chapter 5 investigates the structural and morphological stability of Au nanowires fabricated by Focused Ion Beam etching of gold films on different substrates. The stability of the wires is noticeably better in the case of conducting Si substrates than for Si substrates coated with the insulators SiO_2 or Si_3N_4. This is attributed to the influence of better bonding of Au with Si

and to the greater conductivity of Si which minimises space charge effects during FIB fabrication. Instabilities are reduced still further for the same reason by the use of highly doped Si. Buffer HF treatment of Si is used to remove the native oxide from the surface, which gives improved resistance to instability due to the much improved adhesion of the gold film. On insulating substrates there is also clear evidence under SEM investigation of electrohydrodynamically formed Taylor Cones (described in Chapter 5). FIB heating effects cannot be excluded as a contributory factor to the instabilities due to local transient beam induced melting during FIB etch, an effect which is worthy of further study. The instabilities investigated in this study could severely limit the use of gold nanowires in nanosensors and other nanoscale devices.

Chapter 6 is divided into two sections. In *Section A* of the chapter the results indicate that Pt nanowires fabricated using FIB metal deposition are in fact a two phase composite percolating system, where the metallic and insulating temperature dependent behaviour demonstrate the existence of both phases simultaneously. A study of beam energy dependence of metallic concentration and electrical measurement of consequential behaviour was carried out. The results demonstrate a percolation controlled conduction mechanism with a critical metallic volume concentration (CMVC) of 36% compared with predictions of 30% from standard percolation models. They also show an anomalous temperature dependence of resistance for metallic volume concentrations at 36%. This is strong evidence for a percolation mechanism and has been linked in our work to temperature induced strain in the nanowires. This reduces the metallic volume concentration, thereby increasing the resistivity. However, the unexpectedly high magnitude of the resistivity change suggests that inter-particle electron tunnelling plays a significant role in the conduction mechanism. This strain effect could be exploited to fabricate actuators which are suitable *inter alia* for simple nanosensor strain gauges, gas sensors or thermometers.

In Section B, experiments were conducted on the performance of a MEMS bimorph cantilever fabricated using the combined process of FIB milling and metal deposition. An AFM was used to measure the deflection and the effective force generation as a function of drive current to the integrated heater with a higher accuracy than hitherto achieved. The experiments on the micro-cantilever system showed higher deflection sensitivity than previously reported. The effect of thermally driven strain combined with tunnelling conduction on Focused Ion Beam deposited platinum, provides an opportunity for strain tuned resistance and strain gauge nanosensor applications. The experiment also demonstrates that due to the high temperature sensitivity, the thermal isolation of any MEMS or NEMS device is an absolute requirement for controlled behaviour.

Experimental evidence in Chapter 7 suggests that nanowire bridges with diameter above 60 nm simply fracture like a conventional solid material, whereas nanowire bridges with diameter below 20 nm tend to undergo liquid retraction of the gold molecules after reaching the fracture point. These experiments demonstrate that post fracture rearrangement of the Au atoms takes place at a critical radius. The magnitude of the rearrangement is dependent on the cross sectional diameter of the bridge with decreasing diameter resulting in greater retraction. The sliding of the crystal planes under loading tension results in stacking faults and the subsequent combination of stored spring energy and surface tension is the cause of the atomic retraction after the fracture point. One interesting observation is that, if the AFM tip is immediately withdrawn after the facture point and the loading tension on the nanowire bridge is not continuous, then the nanowire can re-establish the Au-Au bond and eventually undergo a healing or reforming process. If the AFM tip is not withdrawn after fracture and the loading is continuous then the ends of the two newly created beams can bond with the AFM tip, due to *van der Waals* forces. These bonds create multiple fracture points. All of the above

experimental evidence supports the idea that nanowires near or below critical radius show liquid-like behaviour.

8.3 Future Work

In the present work, experimental evidence suggests that the instabilities occur below ~ 50 nm diameter. However, the fabrication and characterisation was carried out at ambient temperature only and further investigation is required exploring the effect of temperature variation, e.g. the effect of annealing. Apart from the width of the wire and charging effects, additional factors like impurities, strain and temperature can also influence these instabilities. Recently, some limited work has been done elsewhere to understand thin nanowire instabilities through theoretical and experimental studies [1-2]. Karim *et al* [3] investigated the stability of gold nanowires under annealing stating that these instabilities at lower temperatures should be taken into account when fabricating NEMS devices. Further investigation is required to investigate this temperature dependency on the nanowire instabilities.

Our investigation concentrated on the instabilities in Au nanowires and the temperature dependence resistivity and percolating system in FIB deposited Pt nanowires. Investigations should be carried out on the behaviour of other materials like nickel (Ni), tungsten (W) etc. Materials other than metals like ZnO should be used for such experiments to assess their potential for NEMS applications. The substrates used in our experiments are only various forms of silicon (Si) and its oxide and silicon nitride (Si_3N_4). Other substrates should be explored for similar experiments, especially the effect of substrate on liquid-like instabilities. Expanding upon the present work in Chapter 6, NEMS and MEMS devices, such as a pressure sensor, can be fabricated using the Pt-C percolating/Kirkpatrick system.

FIB fabricated nanowires can be used for single electron transistor (SET) devices. Chapter 7 describes such types of nanowires and nanowire bridges. This work also describes the atomic retraction at or below critical radius, which requires further investigation and mathematical simulation to establish the diameter dependency of these retractions in the Au atoms in such conditions. These experiments should be repeated for other materials like Pt and Ni.

FIB fabricated nanowires with diameters of a few nanometres require further investigation to explore their magnetic and vibrating properties. The use of ferromagnetic materials like nickel and metals with low Curie temperature, like Gadolinium, should also be explored and incorporated in the fabrication of nanowires and their applications.

8.4 References

[1] Hobi E. Jr, Fazzio A., da Silva A. J., *Temperature and Quantum Effects in the Stability of Pure and Doped Gold Nanowires*, Phys Rev Lett., 2008,**100**(5): p 056104.

[2] Bid A., Bora A., Raychaudhuri A. K., *Low frequency conductance fluctuations (1/f_ noise) in 15nm Ag nanowires-Implication on its stability*, Phys. Rev B, 2005, **72**: p 113415.

[3] Karim S., Toimil-Molares M. E., Balogh A. G., Ensinger W., Cornelius T. W., Khan E. U., Neumann R., *Morphological evolution of Au nanowires controlled by Rayleigh instability, Nanotechnology*, 2006, **17**: p 5954-5959.